ALMA MATER STUDIORUM
UNIVERSITÀ DEGLI STUDI DI BOLOGNA
Facoltà di Scienze Matematiche Fisiche e Naturali

Dottorato di Ricerca in Geofisica
XXI Ciclo
Settore scientifico disciplinare: GEO/10

THE RUPTURE PROCESS OF RECENT TSUNAMIGENIC EARTHQUAKES BY GEOPHYSICAL DATA INVERSION

Ph.D. Thesis by:
Fabrizio Romano

Tutor:
Dr. Alessio Piatanesi

Supervisors:
Prof. Maurizio Bonafede
Prof. Stefano Tinti

Coordinator:
Prof. Michele Dragoni

2009

Acknowledgements

I am grateful to Dr. Alessio Piatanesi who gave me the opportunity to work in his group of research during my Ph.D., for being my guide and mentor and for his precious teachings.

I would like to thank Dr. Stefano Lorito for his constant support during these years.

Contents

PART 2 – *Applications*

Introduction

Seismology involves analysis of ground motions produced by energy sources within the Earth, such as earthquake faulting, but also concerns the study of the rupture process related to these seismic events. Except in the intermediate vicinity of the source, most of the ground motion is ephemeral; the ground returns to its initial position after transient have subsided. Vibrations of this type involve small elastic deformations, or *strains*, in response to internal forces in the rock, or *stresses* [*Lay and Wallace*, 1995]. The theory of elasticity provides mathematical relationships between the stresses and strains in the medium.

The release of stress accumulated during tectonic deformation reflects in a sudden slip along the fault plane, causing an earthquake. The magnitude of a seismic event has a large variability and strongly depends on the stress accumulated on the source zone. Seismic activity on the Earth is continuous, but since accumulating a great amount of stress requires a relatively long time, then great earthquakes – magnitude > 8.0 – do not occur very frequently, as described by the *Gutenberg-Richter's Law* [*Gutenberg and Richter*, 1944, Fig. I.1].

An earthquake is the demonstration that the Earth is an evolving system, but often becomes the cause of human tragedies and huge infrastructural damages, as it was dramatically shown by the great 2004 Sumatra earthquake and tsunami, with over 200,000 fatalities and hundreds of coastal settlements destroyed. Seismology, along with a better knowledge of the Earth's physical phenomena, can help to prevent or at least mitigate the consequences of similar disasters in the future. This can be done by estimating the seismic hazard at a given site or by means of early warning systems, or forecasting the occurrence of the eventually generated tsunamis after the next strong seismic events.

This is an ambitious goal, and the seismology is a science relatively young, but the continuous improvement of the instrumental technology and the advances accomplished by seismology in the last decades permit to be optimist. Actually, today we have at our disposal a huge and various amounts of instruments that record for example seismic waves, ground deformations, gravity and sea level changes.

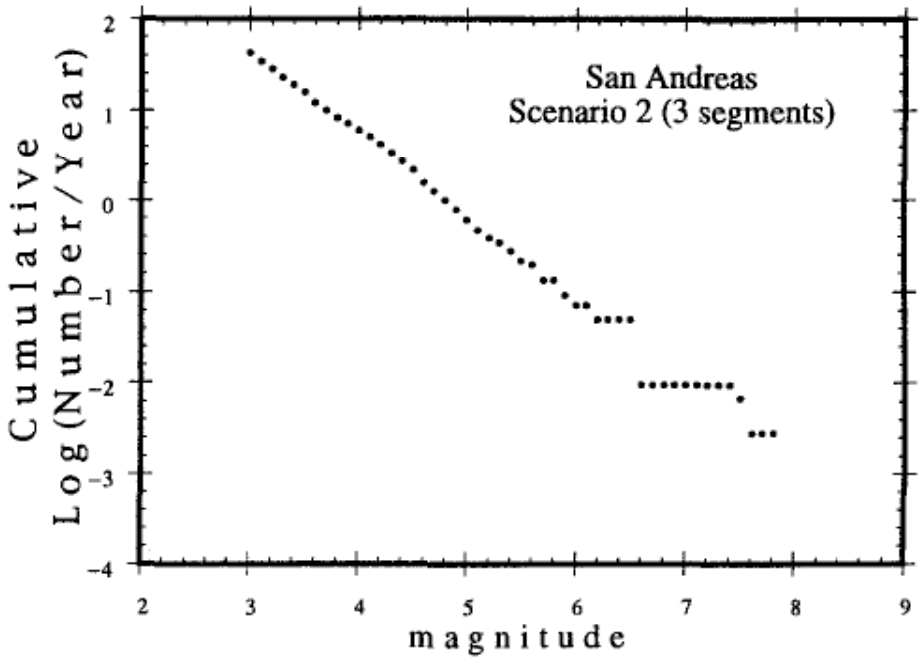

Figure I.1. Cumulative number of events per year versus magnitude for the San Andreas fault zone [after *Wesnousky,* 1994]; the *Gutenberg-Richter's law* is "$\log n = a - bM$" where *n* is the number of events of magnitude *M* and *a* and *b* are constants [*Gutenberg and Richter*, 1944].

Nevertheless, the length of these time series is not still sufficient to our purpose, because recurrence times of the strong earthquakes are very long in comparison, on the order of hundreds or thousands of years. The understanding of the source processes could allow to fill, at least in part, this lack of data. This is exactly the objective of the seismic source investigation.

Unfortunately, the direct observation of an earthquake is often practically unfeasible, and this is true in particular for submarine earthquakes, which are the main subject of this thesis. Nevertheless, we can collect observables measured by instruments positioned on the surface of the Earth and even on the ocean bottom. Therefore, the typical way to proceed when we want to draw out information regarding the source process is to have recourse to the inversion of the geophysical data at our disposal.

In the present thesis, we approach the study of the seismic source by the inference about kinematical parameters of the rupture process. A typical way to infer these parameters is by performing an inversion of seismic waveforms or geodetic data collected during the seismic events.

Large, shallow earthquakes in subduction zones contribute ~90% of the total seismic moment released worldwide [*Pacheco and Sykes,* 1992; *Stern,* 2002]. These

earthquakes have a focal mechanism indicating thrust faulting along the subduction interface. Subduction zones are in fact constituted by an oceanic plate sliding beneath a continental plate. The friction between the two causes the occurrence of a strong seismicity. Because such earthquakes are so powerful and shallow, they constitute a special hazard to people who live near convergent margins. Furthermore, since several of these earthquakes occur under the ocean, the sea-bottom displacements caused by the submarine fault motions cause large-scale displacements of the overlying water column, which gravity will finally bring back to rest, so generating the tsunamis.

Besides the many measurements cited above, therefore exist also the tsunami data, as for example tide-gage records or runup heights measured inland. Actually, in the last years, the importance of this kind of geophysical data for retrieving the source parameters has been demonstrated in several occasions. The tsunami data help in constraining the portion of the fault area positioned offshore, generally close to subduction margin (the trench), that conversely other kinds of data are not able to constrain [*Satake*, 1993].

A first step in dealing with the problem of investigating a seismic event is to represent the seismic source. A fault plane, where the earthquake occurs, is defined in a schematic way by means of a rectangular area. This area, along with its geometrical – depth, strike, dip – and kinematical – slip, rake, rupture velocity – parameters, represents the seismic source. The kinematical properties are the parameters we want to determine to retrieve information about the rupture process,

Generally, however, the geophysical inverse problems involve parameters that because of their mutual complex relations may introduce strong nonlinearities. Therefore, to solve these problems, it is in some cases necessary to turn to methods of global optimization.

This thesis is devoted to the understanding of the rupture process of the seismic sources of great earthquakes that generate tsunamis. A much better understanding of the tsunamigenic earthquakes and, more generally, the link existing between the earthquake magnitude and the tsunami magnitude is one of the open issues about tsunamis. Actually, it may happen that a large earthquake generates a small tsunami and *vice versa*. For example the 2007 M_W 8.4 Sumatra earthquake generated a much small tsunami than the weaker 2006 M_W 7.8 Java earthquake, which produced a very destructive wave over the adjacent coastline.

The tsunamigenesis in fact is controlled by several factors, as the earthquake mechanism, the depth of the rupture, the slip distribution along the fault area, as well as the mechanical properties of the source zone. Each of these factors plays a fundamental role in the tsunami generation.
Therefore, inferring the source parameters of tsunamigenic earthquakes is crucial to understand the generation of the consequent tsunami and so to mitigate the risk along the coasts.
In the next chapters I discuss the rupture process of some recent tsunamigenic events, as inferred by means of an inverse method. In this thesis, particular attention has been paid in investigating how well the different geophysical datasets can constrain the different source parameters, as well as different aspects of the rupture process. This will lead to highlighting the importance of combining different datasets in joint inversions in order to constrain in a much better way the rupture process.

In the first part of this thesis (*Theory and Methodology*) the seismic source and the tsunami problem, the used geophysical datasets, the Green's functions method and the inversion technique will be presented.
In *Chapter 1* it is briefly illustrated what a tsunami is and the seismic source representation discussed, with special attention to those parameters that are important for the tsunamigenic process.
Chapter 2 presents a concise summary of the observables and the corresponding instruments that allow to study a tsunami, highlighting their advantages and drawbacks.
In *Chapter 3* I will carry on with introducing the Green's functions method, which is used to face the problem of inferring the slip distribution and other parameters on the source area; moreover I will discuss a general scheme for the parameterization of the fault plane and the method employed for the numerical modeling of tsunami propagation. Then I will illustrate the formulation of the global optimization problem, the resolution tests, and the error estimation.
In the second part of this thesis (*Applications*) some applications will be presented.
In *Chapter 4* I will illustrate the Mw 8.1 September 25, 2003 Tokachi-oki earthquake, where I show that a joint-inversion of tsunami waveforms and GPS data allows to constrain the slip distribution on the fault area much better than the single datasets separately.

Then, in *Chapter 5* I will carry on with the investigation of the rupture process of the M_W 8.4 September 12, 2007 Sumatra earthquake: in this case – inverting only for tide-gages waveforms – even the rupture velocity has been inferred along with the slip distribution. Moreover, a possible explanation is given for the relatively small tsunami generated by that earthquake, and the possibility of a future big event is warned. Finally, in *Chapter 6* I will present the study of the Mw 9.2 December 24, 2004 Sumatra earthquake. In this case, is performed for the first time a joint-inversion of tide-gages, satellite altimetry and GPS data to retrieve the slip distribution, the rake and the rupture velocity along the entire fault. Furthermore, a novel method is proposed for self-consistent estimation of the source zone rigidity.

The applications discussed in the current Ph.D. thesis are presented in the following papers:

Romano F., S. Lorito, A. Piatanesi, and K. Hirata (2009), Slip distribution of the 2003 Tokachi-Oki (Japan) Mw 8.1 earthquake from joint inversion of tsunami waveform and geodetic data (*submitted to Journal of Geophysical Research*).

Lorito S., **F. Romano**, A. Piatanesi and E. Boschi, (2008), Source process of the September 12, 2007, Mw 8.4 southern Sumatra earthquake from tsunami tide gauge record inversion, *Geophys. Res. Lett.*, *35*, L02310, doi:10.1029/2007GL032661.

Lorito S., A. Piatanesi, V. Cannelli, **F. Romano**, and D. Melini (2009), Kinematics and Source Zone Properties of the 2004 Sumatra-Andaman Earthquake and Tsunami: Nonlinear Joint Inversion of Tide-Gage, Satellite Altimetry and GPS data, *J. Geophys. Research,* (*accepted with revision*).

PART 1
Theory and Methodology

Chapter 1

Tsunamis and tsunamigenic earthquakes

Generally, the largest seismic events occur on faults located along the subduction zones. Since a part of the fault plane is positioned under the ocean, then the seafloor motion reflects in displacement of the water that returns to its initial equilibrium condition triggering anomalous water waves, which are called tsunamis. I discuss here the importance of understanding the rupture process that triggers the tsunami waves.

1.1 Characterization of the seismic source

An earthquake is a physical event that occurs on *faults*, surfaces in the Earth on which one side moves with respect to the other. In the *elastic rebound theory* of earthquakes on a fault [*Reid,* 1910], materials at distance on opposite sides of the fault move relative to each other, but friction on the fault locks it and prevents the sides from slipping (Fig. 1.1). Finally the strain accumulated in the rock is more than rocks on the fault can withstand, and the fault slips, resulting in an earthquake.

In the study of the tsunamigenic earthquakes, one of the most important goals is to understand the rupture process, which intrinsically means to retrieve information about the seismic source. As we will see, the parameters of the earthquake source play a determinant role in the tsunami generation. Actually, inferring the kinematics of the source zone is important because permits to discover the process that generated the seafloor motion and the consequent tsunami. The parameters that describe the earthquake source include geometrical characteristics, such as the dimensions and the orientation of the fault and mechanical parameters, such as the hypocenter (where the rupture initiates on the fault), the rupture velocity (how rapidly the rupture spreads over the fault), and the slip amplitude and direction (how adjacent points on the fault are slipping).

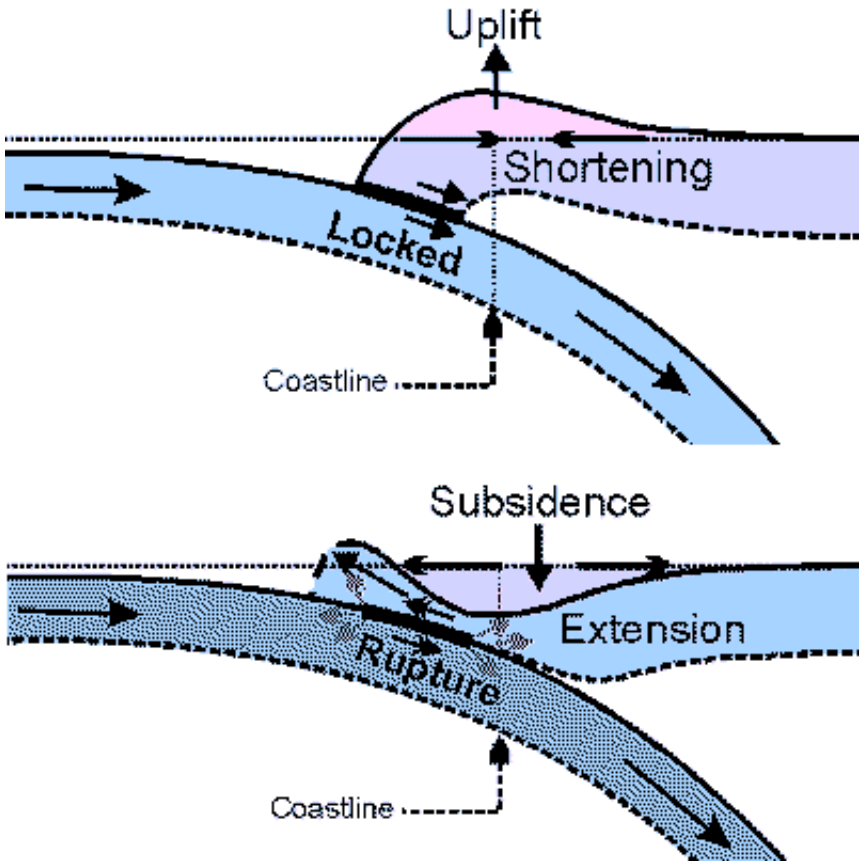

Figure 1.1. Simple subduction earthquake model. Plate convergence is on-going but the two plates are locked over some width of the subduction thrust fault; since the accumulating stress exceeds the strength of the fault, the locked zone fails and a great earthquake occurs [http://gsc.nrcan.gc.ca/geodyn/eqcycle_e.php].

Each of these parameters has a role in tsunami generation, and it is therefore important to understand their variability and the relative capability to trigger or not an anomalous wave.

Among the possible factors that control the tsunamigenesis, the earthquake mechanism is crucial; the vertical displacement field of an oblique slip event is the sum of the displacement fields derived from the dip-slip and strike-slip components. In general the vertical displacement normalized with respect to the slip component is lesser for the strike-slip component than for the dip-slip component [*Kajiura*, 1981; *Geist*, 1999]. Therefore dip-slip events favor tsunami waves higher than strike-slip events. Moreover, the depth of the rupture and the slip distribution along the fault area contribute to amplify or attenuate the tsunami waves amplitude; in fact, shallow

events as well as heterogeneous slip distribution reflect in more relevant tsunami waves. However, not only the geometrical properties of the fault are important with respect to the process of generation of the tsunami. In fact, also the mechanical properties of the source zone play a fundamental role. The vertical inhomogeneity of the lithosphere with respect to the shear modulus has a significant effect on the displacement field. Layering distinguished by rigidity is particularly relevant for the subduction zones, and the contrast in the shear modulus can affect the seafloor displacement [*Geist,* 1999].

1.2 What is a tsunami?

A *tsunami* is a wave, or series of waves in a wave train, generated by the sudden, vertical displacement of a column of water. The main cause that can generate a tsunami is the seismic activity, but a tsunami can be set in motion also by explosive submarine volcanism, submarine landslide or slide entering a water body mass, asteroid impact, or by the sudden change of the atmospheric pressure due to meteorological phenomena. The origin of term *tsunami* is Japanese and means "big wave into the harbor"; actually, such waves often develop as a resonant phenomenon in harbors after an offshore earthquake and this therefore justifies the Japanese term.

The tsunamis are gravity waves that propagate in the ocean and are very different from the much common wind waves, first of all because they have wavelengths and periods greater than the common beach waves; in fact the typical tsunami wavelength ranges from 10 km to hundreds of km, and the typical tsunami period ranges from 5 to a few ten of minutes [*Ward,* 2001]. Another characteristic of the tsunami is its propagation speed, reaching even 900 km/h in the open ocean and slowing down to ~50 km/h near the coastline.

Tsunamis are natural hazards that pose serious threat even to regions very far from the source; actually, tsunami waves may propagate for thousands of km without significant energy dissipation, if we exclude the attenuation due to geometrical spreading of the expanding wavefront. According to the kind of source that generates the tsunami, the wave amplitude may vary in a considerable way. While a tsunami propagates in open ocean, the typical wave amplitude is about 5-20 cm [*Ward,* 2001] and the wavelength is very long (ships do not feel the effects of the passage of the tsunami); conversely, as the wave approaches the coastline, the wavelength decreases

and the amplitude grows (*shoaling*) depending on the bathymetry and the tsunami may achieve a notable height (until several meters). In most cases, even if there are not victims, the damages to the coastal structures are relevant.

1.3 The tsunamis distribution on the Earth

Although the worldwide resonance and the perception of the risk about the tsunami were amplified by the catastrophic event occurred at Sumatra in December 2004, tsunamis have always affected the oceans as they have been documented also during the past ages.

In fact, there are many historical witnesses, from different zones of the world, which report impacts of tsunamis on coastlines, and several fatalities, and structural damages of the houses and harbors, unlucky consequences of the tsunami passage.

Since most tsunamis are generated by earthquakes (about 80% of the events), they are not randomly distributed around the oceans; actually, if we observe the distribution of the world seismicity, then we can see that a very strong correlation exists with the locations of the tsunami events (Fig. 1.2).

This is particularly evident around the Pacific Ocean, since the subduction zones – as we will discuss later - are the natural places to generate tsunamigenic earthquakes. We can mention some relevant events, e.g. the May 22, 1960 Chilean earthquake – one of the more significant historical event – or the March 28, 1964 Alaska earthquake. More recent events are the September 25, 2003 Tokachi-oki, the November 15, 2006 and January 13, 2007 Kuril Islands earthquakes [*Bryant,* 2008].

However, tsunamis occur not only in the Pacific area, but also around the Atlantic Ocean, e.g the November 1, 1755 Lisbon earthquake, around the Mediterranean area, e.g. the December 28, 1908 Messina earthquake and the May 21, 2003 Boumerdes-Zemmouri earthquake, and around the Indian Ocean, e.g. the December 26, 2004 and the September 12, 2007 Sumatra earthquakes (Tab. 1.1), which we will deal with in the following chapters. However, we cannot forget the existence of some important and catastrophic events due to causes other than the seismic activity. Actually, even volcanic explosions can generate a tsunami – like in the case of the eruption of the Krakatoa volcano on 1833, with waves as high as 30 meters – but also submarine landslides, triggered or not by an earthquake – e.g. the July 17, 1998 Papua New Guinea [*Heinrich et al.,* 2001].

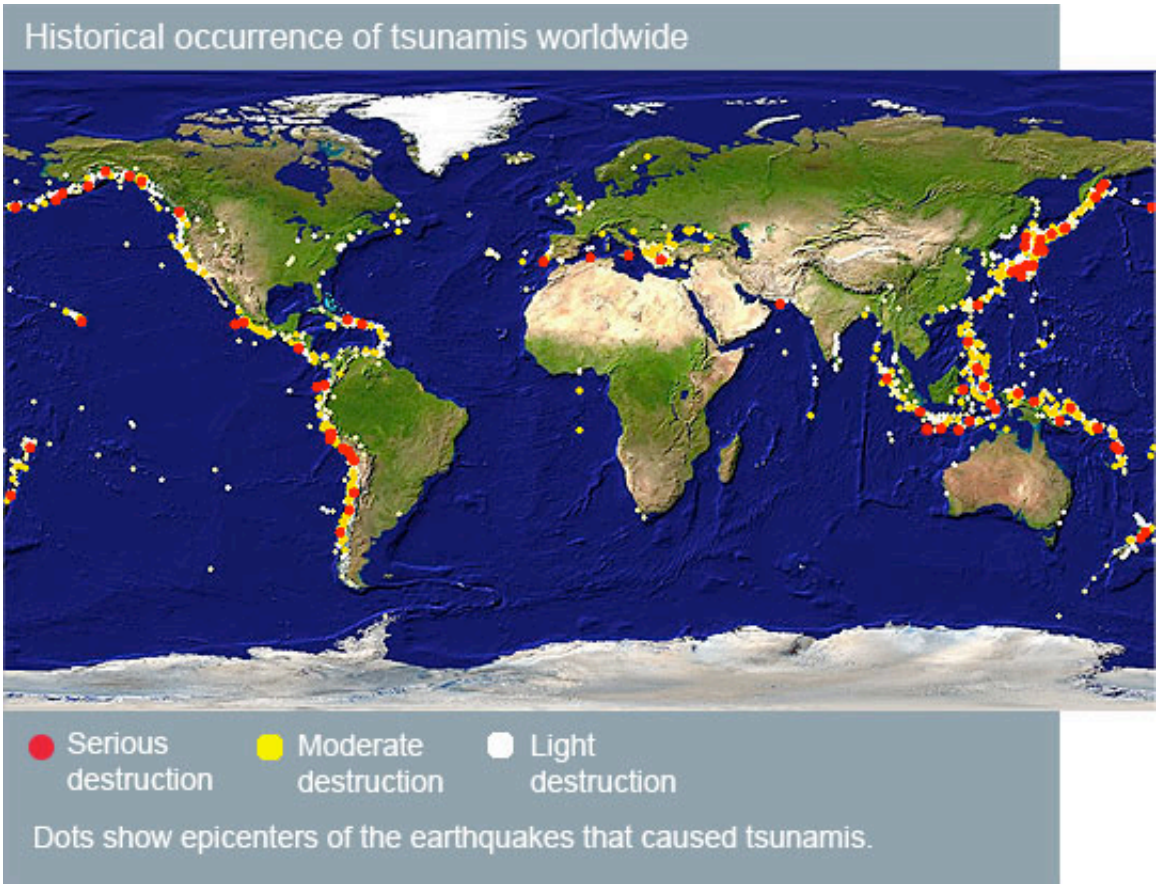

Figure 1.2. World distribution of tsunamigenic earthquakes [http://www.tsunami-alarm-system.com/en/phenomenon-tsunami/phenomenon-tsunami-occurrences.html].

1.4 Tsunamigenic zones and the variability of their tsunami potential

Tsunamis characterized by wave height over a meter or two at the source are not so common. Actually, to build up a wave of this size, a big submarine earthquake greater or equal than magnitude M8.0 must happen. On a global average, about one M8+ earthquake occurs per year. About half of these strike under the ocean with a fault orientation favorable for tsunami excitation. Thus, tsunamis that induce widespread damages are about two to four per decade. Nevertheless smaller tsunamis may be generated by earthquakes with magnitude smaller than M8.

Today, in fact, there are some modern instruments like the ocean bottom-pressure sensors that can detect a tsunami of a few centimeters height in the open sea. Several earthquakes of moderate size (e.g. M6.5) occur around the oceans and they can

generate waves of small size; this kind of tsunamis occur several times per year but, because of their low amplitude, they pass generally unnoticed by the population.

As we observed in the previous section, there is a strong correlation between the geographic distribution of the earthquakes and that of the tsunamis. This correlation mainly concerns the subduction zones that are the most tectonically active regions of the Earth.

We can classify tsunamigenic earthquakes occurring in subduction zones into three types [*Satake and Tanioka,* 1999]: earthquakes at the plate interface (typical *interplate* events), earthquakes at the outer rise, within the subducting slab or overlying crust (*intraplate* events), and ‘‘*tsunami earthquakes*’’ that generate considerably larger tsunamis than expected from seismic waves (Figs. 1.3, 1.4).

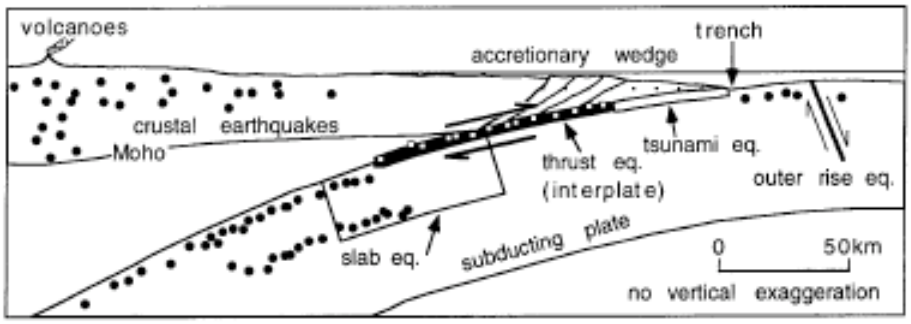

Figure 1.3. Schematic cross section of a subduction zone. ‘‘Typical’’ interplate earthquakes occur at the seismogenic boundary between the subducting and overlying plates. Intraplate earthquakes include outer-rise events, slab events and crustal earthquakes. The source region of ‘‘tsunami earthquakes’’ is beneath the most trenchward part of the accretionary wedge [after *Satake and Tanioka,* 1999].

In accordance with the definition of *Satake and Tanioka* [1999], we can define typical interplate earthquakes those occurring at the seismogenic interface, or megathrust, between subducting and overlying plates. Moreover, we can classify the intraplate earthquakes in two types: if the fault is located outside the trench axis, they are called *outer-rise* events, whereas if the fault is within the subducting slab, we call it a *slab earthquake*.

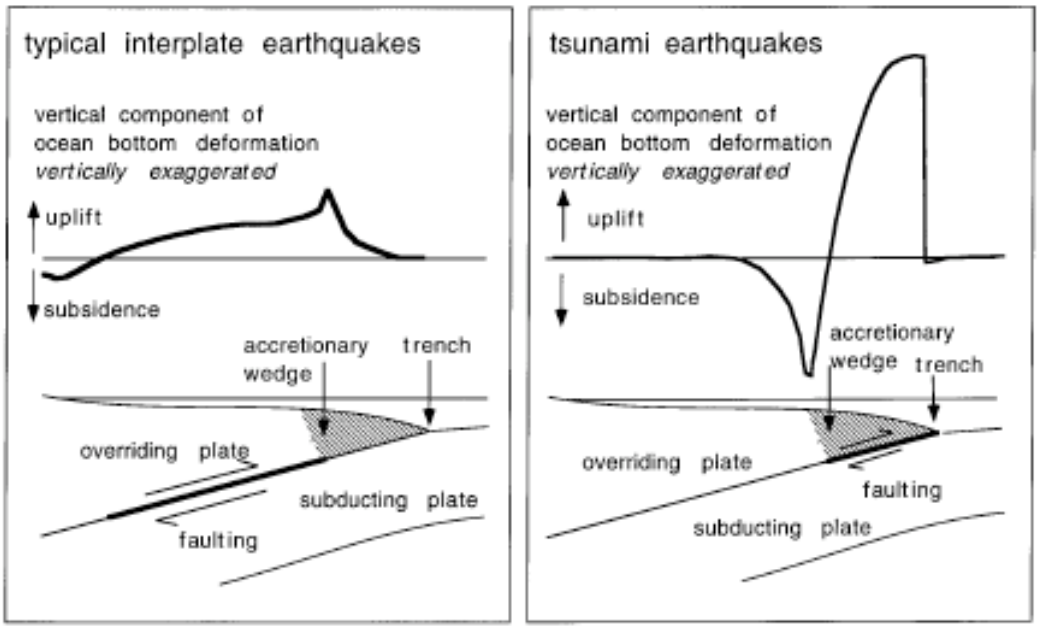

Figure 1.4. Schematic view of the source regions (bottom) and vertical deformation on ocean bottom (top) for typical interplate (left) and tsunami (right) earthquakes. Source region of interplate earthquake typically extends 10 to 40 km depth. Ocean bottom above source region is uplifted and becomes the tsunami source. Source region of tsunami earthquakes is at shallower extension near the trench axis [after *Satake and Tanioka,* 1999].

Finally, if an earthquake generates a much larger tsunami than expected from its seismic waves then we call it a ‘‘tsunami earthquake’’ [*Kanamori*, 1972]. The understanding of the tsunami earthquake and, more generally, the link existing between the earthquake magnitude and the tsunami magnitude is one of the open issues about tsunamis. Actually, it may happen that a large earthquake generate a small tsunami and *vice versa*; an important example is the July 17, 2006 Java earthquake (Mw 7.8) that, even with a lower magnitude, generated waves much higher than the September 12, 2007 Sumatra earthquake (Mw 8.4).

To this end, inferring the source parameters of a tsunamigenic earthquake is crucial to understand the generation of the following tsunami and consequently to mitigate the risk for the people and the damages of the structures along the coasts.

Tsunamigenic Event	Date	Earthquake Magnitude	Runup (meters)
Tokachi-Oki	09/25/2003	**8.1**	**~4**
Sumatra	12/26/2004	**9.1**	**~30**
Nias	03/28/2005	**8.6**	**~4**
Java	07/17/2006	**7.8**	**~8**
Kuril Is.	11/15/2006	**8.3**	**~15**
Kuril Is.	01/13/2007	**8.1**	**~1**
Solomon Is.	04/01/2007	**8.0**	**~0.5**
Peru	08/15/2007	**8.0**	**~0.5**
Chile	11/14/2007	**7.7**	**~0.2**
Sumatra	09/12/2007	**8.4**	**~2**

Table 1.1. List of the recent tsunamigenic earthquakes. It is interesting to notice as the magnitude of the earthquakes not always is correlated with the runup measurements.

Chapter 2

Experimental data

In this section we present a short review of the data that are useful to reconstruct the tsunamigenic source. Of course, these data rely mostly on marine observations, such as tide-gage records, sea level variations captured by ocean bottom-pressure gages and satellite altimetry, but also include on land measurements, like the detection of crustal movements by GPS technique.

2.1 Marigrams

Some marigram is obtained from a gage (stilling well, piezometric, acoustic, etc.) generally installed an harbor, which measures the variations of the sea level. Being present along almost all the coastlines all around the world, the most important advantage of these instruments is that they are characterized by a very good spatial coverage (Fig. 2.1). Nevertheless, there is a strong heterogeneity regarding the technology of instruments; this is a fundamental drawback because, if in some zones – e.g. Japan or United States – there are digital gages with a sampling rate of about 1 minute (Fig. 2.2), 30 seconds or less, in other regions the only operative gages are of analogical type, or with large sampling rates (5 to 15 minutes), mainly because these instruments have been installed to record the ocean tides, that have much longer periods than tsunamis. In these conditions is not always easy or possible to capture details of the tsunami signal, even after a filtering operation to remove the tide from the original record.

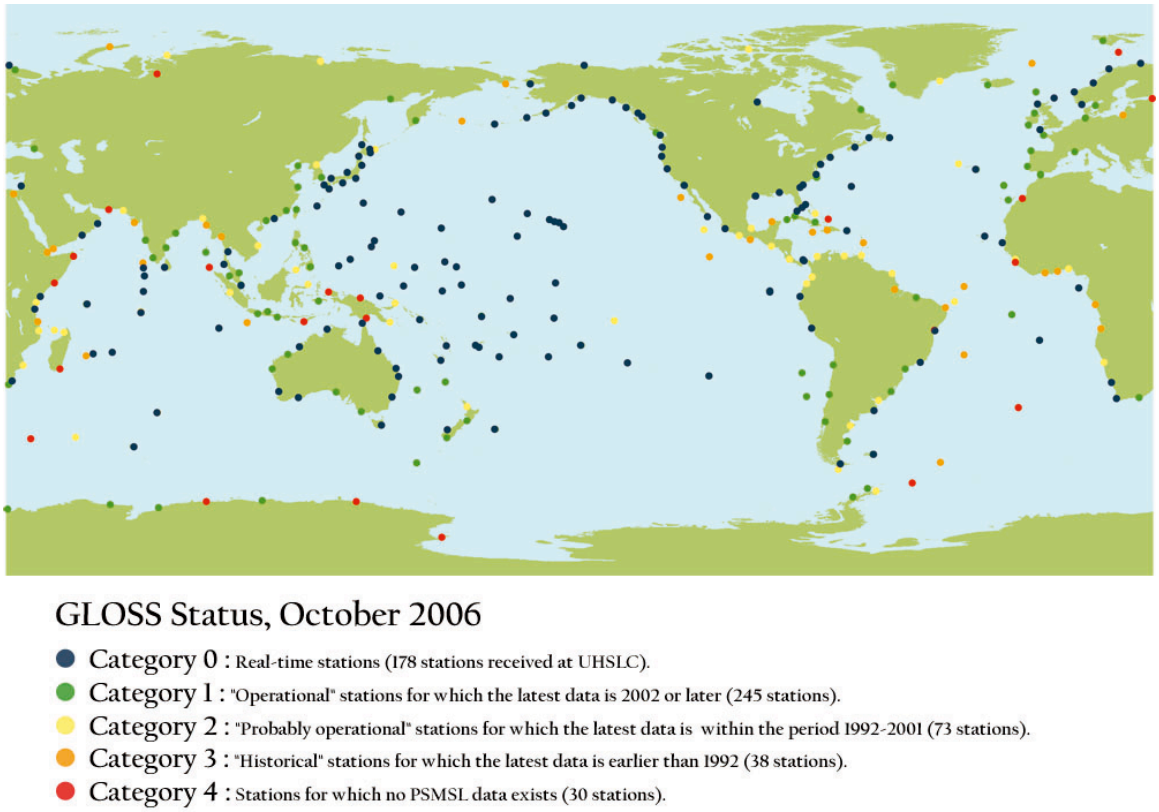

Figure 2.1. World distribution of tide-gages, by GLOSS (Global Sea Level Observing System) [*http://www.gloss-sealevel.org/,* last accessed February 2009].

The up-to-date technology makes a high frequency tide-gage station the cheapest way to measure a tsunami wave. However, since these gages are usually positioned into harbors, the recorded waveforms are affected by local effects due to the bathymetry of the harbor. In fact, the very local bathymetry surrounding the gage operates as a transfer function on the incoming waves and modifies the amplitude and the period of the recorded tsunami, hiding information about the earthquake source; this is the main reason that make somewhat difficult to model such recorded marigrams, especially for the later phases [*Rabinovich,* 1997].

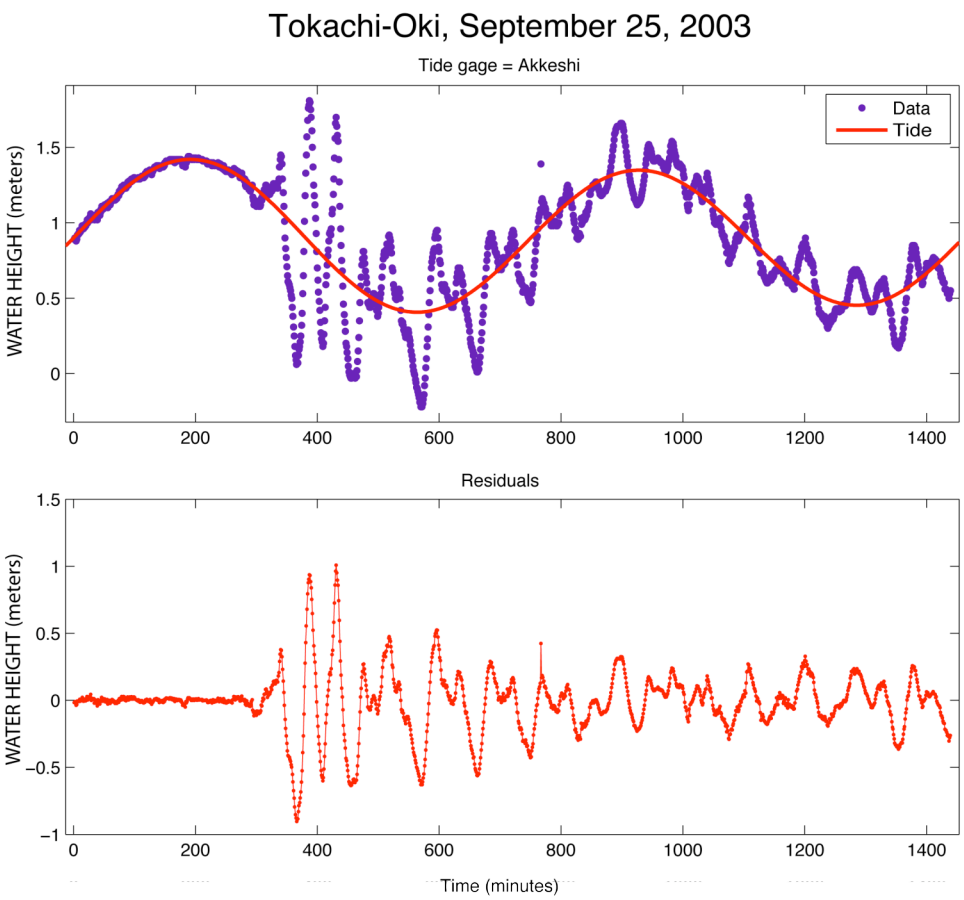

Figure 2.2. Tsunami waveform of the September 25, 2003 Tokachi-oki earthquake, recorded at Akkeshi (Japan) tide-gage. In the upper panel it showed the observed waveform (blue) and the tide (red). Below (red) it showed the observed waveform after removing of the tide.

2.2 Ocean bottom-pressure data

The ocean bottom-pressure gages are instruments positioned on the seafloor, generally at more than 1000 m of depth, that measure the pressure variations there. The pressure exerted on the seafloor depends on the height of the above water column; when a change in the water column occurs, for instance because of the passage of a tsunami wave, this translates into a change of the pressure at the ocean bottom. Being located in the open sea, the waveforms recorded by these instruments are not influenced by local coastal effects, such as amplifications and reflections, as the standard tide-gages placed into the harbors. Moreover, these instruments have a flat response to 0 Hz and, like a "submarine GPS", are able to perfectly detect the static vertical displacement of the seafloor [*Mikada et al.,* 2006].

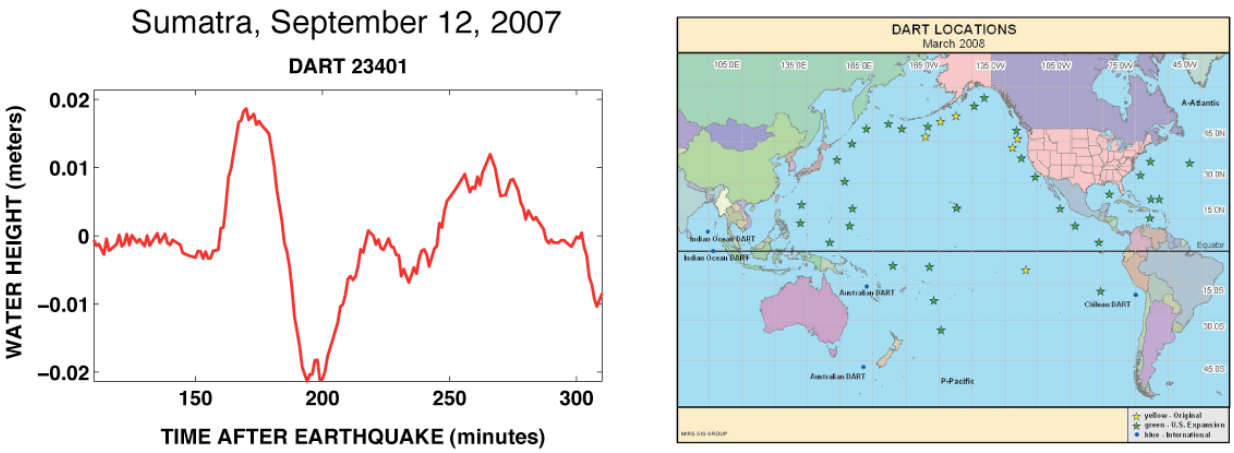

Figure 2.3. In the left panel the tsunami waveform of the September 12, 2007 Sumatra earthquake, recorded at DART buoy 23401 (Indian Ocean). In the right panel the world distribution of the DART buoys.

Unfortunately, this is a relatively recent and expensive technology so that the worldwide coverage is still poor. However, the great 2004 Sumatra tsunami greatly stimulated the interest in such technology and a program to install DART buoys also in the Indian and Atlantic oceans started soon after that event; in only four years the number of operational DART buoys has doubled (Fig. 2.3).

2.3 Satellite Altimetry measurements

In some exceptional cases another useful measurement of the sea level variation can be performed by means of the Satellite Altimetry. Altimeters (e.g. ERS-1, ERS-2, JASON-1 and TOPEX/POSEIDON missions) are sensors that use microwave radar to determine the distance between the satellite and the sea surface directly below [*Hayashi,* 2008]. Although watching for tsunamis is beyond the scope of ongoing altimetry missions, tsunamis can be detected by the change in height of the sea surface during oceanographic monitoring missions, provided that they have the right tracks. Satellite altimetry has the potential to detect large tsunamis [*Okal et al.,* 1999], but no tsunami had been detected clearly from space until the 2004 Indian Ocean tsunami event. Actually, only with the aid of sophisticated techniques is possible at times to retrieve the tsunami signal; in fact some of the detection problems are the unfavorable source directivity in the geometry of existing satellite tracks and the high level of noise at frequencies and wavelengths of interest for tsunamis – including

various effects due to oceanographic, meteorological, geodetic, and seismic phenomena – that blur the tsunami signal if the wave amplitude is not so much high (as was the case for the 2004 Sumatra tsunami, Fig. 2.4).

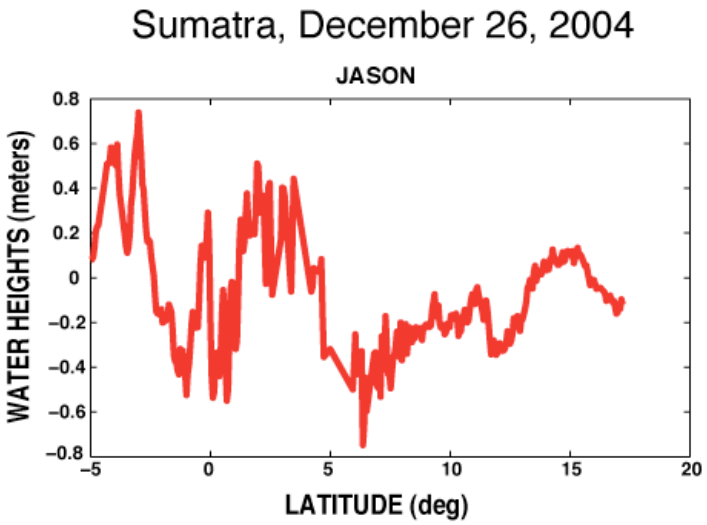

Figure 2.4. Profile of the December 26, 2004 Sumatra tsunami heights along JASON-1 satellite track extracted from satellite altimetry data.

However, since satellite altimetry measurements are carried out in the open sea, they have the same advantage of the oceanic bottom-pressure gages because the local coastal effects do not affect the propagating tsunami waves.

2.4 GPS data

GPS (Geodetic Positioning System) provide crustal measurements that reveal a number of tectonic phenomena, such as coseismic and postseismic displacements due to earthquakes, offering a good constrain regarding the rupture process that generates the tsunami [*Nishimura et al.,* 2005]. However, geodetic measurements are limited to land and therefore the slip distribution is poorly resolved offshore, though well constrained in the landward areas.

These measures are characterized by a very high precision, and the diffusion of these instruments increases day by day. Nevertheless the spatial coverage of these sensors is not always good around the world. Only in some regions, for example in Japan, the

instrumental distribution is excellent; when dealing with the study of the rupture process, as we will discuss in a following chapter, this is a crucial point (Fig. 2.5).

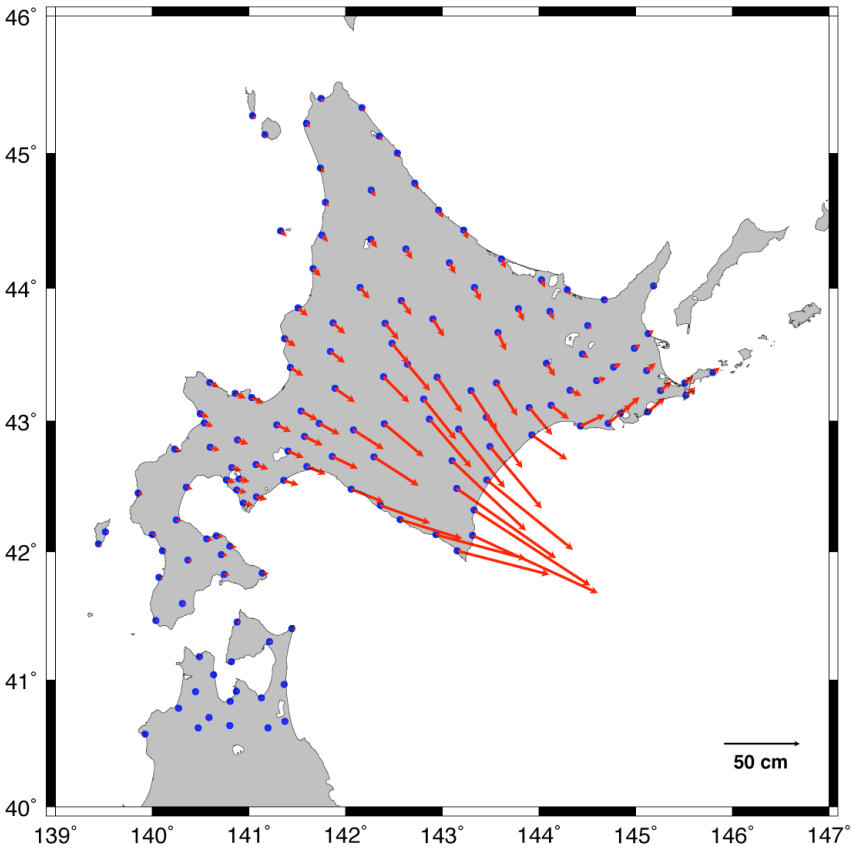

Figure 2.5. Distribution of the GPS stations of the GSI on both Hokkaido and northern part of Honshu region. Red arrows indicate the horizontal coseismic displacement of the September 25, 2003 Tokachi-Oki earthquake.

Chapter 3

Nonlinear inverse method for tsunamigenic sources

The main problem we are facing in this thesis consists in the inversion of different geophysical data to infer some properties about the rupture process of the tsunamigenic source. Let's denote with $\mathbf{d}_{obs}$ the data values (i.e. the actual observations), with **m** the model parameters (i.e. the tsunamigenic source) and with **G** the operator (Green's function) that allows the calculations of predicted data values $\mathbf{d}_{cal}$ given a model **m**. From a mathematical and general point of view, solving an inverse problem consists in finding the model $\mathbf{m}_s$ that minimize in some sense the difference between $\mathbf{d}_{obs}$ and $\mathbf{d}_{cal}$.

This will require the definition of a suitable parameterization of the model, i.e. the tsunamigenic source, then solve the forward modeling problem to compute appropriate Green's functions corresponding to the different data. In general, and this will be the case for the problem we are dealing with, the operator **G** performs a nonlinear mapping between the model space and the data space. This means that the solution cannot be found by solving a linear system of equations; here, we will search for the model solution by means of a global optimization method.

3.1 Fault Parameterization

For large earthquakes, it is usual to consider the fault area as a surface on which the rupture occurs. This surface, eventually subdivided into smaller subfaults, may be, in the simpler cases, a rectangular plane.

On the basis of the focal mechanism of the earthquake, the distribution of aftershocks, the magnitude of the event and the tectonics of the source zone, we may estimate some geometrical characteristics of the source [*Wells and Coppersmith,* 1994], like

the dimensions, the depth and the orientation of the fault and some mechanical parameters, such as the gross amount of the slip, the rake angle, and the hypocenter.
Some of these parameters are fixed, whereas others are not constrained and therefore free to vary, being the parameters we want to infer in our problem.
Each subfault is characterized by 10 parameters: position (Lon, Lat), depth of the upper border, length, width, strike, dip, rake, slip amplitude and the rupture time. Usually the only free parameter is the slip amplitude, in some cases the rake and, if the earthquake is large enough, also the rupture time; we will see some examples in the sections dedicated to the applications.
In some cases, as for the Sumatra 2004 event, we may parameterize the fault plane also with a geometry that is not necessarily regular. For example we could treat the subfaults as rectangles but each with a different strike and each with different dip and/or size.

3.2 Tsunami modeling

Tsunamis are gravity waves that propagate in the ocean, the latter being considered as a homogeneous, incompressible and not viscous fluid. This physical phenomenon is constituted by three phases: the generation, the propagation and the shoaling with the consequent inundation of the coast.
As we have observed in a precedent chapter, the typical tsunami wavelength is on the order of 100 km, whereas the ocean depth is about 4-5 km; in this case we can consider a tsunami as a "long-wave" because its wavelength is much longer than the depth and therefore the Navier-Stokes equations in "shallow-water" approximation are suitable to describe the tsunami propagation.
The shallow water equations are a system of PDEs:

$$\begin{cases} \dfrac{\partial(z+h)}{\partial t} + \nabla \bullet \left[\mathbf{v}(z+h)\right] = 0 \\ \dfrac{\partial \mathbf{v}}{\partial t} + (\mathbf{v} \bullet \nabla)\mathbf{v} = -g\dfrac{\partial z}{\partial x} + \mathbf{C} + \mathbf{F} \end{cases} \qquad (1)$$

where, as we can see in the Fig. 3.1, *z(x,y;t)* represents the water elevation above sea level, *h(x,y)* the water depth in a still ocean, *g* the gravity acceleration, and **C** and **F** represent the Coriolis and the bottom friction forces respectively. This problem is 2D

because the vertical component of the velocity is negligible; actually the **v** horizontal velocity vector (with component *u(x,y,t)* e *v(x,y,t)*) is depth-averaged since we consider the horizontal velocity as a constant along the whole water column.

Physically the first equation of (1) represents the mass conservation, whereas the second and third equations represent the conservation of momentum.

The modeling of the tsunami propagation is performed considering the linear form of (1) since $z + h \cong h$ when the wave amplitude is negligible compared to the depth of the ocean and moreover the advection term $\mathbf{v} \bullet \nabla \mathbf{v}$ can be dropped out along with the bottom friction term, that is

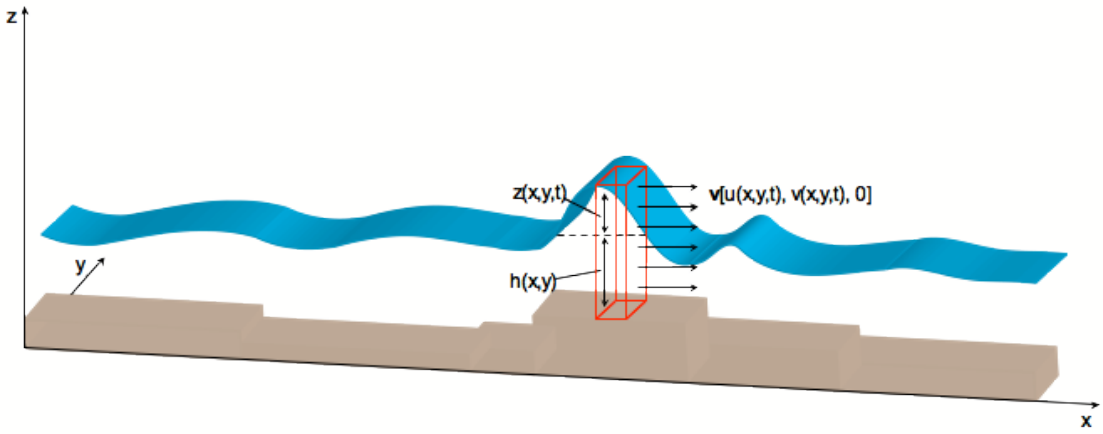

Figure 3.1. Schematic representation of tsunami propagation

$$\begin{cases} \dfrac{\partial (z+h)}{\partial t} + \nabla \bullet [\mathbf{v}h] = 0 \\ \dfrac{\partial \mathbf{v}}{\partial t} = -g \dfrac{\partial z}{\partial x} + C \end{cases} \qquad (2)$$

This system of equations is completed by two boundaries conditions: a pure wave reflection at the solid boundary (coastlines) and full wave transmission at the open boundary (open sea)

$\mathbf{v} \bullet \mathbf{n} = 2(c_1 - c_0)$ open sea

$\mathbf{v} \bullet \mathbf{n} = 0$ coastlines

where $c_0 = (gh)^{1/2}$ is the linear wave phase velocity, $c_1 = \left[g(z+h)\right]^{1/2}$ is the local wave phase velocity and **n** is the unit normal vector at the domain boundary.

Usually, the initial condition that sets in motion the tsunami wave is the seafloor uplift, which instantaneously transfers to the water column; therefore the initial condition is defined by the initial surface elevation field $z(x,y,t_0)=z_0(x,y)$, with the assumption that the initial velocity field is $u(x,y,t_0)=v(x,y,t_0)=0$. These hypotheses are reasonable since the duration of the tsunami generation process (few tens of seconds) is much smaller than the tsunami wave period (few tens of minutes). Nevertheless, if the causative source of the tsunami is not a seismic event, but for example a submarine landslide, the generation process is no longer considered as instantaneous and a time dependent forcing term have to appear in eqs. 1) and 2).

3.3 Green's functions for tsunami waveforms

Once defined a fault area and its parameterization, we have to compute the Green's functions, i.e. the tsunami waveform at a station produced by each subfault with unitary slip (Fig. 3.2); these synthetic waveforms are computed by solving eqs. (1) or (2) by means of a numerical method, here we use a finite difference method on a staggered grid [*Mader,* 2001].

The successive step is to generate the tsunami waveforms as a linear combination of the Green's functions, multiplied by a coefficient that is the actual slip value.

The initial condition for the tsunami, that is the coseismic displacement field affecting the seafloor, is usually computed by considering the Earth as an elastic, isotropic and homogeneous half-space where the rupture of a rectangular fault with uniform slip occurs. According to these hypotheses the deformations are computed through the Okada's analytical formula [*Okada,* 1992]. However, modelling of coseismic displacements, using a layered model is more realistic than a homogeneous half-space, since for a given slip, the surface displacement is usually larger due to the rigidity contrasts, particularly as regards the horizontal components [*Ichinose et al.,* 2007; *Wald and Graves*, 2001].

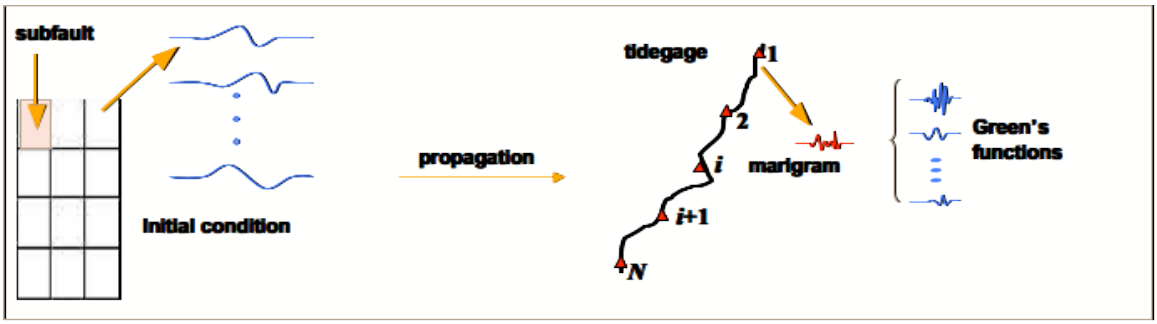

Figure 3.2. Schematic representation of the Green's function for the tsunami waveforms.

Therefore we can compute the vertical coseismic deformation field as initial condition for the tsunami considering a vertical layering of the lithosphere embedding the source zone [*Wang et al.,* 2006]: it has been demonstrated that, for thrust faulting, crustal layering plays a smaller role for the vertical component of the displacement than for the horizontal ones.

Eqs. (2) represent a good approximation as long as the tsunami propagation occurs in open sea; while approaching the shoreline, the water depth becomes smaller and smaller, the non linear effects become relevant and the non linear form of the shallow water equations (eqs. (1)) should be used to describe the tsunami propagation. When entering very shallow water, tsunami waves shoal, i.e. the wavelength shortens and the wave amplitude grows. Of course, to model in a proper way these effects, the spatial resolution of the grid in the nearshore zone, where eqs. (1) are solved, should be very high. On the other hand, since the tsunami propagation is greatly dependent on the depth of the sea, we need also a very detailed bathymetric grid, especially near the locations where the tide-gages are positioned, i.e. in the harbors for instance. A high-resolution bathymetric dataset is not always available in these zones and therefore it is necessary to obviate to this problem, for example by digitizing nautical charts concerning the harbors details, as we will see in one of the applications in a next chapter. The Green's functions for the bottom-pressure gages are computed with the same method followed for the waveforms at the tide-gage stations.

3.4 Green's functions for Satellite Altimetry waveforms

The measure of the water elevation performed by the satellite is not executed in a single point of the space, but actually spanning an area that depends on the

instrument. To compute the Green's functions, i.e. the water elevation at each point of the satellite track produced by each subfault with unitary slip we extract and average (in a region that roughly corresponds to the region spanned by the satellite measure) the values of the water height obtained solving eqs. (2), just taking into account that the altimetry recording is a function of both space and time [*Sladen and Hébert*, 2008].

3.5 GPS modeling

GPS measurements reveal several tectonic phenomena, such as coseismic and postseismic displacements due to earthquakes and offer a valuable constrain on the rupture process, especially for the part of the source close to the land that contributes to the tsunami generation. To model the three components of the coseismic surface displacements we can use different approaches.

Usually, when the GPS stations are positioned in the near field, the way to model the coseismic offset is analogous to the modeling of the vertical deformation field we described in the previous section. As we explained above the geodetic data can be modeled through the Okada's analytical formulas: in this case we assume the Earth to be a flat homogeneous elastic half-space. A more sophisticated method still considers the Earth as a flat elastic space, but introduces a vertical layering of the lithosphere [*Wang et al.,* 2006]: this method is useful to take into account the effects induced by soft shallow crustal layers. A more detailed description of this model is over the purpose of this thesis; in a following section we will explain the set-up of the source parameters we use to employ the method proposed by *Wang et al.* [2006].

On the other hand, there may be special cases, like the great 2004 Sumatra earthquake, for which intermediate to far field ground displacements could be used to study the rupture characteristics; in this case the sphericity of the Earth plays an important role and methods based on spherical harmonics summation may be successfully employed [*Piersanti et al.,* 1995]. In a following section we will briefly illustrate this method, which has been used to model the GPS data recorded for the 2004 Sumatra event.

3.6 Green's functions for geodetic data

Following the same approach used for the tsunami waveforms, we compute the Green's functions for the GPS data. The Green's functions – i.e. the coseismic displacements at a GPS station produced by each of subfaults with unitary slip - are computed by means of the Okada's analytical formulas, the approach of *Wang et al.* [2006], or the spherical harmonics summation, depending on the earthquake at hand. For the two latter methods, we need to define the mechanical properties of the different layers involved.

3.7 Global optimization for nonlinear inverse problem

As we will see in detail in the second part of this thesis, where some applications to real earthquakes are presented, we may simultaneously invert for slip, rake, rupture front velocity, and fault rigidity, depending on the particular event we are dealing with.

We anticipate here that the relation between data and rupture velocity as well as between slip and rigidity is non-linear. A simultaneous inversion of the whole parameter set therefore requires a non-linear inversion method; here we use the "heat bath algorithm" implementation of the *simulated annealing* technique [*Rothman*, 1986]. This technique is based on a large sampling of the model space, and progressive concentration of the search on regions characterized by low values of the cost function, i.e. where the optimal models are likely to be found. Some details of this method are presented in *Appendix A*.

To solve a global optimization problem we need a suitable cost function to minimize. Since we have to do with different datasets then we need also different cost functions, where each of these has to represent the goodness of the fit between the observed and the inverted data.

For the tsunami dataset, which is composed of time series, we used a cost function that has proven to be sensible both to amplitude and phase matching [*Spudich and Miller*, 1990; *Sen and Stoffa*, 1991]. It is expressed as follows:

$$E^{T}(m) = \sum_{k=1}^{N} \left[1 - \frac{2\sum_{t_i}^{t_f} \left(u_o(t) u_s(t) \right)}{\sum_{t_i}^{t_f} u_o^2(t) + \sum_{t_i}^{t_f} u_s^2(t)} \right] \qquad (3)$$

In eq. (3) u_o and u_s are the observed and synthetic waveforms respectively, t_i and t_f are the lower and upper bounds of the time window and N is the number of records used in the inversion.

As regard the geodetic data, instead, we use a standard L_2-norm as a cost function, expressed as follows:

$$E^{GEOD}(m) = \sum_{i=1}^{N_{GEOD}} \left(\frac{u_o - u_s}{\sigma} \right)^2 \qquad (4)$$

where, as for the precedent cost function, u_o and u_s are the observed and synthetic coseismic displacements respectively, σ is the error of the single observed data and N_{GEOD} is the number of geodetic records used in the inversion.

Since we perform a joint inversion then we must compute a total cost function to minimize; we decide to use a weighted mean of the datasets we utilize.

Obviously, as the datasets are different, the single cost functions could be minimized in a different way, that is the cost function of a dataset could decrease too rapidly, unbalancing the result of the inversion in disadvantage of the other dataset. To avoid this difficulty, an efficient way to work is to select different weights after a starting *trial and error* procedure.

3.8 Resolution test

In general, given a parameterization of the source, we do not know a priori if the data at our disposal are sufficient to solve the problem.

For example, the azimuthal coverage of the tide-gage stations and/or the spatial distribution of the GPS stations could be inadequate to constrain the source; in particular, we have to check the size of the subfaults and determine the minimum dimension that permits to infer properly the slip distribution.

Looking at the problem of reconstructing the rupture process of an earthquake, we note that different researchers find different solutions for the same event. This introduces the issue related to the spatial resolution we want to resolve and therefore the necessity to perform some tests before to decide the final parameterization we want to use. By means of these tests, in fact, we are able to assess the reliability of the results of the inversion.

The essential concept is that, because we do not know the true characteristics of an earthquake, it is difficult to evaluate the goodness of the results, and therefore how much the recovered rupture process is close to the reality.

For these reasons, it is a good practice to make preliminary tests with the synthetic data before performing the inversion with the real data.

3.9 Checkerboard test

A typical resolution test is the *checkerboard test*. For instance, when we face the problem of determining the slip distribution, the usual way to proceed is to fix all parameters but the slip amplitude, which is assumed to have a checkerboard pattern, that is with alternating values of the slip onto adjacent subfaults. With this parameterization we model the synthetic data, eventually adding a certain level of noise into them, then we perform an inversion and we verify how much the inverted and the target model are in agreement. In this way we are able to estimate the resolution of our data in relation to the assumed parameterization.

Once we have verified the consistency between the data and the parametric choice, then we perform the inversion with the real data. Nevertheless, it is important to underline that the resolution tests are not a guarantee for reliable result; in fact, the synthetic tests cannot take into account those modeling errors that may bias the results.

3.10 Error estimation

The *best model* is the model that minimizes the misfit between the observed and the calculated data. The Heat Bath Algorithm permits to explore very efficiently the model space, thus guaranteeing that the global minimum of the cost function or a very close value is reached.

However, in many geophysical problems, it has been observed that the data may be fitted very well by many different models [*Sen and Stoffa,* 1995]; this feature demonstrates the non-uniqueness of the solution and that the inverse problem is underdetermined [*Menke,* 1984]. In order to estimate the non-uniqueness of the solution we can follow a statistical approach by analyzing the solution in terms of the probability density functions (pdf) of each parameter of the model space. In this approach we take advantage of the large ensemble of models build up by the simulated annealing algorithm during the search for the best model. We compute an averaged model and the associated standard deviation by weighting all models of the ensemble by the inverse of their cost function values; we may express these quantities as:

$$\langle m_i \rangle = \frac{\sum_{j=1}^{N} \frac{m_{ij}}{E_j}}{\sum_{j=1}^{N} \frac{1}{E_j}} \qquad (5)$$

$$\langle \sigma_i \rangle^2 = \frac{\sum_{j=1}^{N} \frac{\left(m_{ij} - \langle m_i \rangle\right)^2}{E_j}}{\sum_{j=1}^{N} \frac{1}{E_j}} \qquad (6)$$

where $<m_i>$ and $\langle \sigma_i \rangle$ are the averaged model parameter and the associated standard deviation, respectively, N is the total number of models belonging to the ensemble, m_{ij} is the *i-th* parameter of the *j-th* model and E_j is the value of the cost function corresponding to the model $\boldsymbol{m_j}$. These estimates can provide more information about

each parameter and the complete source process studied, being representative of all models that satisfactorily fit the data.

PART 2
Applications

In the next chapters I will illustrate the real cases studied during my Ph.D., showing how depending on the earthquake and the available kind of data is possible to infer different rupture parameters.

In the *Chapter 4* (2003 Tokachi-Oki earthquake) is inferred the slip distribution from a joint inversion of tsunami waveform, GPS, and ocean bottom pressure data.

In the *Chapter 5* (2007 Sumatra earthquake) are inferred the slip distribution and the average rupture velocity by inverting several tsunami waveform.

In the *Chapter 6* (2004 Sumatra earthquake) are inferred the slip distribution, the rake, and the rupture velocity by performing a joint inversion of tsunami waveform, Satellite Altimetry, and GPS data. Moreover, it is proposed a new method to estimate self-consistently the rigidity on the source zone.

Chapter 4

Inverting for the slip distribution: the 2003 Tokachi-Oki earthquake

The 2003 Tokachi-Oki earthquake (Mw 8.1) is one of the most important seismic events occurred in Japan during the last years. In this section we will jointly invert tsunami waveform, GPS, and ocean bottom-pressure data, to infer the slip distribution onto the fault area. This earthquake occurred near the Kuril trench and a large part of the fault plane was positioned offshore. We show that GPS data on land allow to well constraining the slip distribution onshore, whereas the tsunami data are very sensitive to the slip distribution offshore. The joint inversion of tsunami and geodetic data has revealed a much better constrain for the slip distribution on the fault rather than the separate inversions of single datasets. The study of the Tokachi-Oki earthquake, in particular, demonstrates that the installation of offshore geodetic stations could have important implications in the planning of tsunami warning systems, and therefore it could help to mitigate the tsunami risk along the coastlines.

This work resulted in the following research paper submitted to *Journal of Geophysical Research*:
Romano F., S. Lorito, A. Piatanesi, and K. Hirata (2009), Slip distribution of the 2003 Tokachi-Oki (Japan) Mw 8.1 earthquake from joint inversion of tsunami waveform and geodetic data.

Part of this work has been also presented at the 2008 European Geophysical Union (EGU), where I have received the *Young Scientists' Outstanding Poster Paper* (YSOPP) Award for my poster presentation "**Rupture process of the September 25, 2003 Tokachi-Oki (Hokkaido, Japan) Mw 8.3 earthquake from joint inversion of tsunami waveform and GPS data**" in the scientific session "*NH6.1 Tsunamis*".

Slip distribution of the 2003 Tokachi-Oki (Japan) Mw 8.1 earthquake from joint inversion of tsunami waveform and geodetic data

Romano[1] F. , S. Lorito[1], A. Piatanesi[1], and K. Hirata[2]

[1] Istituto Nazionale di Geofisica e Vulcanologia, Department of Seismology and Tectonophysics, Via di Vigna Murata 605, 00143 Rome, Italy

[2] Institute for Research on Earth Evolution, Japan Agency for Marine-Earth Science and Technology, Yokosuka, Japan

Abstract

We studied the September 25, 2003 Tokachi-Oki earthquake, a great inter-plate event (M8.1) occurred at the southwestern end of the Kuril trench offshore Hokkaido, Japan, that generated a significant tsunami. We aim to infer the earthquake slip distribution performing a joint inversion of tsunami waveforms and geodetic data, measured by tide-gages, inland GPS stations, and two ocean bottom Pressure Gages (PG). This is the first inversion joining tsunami and geodetic data for this event. First of all, we performed several checkerboard tests, in order to assess the resolution of the datasets on the slip distribution details. We found that the tsunami data constrain very well the slip distribution offshore, whereas the coseismic GPS data in the onshore zone; the two PG data-points constrain the offshore slip only in a gross sense. Thus, combining the different datasets significantly improves the inversion's results. We then performed a joint inversion in the case of the 2003 Tokachi-Oki earthquake, and we found that the maximum values of the slip (5-7 meters) are located well down-dip of the epicenter and with a patch of slip (5 meters) in the deepest part of the source (~50 km of depth). The latter patch was absent or misplaced in some previous studies based on single datasets. Our findings support the implementation of dense networks of bottom pressure gages close to subduction zones, and their integration in real-time tsunami forecast systems.

1. Introduction

The Tokachi-oki earthquake (M8.1), that took place on 2003 September 25, was one of the most important seismic events in the last 50 years in Japan. This event occurred at 19:50:07 UTC, had an epicentre located at 41.780° N, 144.079° E (Fig. 1) – very close to the 1952 Tokachi-oki event [*Hirata et al., 2007*] – and at a depth of 25 km [*Koketsu et al., 2004*].

Large and tsunamigenic earthquakes occur frequently on Hokkaido Island (northern Japan) because it lies onto the Okhotsk Plate [*Bird, 2003*], and the Pacific Plate subducts at the Kuril trench just under the Hokkaido region (Fig. 1). Several tsunamigenic earthquakes occurred in the last 50 years in this region, as for example the 1952 Tokachi-Oki (M8.2), the 1958 Etorofu (M8.1), the 1963 off Urup (M8.1), the 1973 Nemuro-Oki (M7.7) and the 1994 Hokkaido Toho-Oki (M8.1) [*Hirata et al., 2007*; *Watanabe et al., 2006*].

The average recurrence interval estimated for great earthquakes along the Kuril trench is about 70 years [*Yamanaka and Kikuchi,* 2003]. However, the 2003 Tokachi-oki earthquake occurred only 50 years after its forerunner in 1952 [*Sawai et al.,* 2009], even if its source included only the western half of the 1952 rupture area [*Nakanishi et al.*, 2004; *Tanioka et al.*, 2004a]

The 2003 event caused at least 589 injuries, extensive damages, landslides and power outages and many roads damaged in southeastern Hokkaido; furthermore the event generated a large tsunami along the southern coast of Hokkaido, with runup heights higher than 4 m at some locations [*Tanioka et al., 2004b*]. The tsunami was recorded along the coasts of both Hokkaido and Honshu islands by the Japanese tide-gages network; the surface displacement due to the earthquake was recorded by the many GPS stations present onto such islands. The vertical component of the coseismic displacement was clearly captured also by two Pressure Gages (PG) installed on the seafloor near the Kuril trench (Fig. 1) [*Mikada et al., 2006*].

In previous studies, the 2003 Tokachi-Oki earthquake has been analyzed following different approaches and using various geophysical datasets. The seismic source has been investigated using tsunami travel-times [*Hirata et al., 2004*], and performing a tsunami waveforms inversion [*Tanioka et al., 2004a*], but also using teleseismic data inversion [*Yamanaka et al. 2004; Horikawa, 2004*], strong motion data [*Honda et al., 2004*], teleseismic and strong motion data jointly [*Yagi, 2004*], and finally combining

geodetic and strong motion data [*Koketsu et al., 2004*].

In this study we performed, for the first time as regards this event, a joint inversion of geodetic and tsunami data. The fault planes of the subduction zones have, generally, one portion beneath the land and the other one beneath the ocean seafloor. Thus tsunami waveforms and PG data serve basically to constrain the slip distribution on the fault plane in the offshore zone, and GPS data to constrain principally the slip onto the onshore zone [*Satake, 1993*]. Therefore, in order to infer the slip distribution for the Tokachi-Oki earthquake, we performed a joint inversion of both the tsunami and geodetic datasets.

In what follows, we first describe the datasets and their pre-processing, then the methods for calculating the Green's functions relative to each of them, and finally the parameterization of the source adopted in this study. Later, synthetic checkerboard tests are used to assess the resolving power that the data have on the slip distribution, both for separate and joint inversions. Finally, the results of inversions for the Tokachi-Oki earthquake are shown and discussed.

2. Data

The tsunami generated by the 25 September, 2003 Tokachi-Oki earthquake was recorded at several tide-gages along the coasts of the Japan. These recordings are provided by Japan Meteorological Agency (JMA), the Hokkaido Regional Development Bureau (HRDB) of the Ministry of Land, Infrastructure and Transport, and the Hydrographic and Oceanographic Department (HOD) of the Japan Coast Guard [*Hirata et al., 2004*]. We used in this work only 16 tsunami waveforms (Tab. 1, Fig. 1): 10 digitally recorded at stations located in Hokkaido and 6 digitally recorded at stations in northern Honshu. We selected only those waveforms with an acceptable signal to noise ratio, and excluded those with a hardly distinguishable tsunami signal. On the other hand we paid attention to preserve as far as possible the azimuthal coverage around the earthquake source. The selected recordings were sampled at 1 minute and included the ocean tide. Therefore, we removed the tidal component as inferred by fitting it with a sum of three harmonics. Moreover we chose, for each waveform, a time window including only the first oscillations of the tsunami wave; in this way we attempt to minimize the contribution of local effects to the tsunami signal (reflections, resonance of the bays etc.) that could hide the

information about the seismic source, and that are more difficult to model.

The displacement associated to the earthquake was recorded at several GPS stations of the GEONET system, maintained by the Geographical Survey Institute of Japan. We chose 140 datapoints (Fig. 1), recorded by stations distributed onto Hokkaido and the northern part of Honshu, i.e. those that recorded a significant coseismic displacement. These GPS data have a sampling rate of 1 day, and were downloaded from the website of Geographical Survey Institute [http://mekira.gsi.go.jp/ENGLISH/index.html].

To derive the static coseismic offsets, we have taken into account pre- and post-event trends in the records, and processed them following the procedure described in *Banerjee et al.* (2007).

First we determined, separately, the best-fit straight line for the displacements regarding the 9 days before the Tokachi-Oki event and those for the 10 days after the event; then we extrapolated from these straight lines the times t_0 and t_1 corresponding to the preseismic and postseismic instants respectively, just prior and after the earthquake. Finally, we estimated the coseismic offsets for each GPS stations as the difference between the coseismic measurements extrapolated at t_1 and t_0 (Fig.2, Tab.2). Moreover we estimated the errors for these offsets as the standard deviation of the daily preseismic time series (Tab.2).

The vertical component of the coseismic displacement has been recorded even on the seafloor, by the bottom Pressure Gages (PG), labelled as PG1 (depth 2218 m) and PG2 (depth 2210 m). Even these data are available on the web [http://www.jamstec.go.jp/scdc/top_e.html]. In this work we used the vertical coseismic static offsets at the PG's estimated by *Mikada et al.* [*2006*] (Tab. 2).

3. Modeling and Green's functions

We computed both horizontal and vertical coseismic displacements, at the GPS and PG stations as well as the initial condition for the tsunami propagation, using a layered Earth's model, and by means of the PSGRN/PSCMP numerical code [*Wang et al.,* 2006]. A layered model is more realistic than a homogeneous half-space [e.g. *Okada,* 1992], since for a given slip, the surface displacement is usually larger due to the rigidity contrasts, particularly as regards the horizontal components [*Ichinose,* 2007*; Wald and Graves*, 2001; *Zhao et al.*, 2004].

The PSGRN/PSCMP code needs both the P and S wave velocities and the density values for each of the layers as input parameters; we used values from the vertical cross-sections along lines F–F' as reported by *Wang and Zhao* (2005). Here we used four layers, whose parameters are listed in Tab. 3.

The initial seawater elevation is assumed to be equal to the coseismic vertical displacement of the sea bottom, while the initial velocity field is assumed to be identically zero. To model the tsunami propagation, we used the nonlinear shallow water equations, including the Coriolis force. The boundary conditions are pure wave reflection at the solid boundary (coastlines) and full wave transmission at the open boundary (open sea),. The bathymetric grid for the computational domain depicted in Fig. 1 has 10 arc-seconds of spatial resolution and was provided by HOD (*Hydrographic and Oceanographic Department of Japan*). The equations are solved numerically by means of a finite difference technique on a staggered grid [*Mader*, 2001].

4. Fault parameterization

We chose the source area basing on the aftershock distribution [*Ito et al., 2004*], (Fig. 1) and the geometry of the fault basing on the focal mechanisms calculated by JMA and CMT, modifying them slightly in order to be consistent also with the geometry of the subducting plate proposed by *Bird* (2003): the strike of the fault is 225°, the slip direction is 109° (Fig. 1). The length of the fault is 180 km and its width is 150 km (Tab. 4). Following *Katsumata et al.* (2003) and *Hirata et al.* (2003) we opted for a variable dip angle ranging from 9° at 11 km depth to 24.6° at a depth of about 60 km. We divided the entire fault area into 30 subfaults with a size of 30 x 30 km each (Fig. 1), with the top of the shallowest subfaults at a depth of about 11 km and the top of deepest subfaults at a depth of about 42 km.

5. Inversion

The aim of this study is to retrieve the slip distribution from tsunami and geodetic data. To solve this inverse problem we used the "heat bath algorithm" [*Rothman*, 1986] implementation of the simulated annealing technique, following previous studies using tsunami, geodetic, and strong motion data [e.g. *Piatanesi and Lorito* (2007); *Piatanesi et al.* (2007); *Lorito et al.* (2009)]. We compared the observed and

synthetic datasets by means of two different cost functions for the tsunami and the geodetic datasets. For the tsunami dataset, which is composed of time series, we used a cost function that has proven to be sensible both to amplitude and phase matching [*Spudich and Miller*, 1990; *Sen and Stoffa*, 1991]. It is expressed as follows:

$$E(m) = \sum_{k=1}^{N} \left[1 - \frac{2\sum_{t_i}^{t_f} (u_O(t) u_S(t))}{\sum_{t_i}^{t_f} u_O^2(t) + \sum_{t_i}^{t_f} u_S^2(t)} \right]_k \qquad (6)$$

In eq. (6) u_O and u_S are the observed and synthetic waveforms respectively, t_i and t_f are the lower and upper bounds of the time window and N is the number of records used in the inversion. On the other hand, for the geodetic dataset, we used a standard L_2-norm as a cost function to quantify the misfit between experimental and synthetic datasets.

As regards the joint inversion, the global cost function is a weighted sum of the cost functions for the single datasets. We introduce *a-priori* information in the solution by imposing lower and upper bounds to the range of variation of the source parameter – the slip - and on their steps between extreme values. The slip value is allowed to vary between 0-10 meters on each subfault, at 0.5 meters steps.

Inversion of tsunami data: checkerboard test

We start with evaluating the resolution of the tsunami data. Thus, to check the effectiveness of our method to invert the slip distribution, we performed a series of synthetic tests [*Piatanesi and Lorito*, 2007; *Lorito et al.*, 2008a; *Lorito et al.*, 2008b].

Figure 3a depicts the synthetic target source model we used in the synthetic tests. It consists of a slip distribution featuring a checkerboard pattern, with slip values switching between 1 and 3 meters upon adjacent subfaults. We corrupted the resulting synthetic waveforms by adding a Gaussian random noise with a variance that is 10% of the clean waveform amplitude variance [*Sen and Stoffa*, 1991; *Ji et al.*, 2002], in order to mimic modeling uncertainties.

During a preliminary step of this work we moreover performed some tests with smaller subfault's size (not shown). We observed that, given the present dataset, 30x30 km is very close to the mimimum size for resolving details of the slip distribution.

Our findings indicate that the source process is fairly well constrained by the tsunami data. The best model we found is in fact very similar to the target one: the checkerboard shape of the slip distribution is very well reproduced (Fig. 3b, column 2 of Tab. 5), with a maximum difference between inverted and target values of 1 meter. Nevertheless, a more careful observation of the retrieved slip distribution reveals that the checkerboard pattern is perfectly recovered only onto the offshore zone of the fault area; whereas in the onshore zone the checkerboard pattern still exists, but the residuals between the target and the solution are higher. This supports the general conclusion that tsunami data constrain better the offshore than the onshore rupture features [*Satake*, 1993].

Inversion of Geodetic data: checkerboard test

To evaluate the resolution of the geodetic dataset, we repeated the checkerboard test with the GPS and PG data. The target model is the same as in the same test with the tsunami data (Fig. 4a). We added to the components of each synthetic GPS data point, as well as for the PG's, a random value extracted by a Gaussian distribution, with a variance equal to the square of the error on the real data.

In this case the resolution test has given a positive result only for the portion of the fault plane in the onshore zone or very close to it. In fact, the checkerboard pattern of the slip distribution is well reproduced only on the subfaults sufficiently close to the GPS stations and degrades departing from the coast, despite of the almost perfect agreement (not shown) between the synthetic and the inverted displacements vectors (Fig. 4b and Tab. 5, col. 3).

This result confirms that the geodetic data constrain better the onshore rupture features, whilst they are not sufficient to constrain the slip distribution offshore, despite of the presence of the (very few) PG data.

To support this evidence we performed two further checkerboard tests.

Firstly, we imposed very big patches of slip in the target model: 60x60 km instead of 30x30 km. We imparted, once again, slip values switching between 1 and 3 meters on

the broader adjacent subfaults. We added noise to the synthetic dataset like in the precedent case. In this case the target pattern is perfectly recovered (Fig. 5a, and Tab. 5, col. 4). This confirms that the geodetic dataset has a lower resolving power for the fault geometry we are considering. Secondly, we "virtually" shifted the fault plane below the Hokkaido region, but conserving the initial size of 30x30 km for the subfaults, in order to mimic a very good instrumental coverage immediately above and around the fault zone. We observe that, as in the case of broader subfaults, the checkerboard pattern is perfectly recovered (Fig. 5b, and Tab. 5, col. 5). This test is in some sense the "dual case" of the experiment of *Nishimura et al.* (2005), who place on the seafloor a "virtual" geodetic network, and obtain consistent findings.

Joint inversion: checkerboard test

In view of the different and complementary resolution of two datasets – tsunami and geodetic data – we performed one more checkerboard test: a joint inversion combining the two kinds of data.

The setup of the target source is the same as in the case of the tsunami dataset, i.e. with alternating slip values of 1 and 3 meters on the 30 km squared subfaults (Fig. 6a).

The results of the checkerboard test are totally satisfactory (Fig. 6b, Tab. 5, col. 6), as the slip distribution is now perfectly reproduced. The combination of tsunami and geodetic datasets is then, in principle, efficient to constrain the source process. We will then perform a joint inversion to estimate the slip distribution of the 2003 Tokachi-Oki earthquake. Nevertheless, before doing this, we will perform two separated inversions for the Tokachi-Oki earthquake, one for each dataset, to compare the different source models on the base of the evidences offered by the synthetic tests.

Inversion of tsunami data: Tokachi 2003 earthquake

By means of an inversion of the observed tsunami dataset, and with the same fault parameterization of the checkerboard tests, we aim to retrieve the source process of the September 2003 Tokachi-Oki earthquake.

The results are shown in Fig. 7a. The numerical values of inverted slip are listed in Tab. 6 (col. 2).

The source model we estimated for the 2003 earthquake features the maximum slip concentration close to and downdip of the epicenter. Immediately beneath the epicenter there is a patch with a slip value of 6 meters. In the deep part of the fault instead there are 4 subfaults with slip values between 5 and 7 meters. Other slip values are smaller and more or less distributed around the epicenter.
The comparison between the experimental and synthetic datatasets, computed with the best source model provided by the inversion, is shown in Fig. 7b. We observe that the amplitudes of the synthetics waveforms reproduce very well the experimental one; conversely, the phases are not always perfectly matching.

Inversion of geodetic data: Tokachi 2003 earthquake

The next step has been to retrieve the source process of the September 2003 Tokachi-Oki earthquake, this time by means of an inversion of the observed geodetic datasets.
The results are shown in Fig. 8a. The numerical values of the inverted slip are listed in Tab. 6 (col. 3).
The source model based on geodetic data features the maximum slip concentration on the patches close to the hypocenter, as it was in the case of the tsunami data inversion. In this zone, there is one subfault with slip value of 7 meters just at the hypocenter, whereas further slip concentration is deeper, as located north of this patch, and with lower values (3-5 meters).
The comparison between the experimental and the synthetic datasets is shown in Fig. 8b,c. The fit between the real and inverted horizontal coseismic displacements at the GPS positions is very good as well as for the vertical coseismic displacements at the GPS and PG sites.

Joint inversion: Tokachi 2003 earthquake

Finally we performed a joint inversion of tsunami and geodetic data.
Our best model, as retrieved by the joint inversion, is shown in Fig. 9a. The numerical values of the slip model distribution are listed in Tab. 6 (col. 4).
The source model we estimated for the 2003 Tokachi-Oki earthquake features the maximum slip concentration on the patches at deep southeast of the epicenter. In this zone, the higher slip values are in the range of 5-7 meters, and the remainders are lower and essentially distributed around the epicenter.

We compared once again the experimental datataset and the synthetic one (Fig 9b,c,d). The inverted tsunami waveforms fit very well the real tsunami waveforms at the tide-gages; as in the prior tsunami dataset inversion this agreement is very good particularly for the amplitudes whereas it is not always perfect for the phases of all the tide-gages. Furthermore, we observed that the fit between the synthetics and observed displacements is fairly good. The discrepancies are probably to be attributed to the size of the subfaults, or to *a-priori* fixed slip direction (rake).

The errors on the model parameters are estimated, following *Piatanesi and Lorito* (2007), by means of *a-posteriori* analysis of the ensemble of models explored during the search for the best model, and using only those models having a cost function value not exceeding the minimum by more than 1%. We first calculated the average model, and then estimated the errors as the weighted standard deviation for each of the parameters. Both the average model (Fig. 10a) and the associated errors are reported in Tab. 6 (col. 5). In the average model, the major slip values are lower than those of the best model, and despite the slip values never vanishes the general pattern is conserved. The match between the synthetic dataset calculated with the average model and the real data (Fig. 10b,c,d) is nonetheless still comparable to those obtained with the best model (Fig. 9b,c,d). This indicates that the class of acceptable models for this earthquake is quite broader than the best model itself, and the latter is meant to be just an end-member of a broader ensemble of "good" solutions.

6. Discussion

When performing the checkerboard tests we noticed a substantial difference between using either the tsunami data alone or the geodetic data alone. We have observed that each single dataset is very sensitive for a certain part of the source to resolve the slip distribution. Indeed, on one hand the checkerboard pattern is perfectly resolved in the offshore zone when inverting only for the tsunami waveforms, on the other hand, inverting only for the geodetic data permits to resolve the slip only on the portion of the fault closest to the instruments. To confirm this result we shifted the entire fault beneath the Hokkaido region (in an unreal tectonic configuration, but useful for our purpose); the result of the inversion supports this hypothesis - the checkerboard pattern is perfectly reproduced. Hence, our checkerboard test, points out that the tsunami waveforms and the geodetic data are differently sensitive to the slip

distribution on the fault. In fact, in other studies bigger subfaults than here are used [*Nishimura et al. 2005; Baba et al. 2006*]. We used also two geodetic measurements obtained by two bottom pressure gages located near the Kuril trench; however we observed that these two geodetic data improve only slightly the resolution – having a mutual distance much bigger than the size of the single subfault – and therefore this points out the importance to install offshore a network sufficiently dense of geodetic instruments to better monitor the seismic displacements near the subduction zones, as highlighted by *Nishimura et al.* [2005].

The features individuated in the checkerboard tests are reflected by the results of real data inversions. This is revealed by comparison of the results of the joint inversion with those of the single dataset's inversions. Indeed, we observe in Figure 9 that the patches of slip immediately close to the GPS stations are essentially the same obtained by inverting only the geodetic data (Fig. 8). On the other hand, in the offshore part of the fault, the slip distribution is in agreement with the results obtained inverting only for the tsunami data (Fig. 7).

We noticed that the phases are not perfectly matched for all the tide-gages. In particular, this mismatch occurs for the gages close to the source and likely it depends on size and position of the subfaults. Considering L as the dimension of each subfault and $v = \sqrt{gh}$ as the wave velocity in open sea (linear approximation), where h is the depth ocean, then the wave travels over a subfault in a time $\Delta T = L/v$. This time (ΔT =~5 minutes, if h=~1000 m and L=30 km) is comparable or larger than the observed phase mismatches; therefore a position slightly different of the subfault could be useful to reduce the temporal mismatch. For example, if we consider the Tokachikou tide-gage and we compare it with the same fit obtained by *Tanioka et al.* [2004a] (see the tide-gage Hiro) we notice that there the phase is correct. Actually, in that work the positions and the size of the subfaults are slightly different from ours, and moreover there are not patches of slip in the deepest part of the fault, which instead contribute to our waveforms. Using a smaller size for the subfaults could help to fit much better the tsunami waveforms; however after several preliminary tests we noticed that 30x30 km represents the spatial resolution limit.

We observe that slip values around 6-7 meters, and positioned down-dip of the epicenter, are fairly consistent to those obtained with the joint inversion of teleseismic and strong motion data performed by *Yagi* [2004].

On the other hand our slip values are slightly higher than slip values obtained inverting only for the tsunami waveforms [*Tanioka et al.,* 2004a]. However, we here used a layered Earth's model, which may require slightly more slip to obtain the same surface displacement, and depends strongly on the underlying rheological model. Another difference here is the size of the subfaults that, being smaller, may require more slip while conserving the total moment. It is nevertheless possible that this depends on the finer grid resolution used by *Tanioka et al.* [2004a], and in this case we should have used the same grid. All of these aspects would be worth of further investigations.

If we consider the slip distribution inferred by means of a geodetic data inversion [*Koketsu et al.,* 2004], we can see that they find only one asperity downdip of the hypocenter. Conversely, we found two asperities, one immediately below the hypocenter and another one in the deepest part of the fault. This deep patch of slip (5 meters) appears in *Yagi* [2004], but not in other inversions that use geodetic or tsunami data. However, we use a fault plane more extended downdip; actually, some slip distributions [e.g *Tanioka et al.,* 2004a] have the maximum slip values just on the deepest part of the fault and this likely means that could have continued downdip.

Our best model features a seismic moment of 1.86 x 10^{21} N•m (using as shear modulus the values derived by the layering, see Tab. 3), corresponding to a magnitude $M_w = 8.11$ earthquake; our average model instead features a seismic moment of 2.01 x 10^{21} N•m, corresponding to a magnitude $M_w = 8.13$ earthquake.

7. Conclusions

This is the first time that both tsunami and geodetic data (GPS and vertical seafloor uplift obtained by ocean bottom pressure gages) are jointly used to infer the rupture process of the 2003 September 25 Tokachi-Oki earthquake. We performed some synthetic tests to estimate the sensitivity of the data at our disposal to resolve the slip distribution on the fault area. We observed the different efficiency of tsunami and geodetic data; the former permit to resolve the rupture in the offshore zone, and the latter in the onshore zone. Moreover we noticed that using few geodetic data in the offshore zone contribute slightly to resolve the slip on the entire fault plane. Performing another kind of test we noticed that the resolution of the slip distribution is strongly dependent on the position and the density of the GPS network. It is

possible that a very dense network of instruments able to provide information about the displacement of the ocean seafloor – like the ocean bottom pressure gages – can help to constrain in a much better way the tsunamigenic rupture processes. And, of course, this would be crucial for a real-time forecast system, as the details of the slip distribution counts for tsunamis attacking coasts in the near-field of the source. Using jointly the two datasets permits to resolve the slip on the entire fault, confirming that, as at state of the art, i.e. in absence of sufficient data offshore, the tsunami data are very important to better constrain the rupture processes in the subduction zones. Finally, the slip distribution of the 2003 Tokachi-Oki event inferred in this work, as regard the slip peak values, the positions of the asperities as well as the corresponding seismic moment (M_w = 8.1) reconciles the previous inversions involving other kinds of geophysical datasets.

Acknowledgments

We would like to thank the Japan Meteorological Agency, the Hokkaido Regional Development Bureau of the Ministry of Land, Infrastructure and Transport, and the Hydrographic and Oceanographic Department of the Japan Coast Guard, for giving us the digital tide-gage records and the bathymetric dataset.

We also gratefully thank Claudia Piromallo for the precious suggestions, and Zhi Wang for kindly providing with us the velocity profiles data.

Some of Figures in this work were drawn using GMT software [*Wessel and Smith,* 1995].

References

Baba T., K. Hirata, T. Hori, and H. Sakaguchia (2006), Offshore geodetic data conducive to the estimation of the afterslip distribution following the 2003 Tokachi-oki earthquake, *Earth Planet. Sci. Lett. 241*, 281 – 292, doi:10.1016/j.epsl.2005.10.019.

Banerjee P., F.F. Pollitz, B. Nagarajan, and R. Bürgmann (2007), Coseismic Slip Distributions of the 26 December 2004 Sumatra–Andaman and 28 March 2005 Nias Earthquakes from GPS Static Offsets, *Bull. Seismol. Soc. Am., 97*(1A), S86-S102, doi:10.1785/0120050609.

Bird P. (2003), An updated digital model of plate boundaries, *Geochem. Geophys. Geosystems 4*, doi 10.1029/2001GC000252.

Hirata K., E. L. Geist, K. Satake, Y. Tanioka, and S. Yamaki (2003), Slip distribution of the 1952 Tokachi-Oki earthquake (M8.1) along the Kuril Trench deduced from tsunami waveform inversion, *J. Geophys. Res., 108*(B4), 2196, doi:10.1029/2002JB001976.

Hirata K., Y. Tanioka, K. Satake, S. Yamaki, and E. L. Geist (2004), The tsunami source area of the 2003 Tokachi-oki earthquake estimated from tsunami travel times and its relationship to the 1952 Tokachi-oki earthquake, *Earth Planets Space 56*, 367–372.

Hirata K., K. Satake, Y.Tanioka and Y.Hasegawa (2007), A Review on recent studies of tsunamis in the southernmost Kuril Trench, *Proceedings of International Workshop on Tsunami - Wave Propagation, Theory, Numerical Approach and Data Inversion*, Keio Univ.

Honda R., S. Aoi, N. Morikawa, H. Sekiguchi, T. Kunugi and H. Fujiwara (2004), Ground motion and rupture process of the 2003 Tokachi-oki earthquake obtained by strong-motion data of K-NET and KiK-net, *Earth Earth Planets Space*, 56, 317–322

Horikawa H. (2004), Fault geometry and slip distribution of the 2003 Tokachi-oki earthquake as deduced from teleseismic body waves, *Earth Planets Space 56*, 1011–1017.

GSI, *Geodetic Survey Institute*, Government of Japan, http://mekira.gsi.go.jp/ENGLISH/index.html.

Ichinose G., P. Somerville, H.K. Thio, R. Graves, and D. O'Connell (2007), Rupture process of the 1964 Prince William Sound, Alaska, earthquake from the combined inversion of seismic, tsunami, and geodetic data, *J. Geophys. Res., 112*, B07306, doi:10.1029/2006JB004728.

Ito Y., H. Matsubayashi, H. Kimura, T. Matsumoto, Y. Asano, and S. Sekiguchi (2004), Spatial distribution for moment tensor solutions of the 2003 Tokachi-oki earthquake (M_{JMA} = 8.0) and aftershocks, *Earth Planets Space 56*, 301-306.

JAMSTEC, *Japan Agency for Marine-earth Science and Technology*, http://www.jamstec.go.jp/scdc/top_e.html.

Ji C., Wald D.J., and D.V. Helmberger (2002), Source description of the 1999 Hector Mine, California earthquake; Part I: wavelet domain inversion theory and resolution analysis, *Bull. Seismol. Soc. Am., 92*, 4, 1192-1207,doi:10.1785/0120000916.

Katsumata K., N. Wada, and M. Kasahara (2003), Newly imaged shape of the deep seismic zone within the subducting Pacific plate beneath the Hokkaido corner, Japan-Kurile arc-arc junction, *J. Geophys. Res. 108*, doi:10.1029/2002JB002175.

Koketsu K., K. Hikima, S. Miyazaki, and S. Ide (2004), Joint inversion of strong motion and geodetic data for the source process of the 2003 Tokachi-oki, Hokkaido, earthquake, *Earth Planets Space, 56*, 329 – 334.

Lorito S., F. Romano, A. Piatanesi, and E. Boschi (2008a), Source process of the September 12, 2007, Mw 8.4 southern Sumatra earthquake from tsunami tide gauge record inversion, *Geophys. Res. Lett., 35*, L02310, doi:10.1029/2007GL032661.

Lorito S., A. Piatanesi, and A. Lomax (2008b), Rupture Process of the 18 April 1906 California Earthquake from Near-Field Tsunami Waveform Inversion*, Bull. Seismol. Soc. Am., 98*(2), 832–845, doi: 10.1785/0120060412.

Mader C. L. (2001), *Numerical Modeling of Water Waves*, Los Alamos Ser. 341 Basic Appl. Sci., vol. 8, CRC Press, Boca Raton, Fla.

Mikada H., K. Mitsuzawa, H. Sugioka, T. Baba, K. Hirata, H. Matsumoto, S. Morita, R. Otsuka, T. Watanabe, E. Araki, and K. Suyehiro (2006), New discoveries in dynamics of an M8 earthquake-Phenomena and their implications at the 2003 Tokachi Earthquake using a long term monitoring cabled observatory, *Tectonophysics*, 426, 95 – 105, doi:10.1016/j.tecto.2006.02.021.

Nakanishi, A., A. J. Smith, S. Miura, T. Tsuru, S. Kodaira, K. Obana, N. Takahashi, P. R. Cummins, and Y. Kaneda (2004), Structural factors controlling the coseismic rupture zone of the 1973 Nemuro-Oki earthquake, the southern Kuril Trench seismogenic zone, *J. Geophys. Res.*, 109, B05305, doi:10.1029/2003JB002574.

Nishimura S., M. Ando, and K. Tadokoro (2005), An application of numerical simulation techniques to improve the resolution of offshore fault kinematics using seafloor geodetic methods, *Physics of the Earth and Planetary Interiors 151,* 181–193, doi:10.1016/j.pepi.2005.03.002.

Okada, Y. (1992), Internal deformation due to shear and tensile faults in a half-space, Bull. Seismol. Soc. Am., 82, 1018-1040. 208.

Piatanesi, A., A. Cirella, P. Spudich and M. Cocco (2007) : A global search inversion for earthquake kinematic rupture history : application to the 2000 Western Tottori, Japan earthquake *J. Geophys. Res.* Vol. 112, No. B7, B07314, doi:10.1029/2006JB004821.

Piatanesi A., and S. Lorito (2007), Rupture Process of the 2004 Sumatra–Andaman Earthquake from Tsunami Waveform Inversion, *Bull. Seismol. Soc. Am., 97*(1A), S223-S231, doi: 10.1785/0120050627.

Rothman D. (1986), Automatic estimation of large residual statics corrections, *Geophysics, 51*, 332-346.

Satake K. (1993), Depth Distribution of Coseismic Slip Along the Nankai Trough, Japan, From Joint Inversion of Geodetic and Tsunami Data, *J. Geophys. Res., 98*, B3, 4553-4565.

Sawai Y., T. Kamataki, M. Shishikura, H. Nasu, Y. Okamura, K. Satake, K. H. Thomson, D. Matsumoto, Y. Fujii, J. Komatsubara, and T. T. Aung (2009), Aperiodic recurrence of geologically recorded tsunamis during the past 5500 years in Weastern Hokkaido, Japan, *J. Geophys. Res.,* 114, B01319, doi:10.1029/2007JB005503.

Sen M., and P.L. Stoffa (1991), Nonlinear one-dimensional seismic waveform inversion using simulated annealing, *Geophysics*, *56*, 1624-1638.

Spudich P., and D.P. Miller (1990), Seismic site effects and the spatial interpolation of earthquake seismograms: results using aftershocks of the 1986 North Palm Springs, California earthquake, *Bull. Seismol. Soc. Am., 80*, 1504-1532.

Tanioka Y., K. Hirata, R. Hino, and T. Kanazawa (2004a), Slip distribution of the 2003 Tokachi-oki earthquake estimated from tsunami waveform inversion, *Earth Planets Space 56*, 373 – 376.

Tanioka Y. et al. (2004b), Tsunami run-up heights of the 2003 Tokachi-oki earthquake, *Earth Planets Space 56,* 359-365.

Wald D. J., and R. W. Graves (2001), Resolution analysis of finite fault source inversion using one- and three-dimensional Green's functions 2. Combining seismic and geodetic data, *J. Geophys. Res., 106*, 8767–8788.

Wang Z., and D. Zhao (2005), Seismic imaging of the entire arc of Tohoku and Hokkaido in Japan using P-wave, S-wave and sP depth-phase data*, Physics of the Earth and Planetary Interiors 152*, 144-162, doi:10.1016/j.pepi.2005.06.010.

Wang R., F.L. Martin, and F. Roth (2006), PSGRN/PSCMP - a new code for calculating co- and post-seismic deformation, geoid and gravity changes based on the viscoelastic-gravitational dislocation theory. *Computers and Geosciences, 32*, 527-541, doi:10.1016/j.cageo. 2005.08.006.

Watanabe T., H. Takahashi, M. Ichiyanagi, M. Okayama, M. Takada, R. Otsuka, K. Hirata, S. Morita, M. Kasahara, and H. Mikada (2006), Seismological monitoring on the 2003 Tokachi-oki earthquake, derived from off Kushiro permanent cabled OBSs and land-based observations, *Tectonophysics, 426*, 107-118, doi:10.1016/j.tecto.2006.02.016.

Yagi Y. (2004), Source rupture process of the 2003 Tokachi-oki earthquake determined by joint inversion of teleseismic body wave and strong ground motion data*, Earth Planets Space, Vol 56*, 311-316.

Yamanaka Y., and M. Kikuchi (2003), Source process of the recurrent Tokachi-oki earthquake on September 26, 2003, inferred from teleseismic body waves*, Earth Planets Space, 55*, e21–e24.

Yamanaka H., K. Motoki, K. Etoh, M. Murayama, and N. Komaba (2004), Observation of aftershocks of the 2003 Tokachi-Oki earthquake for estimation of local site effects, *Earth Planets Space, 56*, 335-340.

Zhao S., R.D. Müller, Y. Takahashi, and Y. Kaneda (2004), 3-D finite-element modeling of deformation and stress associated with faulting: effect of inhomogeneous crustal structures, *Geophys. J. Int., 157*, 629-644, doi:10.1111/j.1365-246X.2004.02200.x.

Tables

Table 1. Tide-gages positions

Station	Lon	Lat	Sampling (min)
Hanasaki	145.57 E	43.28 N	1
Kirittapu	145.12 E	43.08 N	1
AkkNshi	144.85 E	43.05 N	1
Kushiro	144.37 E	42.97 N	1
Tokachikou	143.32 E	42.30 N	1
Urakawa	142.77 E	42.16 N	1
Tomakomai	141.82 E	42.61 N	1
Muroran	140.95 E	42.34 N	1
Morikou	140.59 E	42.11 N	1
Hakodate	140.72 E	41.78 N	1
Sekinehama	141.24 E	41.36 N	1
Hachinohe	141.53 E	40.53 N	1
Miyako	141.97 E	39.64 N	1
Kamaishi	141.89 E	39.27 N	1
Ofunato	141.75 E	39.02 N	1
Ayukawa	141.51 E	38.30 N	1

Table 2. Geodetic coseismic dataset

Lon	**Lat**	**E_{offset}**	**N_{offset}**	**Z_{offset}**	**E_{sig}**	**N_{sig}**	**Z_{sig}**
°E	°N	cm	cm	cm	cm	cm	cm
140,81	40,83	0,658	-0,141	-1,862	0,239	0,342	0,732
141,84	43,53	9,409	-7,525	0,144	0,229	0,401	1,052
141,75	45,40	1,809	-2,262	0,046	0,382	0,345	1,100
143,22	44,43	2,698	-5,454	0,162	0,412	0,335	1,210
141,76	44,40	3,796	-4,252	0,404	0,241	0,315	1,319
144,68	43,92	1,817	-0,579	-0,385	0,360	0,356	1,364
144,45	43,51	3,908	-2,474	-1,980	0,394	0,386	0,962
145,51	43,29	5,683	4,564	-1,590	0,285	0,390	0,661
142,48	43,59	11,035	13,493	0,604	0,384	0,478	1,759
141,51	43,85	6,312	-5,131	-1,050	0,235	0,288	0,962
145,13	43,07	11,383	9,359	0,996	0,201	0,513	0,803
144,43	42,96	15,868	7,573	0,879	0,209	0,497	0,416
143,46	43,03	23,773	-33,633	-9,328	0,525	0,434	0,680
142,40	42,98	25,988	-21,846	-4,731	0,348	0,284	0,693
141,03	43,18	7,396	-3,857	-0,553	0,211	0,383	0,787
141,73	42,98	13,275	-7,273	-0,334	0,215	0,313	0,893
143,33	42,32	77,143	-50,272	-23,745	2,510	0,756	1,464
142,36	42,36	32,722	-11,746	-8,909	0,555	0,345	0,761
139,86	42,45	2,950	-0,756	-0,736	0,166	0,397	0,511
140,94	42,37	6,249	-1,382	-1,389	0,211	0,366	0,565
143,16	42,01	61,116	-15,742	-18,843	1,748	0,361	0,687
139,52	42,15	2,015	-0,331	-0,943	0,266	0,378	0,741
140,11	42,01	2,624	-0,351	-1,064	0,211	0,387	0,760
140,75	41,83	3,370	-0,408	-1,732	0,243	0,429	0,500
140,04	41,47	1,359	-0,220	-1,871	0,256	0,445	1,058
141,21	41,30	1,869	-0,086	-2,221	0,233	0,408	1,126
140,27	40,78	0,599	-0,136	-1,122	0,242	0,368	0,831

142,17	45,34	1,757	-2,551	-0,401	0,360	0,337	1,034
141,04	45,28	1,907	-2,088	-0,800	0,334	0,351	1,188
142,54	45,00	2,017	-3,084	-0,375	0,294	0,245	0,832
141,74	44,89	2,572	-2,998	-0,653	0,304	0,331	1,115
142,27	44,73	2,591	-4,013	-0,183	0,295	0,348	1,174
141,33	44,43	3,685	-3,438	-0,061	0,275	0,346	1,037
142,63	44,29	3,986	-6,501	0,602	0,346	0,334	1,292
144,03	44,06	2,086	-4,926	-0,239	0,403	0,283	1,002
145,19	44,02	2,014	1,192	-0,958	0,373	0,331	1,323
142,15	44,01	6,079	-7,381	1,080	0,252	0,280	1,305
143,33	44,01	4,042	-8,628	0,169	0,379	0,311	1,235
143,93	42,89	23,316	-16,498	-4,525	0,669	0,421	0,803
144,99	43,55	3,907	2,532	-0,809	0,356	0,398	0,845
143,79	43,85	3,310	-7,953	-0,733	0,378	0,359	1,267
145,13	43,66	3,434	2,073	-1,015	0,415	0,379	0,794
144,77	43,41	4,715	2,476	-1,492	0,364	0,414	0,677
141,43	43,40	8,427	-5,400	-0,649	0,198	0,364	0,820
145,12	43,38	5,588	4,849	-0,795	0,265	0,413	0,509
145,80	43,37	4,350	3,290	-1,385	0,347	0,362	0,604
140,60	43,29	5,659	-2,746	-0,730	0,283	0,339	0,917
143,56	43,29	13,713	-21,693	-4,366	1,389	0,381	0,540
144,33	43,23	7,534	-3,546	-1,450	0,327	0,438	1,371
143,30	43,23	17,145	-26,173	-5,070	0,567	0,358	0,733
144,13	43,12	11,549	-9,136	-2,313	0,409	0,413	1,780
144,84	43,06	12,442	10,765	1,850	0,258	0,540	0,744
140,50	43,06	5,421	-2,244	-0,713	0,277	0,363	0,714
140,54	42,99	5,581	-2,252	-0,850	0,285	0,429	0,770
141,29	42,97	9,085	-4,540	-0,289	0,231	0,355	1,003
140,88	42,86	6,948	-2,756	-1,274	0,248	0,346	0,556
140,60	42,80	5,755	-1,955	-1,390	0,297	0,361	0,620
140,23	42,79	4,239	-1,324	-1,380	0,282	0,386	0,622
141,86	42,73	16,658	-8,001	-1,828	0,191	0,318	0,686
142,30	42,73	29,419	-19,027	-5,479	0,292	0,520	0,789
143,10	42,70	48,976	-46,362	-19,237	1,099	0,788	1,405
141,08	42,67	7,813	-2,977	-0,791	0,285	0,389	0,709
141,60	42,66	12,223	-5,057	-0,111	0,208	0,315	0,935
140,83	42,65	6,366	-2,038	-1,345	0,222	0,404	0,508
143,46	42,55	57,192	-46,367	-16,101	1,105	0,816	1,043
141,36	42,55	9,497	-3,022	-1,164	0,219	0,426	0,694
140,35	42,49	3,933	-1,046	-1,357	0,219	0,389	0,208
142,06	42,48	21,376	-8,503	-3,574	0,220	0,383	1,238
142,57	42,25	40,842	-12,523	-12,589	0,990	0,405	0,914
140,25	42,24	3,366	-0,702	-1,072	0,222	0,396	0,534
142,94	42,13	59,703	-16,044	-21,304	1,265	0,465	0,717
140,00	42,13	2,746	-0,646	-1,123	0,231	0,423	0,523
140,57	42,10	3,691	-0,710	-1,112	0,179	0,401	0,647
140,81	42,04	4,303	-0,632	-1,194	0,235	0,455	0,682
141,14	41,83	4,223	-0,241	-2,168	0,223	0,495	0,557
140,32	41,60	2,015	-0,273	-1,396	0,294	0,472	0,629
140,88	41,46	2,052	0,087	-2,097	0,256	0,407	0,806
140,64	41,04	0,990	-0,093	-2,280	0,291	0,367	0,509
141,37	40,97	0,917	-0,010	-3,012	0,255	0,350	0,837
141,20	40,63	0,485	-0,260	-2,611	0,249	0,324	0,682
139,93	40,58	0,123	-0,104	-1,205	0,197	0,379	0,777
141,17	45,14	2,227	-2,200	-0,418	0,268	0,354	1,169
142,96	44,58	2,780	-4,962	0,118	0,421	0,405	1,184
143,62	44,22	2,589	-5,799	-0,290	0,419	0,288	1,139
143,08	44,19	3,751	-7,068	0,886	0,380	0,305	1,117

144,29	43,99	1,754	-3,309	-0,728	0,347	0,302	0,933
142,58	43,91	6,594	-9,507	1,018	0,249	0,341	1,522
144,12	43,83	2,486	-5,456	-0,408	0,387	0,330	1,060
142,41	43,74	8,826	-10,737	0,290	0,343	0,337	1,591
141,87	43,74	7,806	-7,147	-0,658	0,224	0,319	1,002
142,90	43,77	7,315	-11,542	0,627	0,296	0,503	1,461
143,58	43,67	5,155	-11,838	-0,821	0,278	0,439	1,589
145,26	43,23	7,235	6,258	-0,685	0,210	0,441	0,496
144,08	43,44	5,440	-8,337	-1,872	0,399	0,381	1,083
142,40	43,34	16,79	-16,996	-2,665	0,672	0,354	0,757
144,60	43,31	5,925	1,673	-0,949	0,312	0,401	0,712
141,89	43,25	12,95	-9,035	-0,467	0,212	0,365	1,188
140,86	43,21	6,672	-3,279	-0,754	0,300	0,380	0,594
142,81	43,17	21,366	-26,655	-6,232	0,265	0,314	0,919
145,52	43,2	5,942	5,197	-0,890	0,271	0,400	0,558
141,54	43,08	10,714	-6,009	-0,148	0,203	0,349	1,137
143,17	42,94	30,490	-38,930	-10,666	1,035	0,669	0,901
141,58	42,88	11,700	-5,765	-0,915	0,196	0,343	0,921
141,41	42,77	10,082	-4,299	-1,139	0,276	0,355	0,796
140,90	42,56	6,673	-1,926	-1,483	0,224	0,387	0,574
140,77	42,55	5,674	-1,610	-0,698	0,191	0,418	0,427
140,88	42,47	6,103	-1,558	-1,572	0,212	0,385	0,815
139,45	42,06	2,019	-0,500	-1,394	0,225	0,435	0,380
140,67	42,12	4,290	-0,657	-1,139	0,187	0,471	0,519
140,72	41,98	3,752	-0,427	-1,462	0,240	0,433	0,889
140,07	41,80	2,147	-0,169	-1,341	0,227	0,434	0,785
144,72	42,98	15,285	12,599	4,512	0,231	0,520	0,644
143,32	42,13	83,160	-38,260	-22,537	2,638	0,502	0,766
141,45	41,40	2,522	-0,272	-1,963	0,193	0,422	0,902
140,49	41,19	1,002	-0,068	-2,248	0,225	0,358	0,856
140,82	41,15	1,364	0,035	-2,177	0,207	0,443	0,540
140,87	40,91	0,835	-0,082	-1,781	0,171	0,392	0,572
141,13	40,86	0,645	-0,125	-2,522	0,223	0,349	0,954
140,59	40,71	0,525	-0,225	-2,046	0,265	0,372	0,880
141,38	40,68	0,379	-0,252	-2,017	0,226	0,336	0,905
140,48	40,62	0,452	-0,271	-2,010	0,212	0,376	0,786
140,80	40,64	0,414	-0,096	-2,609	0,192	0,348	0,832
140,45	40,91	0,693	-0,276	-1,288	0,225	0,370	0,734
141,60	45,22	2,123	-2,456	-0,540	0,328	0,335	1,199
142,35	45,13	1,932	-2,844	-0,056	0,349	0,315	1,211
142,72	44,78	2,310	-3,917	-0,395	0,284	0,298	1,104
141,79	44,64	2,180	-2,687	0,127	0,241	0,287	0,956
142,26	44,37	3,942	-5,385	0,015	0,230	0,357	1,189
141,66	44,15	4,834	-4,818	-0,280	0,185	0,317	1,232
144,51	43,72	2,406	-1,874	-0,906	0,341	0,370	1,410
141,37	43,62	7,224	-5,040	-0,675	0,265	0,338	0,844
142,95	43,33	16,286	-23,295	-4,236	0,640	0,368	0,909
142,64	43,43	14,859	-17,732	-1,591	0,231	0,676	2,108
143,90	43,10	15,143	-18,055	-5,71	1,128	0,536	0,937
142,87	43,01	27,680	-32,068	-6,76	0,524	0,321	1,048
142,08	42,93	19,862	-12,716	-2,089	0,183	0,333	1,059
143,50	42,81	34,423	-41,239	-13,528	1,008	0,688	1,390
141,08	42,42	6,849	-1,577	-1,570	0,230	0,466	0,431
143,15	42,49	65,900	-46,415	-28,646	1,253	0,653	1,325
140,37	41,93	2,888	-0,357	-0,795	0,229	0,438	0,612
144,44 (*)	41,70 (*)			0,370			0,050
144,85 (*)	42,24 (*)			0,120			0,060

(*) Longitude and latitude refer to ocean bottom pressure gages PG1 and PG2

Table 3. Layered Crustal Model

Depth (km)	Vp (m/s)	Vs (m/s)	Density (kg/m^3)	Rigidity (N/m^2)
0-20	6251	3565	2830	$3.6 \cdot 10^{10}$
20-40	7313	4141	2925	$5.0 \cdot 10^{10}$
40-100	7840	4407	3076	$6.0 \cdot 10^{10}$
100-∞	8109	4538	3247	$6.7 \cdot 10^{10}$

Table 4. Subfaults.

Fault segment	LONG.(*) E	LAT.(*) N	W (km)	L (km)	Strike (deg)	Rake (deg)	Dip (deg)	Top (km)
1	144.48	43.11	30	30	225	109	24.6	42.2
2	144.72	42.93	30	30	225	109	21.4	31.3
3	144.98	42.75	30	30	225	109	13.6	24.2
4	145.23	42.56	30	30	225	109	12.0	18.0
5	145.48	42.38	30	30	225	109	12.0	11.7
6	144.23	42.92	30	30	225	109	24.6	42.2
7	144.47	42.74	30	30	225	109	21.4	31.3
8	144.72	42.56	30	30	225	109	13.6	24.2
9	144.98	42.37	30	30	225	109	12.0	18.0
10	145.23	42.19	30	30	225	109	12.0	11.7
11	143.98	42.73	30	30	225	109	24.6	42.2
12	144.22	42.55	30	30	225	109	21.4	31.3
13	144.47	42.37	30	30	225	109	13.6	24.2
14	144.72	42.18	30	30	225	109	12.0	18.0
15	144.97	41.99	30	30	225	109	12.0	11.7
16	143.73	42.54	30	30	225	109	24.6	42.2
17	143.97	42.36	30	30	225	109	21.4	31.3
18	144.22	42.18	30	30	225	109	13.6	24.2
19	144.47	41.99	30	30	225	109	12.0	18.0
20	144.72	41.80	30	30	225	109	12.0	11.7
21	143.48	42.35	30	30	225	109	24.6	42.2
22	143.72	42.17	30	30	225	109	21.4	31.3
23	143.98	41.99	30	30	225	109	13.6	24.2
24	144.22	41.80	30	30	225	109	12.0	18.0
25	144.47	41.61	30	30	225	109	12.0	11.7
26	143.23	42.16	30	30	225	109	24.6	42.2
27	143.47	41.98	30	30	225	109	21.4	31.3
28	143.72	41.80	30	30	225	109	13.6	24.2
29	143.97	41.61	30	30	225	109	12.0	18.0
30	144.22	41.42	30	30	225	109	12.0	11.7

(*) Longitude and latitude refer to upper reference point (start point in strike direction) of each subfault.

Table 5. Best model parameters values for the checkerboard tests. Target values are in brackets.

Subfault	T.G. Slip (m)	GEODETIC Slip (m)	GEODETIC Bigger patches Slip (m)	GEODETIC Inland patches Slip (m)	JOINT Slip (m)
1	**3.5***(3)*	**3.0***(3)*	**3.0***(3)*	**3.0***(3)*	**3.0***(3)*
2	**1.0***(1)*	**1.0***(1)*	**3.0***(3)*	**1.0***(1)*	**1.0***(1)*
3	**3.0***(3)*	**3.0***(3)*	**1.0***(1)*	**3.0***(3)*	**3.0***(3)*
4	**1.0***(1)*	**1.5***(1)*	**1.0***(1)*	**1.0***(1)*	**1.0***(1)*
5	**3.0***(3)*	**2.5***(3)*	**3.0***(3)*	**3.0***(3)*	**3.0***(3)*
6	**0.5***(1)*	**1.0***(1)*	**3.0***(3)*	**1.0***(1)*	**1.0***(1)*
7	**3.0***(3)*	**3.0***(3)*	**3.0***(3)*	**3.0***(3)*	**3.0***(3)*
8	**1.0***(1)*	**1.0***(1)*	**1.0***(1)*	**1.0***(1)*	**1.0***(1)*
9	**3.0***(3)*	**2.0***(3)*	**1.0***(1)*	**3.0***(3)*	**3.0***(3)*
10	**1.0***(1)*	**0.5***(1)*	**3.0***(3)*	**1.0***(1)*	**1.0***(1)*
11	**3.5***(3)*	**3.0***(3)*	**1.0***(1)*	**3.0***(3)*	**3.0***(3)*
12	**1.0***(1)*	**1.0***(1)*	**1.0***(1)*	**1.0***(1)*	**1.0***(1)*
13	**3.5***(3)*	**2.5***(3)*	**3.0***(3)*	**3.0***(3)*	**3.0***(3)*
14	**1.0***(1)*	**3.0***(1)*	**3.0***(3)*	**1.0***(1)*	**1.0***(1)*
15	**3.0***(3)*	**2.5***(3)*	**1.0***(1)*	**3.0***(3)*	**3.0***(3)*
16	**0.5***(1)*	**1.0***(1)*	**1.0***(1)*	**1.0***(1)*	**1.0***(1)*
17	**3.5***(3)*	**2.5***(3)*	**1.0***(1)*	**3.0***(3)*	**3.0***(3)*
18	**0.5***(1)*	**1.5***(1)*	**3.0***(3)*	**1.0***(1)*	**1.0***(1)*
19	**3.0***(3)*	**2.0***(3)*	**3.0***(3)*	**3.0***(3)*	**3.0***(3)*
20	**1.0***(1)*	**4.0***(1)*	**1.0***(1)*	**1.0***(1)*	**1.0***(1)*
21	**4.0***(3)*	**3.0***(3)*	**3.0***(3)*	**3.0***(3)*	**3.0***(3)*
22	**0.5***(1)*	**1.5***(1)*	**3.0***(3)*	**1.0***(1)*	**1.0***(1)*
23	**3.5***(3)*	**2.5***(3)*	**1.0***(1)*	**3.0***(3)*	**3.0***(3)*
24	**1.0***(1)*	**2.5***(1)*	**1.0***(1)*	**1.0***(1)*	**1.0***(1)*
25	**3.0***(3)*	**0.0***(3)*	**3.0***(3)*	**3.0***(3)*	**3.0***(3)*
26	**0.5***(1)*	**1.0***(1)*	**3.0***(3)*	**1.0***(1)*	**1.0***(1)*
27	**3.5***(3)*	**3.0***(3)*	**3.0***(3)*	**3.0***(3)*	**3.0***(3)*
28	**1.0***(1)*	**1.5***(1)*	**1.0***(1)*	**1.0***(1)*	**1.0***(1)*
29	**3.0***(3)*	**1.5***(3)*	**1.0***(1)*	**3.0***(3)*	**3.0***(3)*
30	**1.0***(1)*	**2.0***(1)*	**3.0***(3)*	**1.0***(1)*	**1.0***(1)*

Table 6. Best and average models for the 2003 Tokachi-Oki earthquake

Subfault	BEST TIDE_GAGE Slip (m)	BEST GEODETIC Slip (m)	BEST JOINT Slip (m)	AVERAGE JOINT Slip (m)
1	0	0	**0**	**0.2±0.5**
2	0	1	**1**	**0.7±0.6**
3	1	0	**0**	**0.2±0.5**
4	0	0	**0**	**0.2±0.6**
5	0	0	**0**	**0.6±1.1**
6	0	0	**0**	**0.2±0.6**
7	0	0	**0**	**0.4±0.8**
8	0	3	**3**	**1.7±1.2**
9	1	0	**0**	**0.7±1.2**
10	1	0	**1**	**1.2±1.6**
11	4	0	**0**	**0.8±1.1**
12	4	4	**4**	**3.2±1.8**
13	3	3	**2**	**2.8±1.9**
14	1	0	**1**	**1.4±1.6**
15	2	0	**1**	**1.8±1.7**
16	4	5	**5**	**3.0±1.7**
17	7	5	**7**	**5.6±2.6**
18	1	4	**1**	**2.5±2.2**
19	1	1	**2**	**1.7±1.5**
20	1	0	**1**	**1.4±1.7**
21	0	0	**0**	**0.9±1.0**
22	0	3	**1**	**2.3±1.9**
23	6	4	**7**	**6.0±2.1**
24	0	6	**0**	**0.9±1.5**
25	1	0	**1**	**1.3±1.6**
26	2	0	**0**	**0.4±0.8**
27	1	1	**2**	**1.3±1.1**
28	1	1	**1**	**1.0±1.2**
29	1	0	**1**	**1.3±1.2**
30	0	0	**0**	**0.8±1.6**

Figures

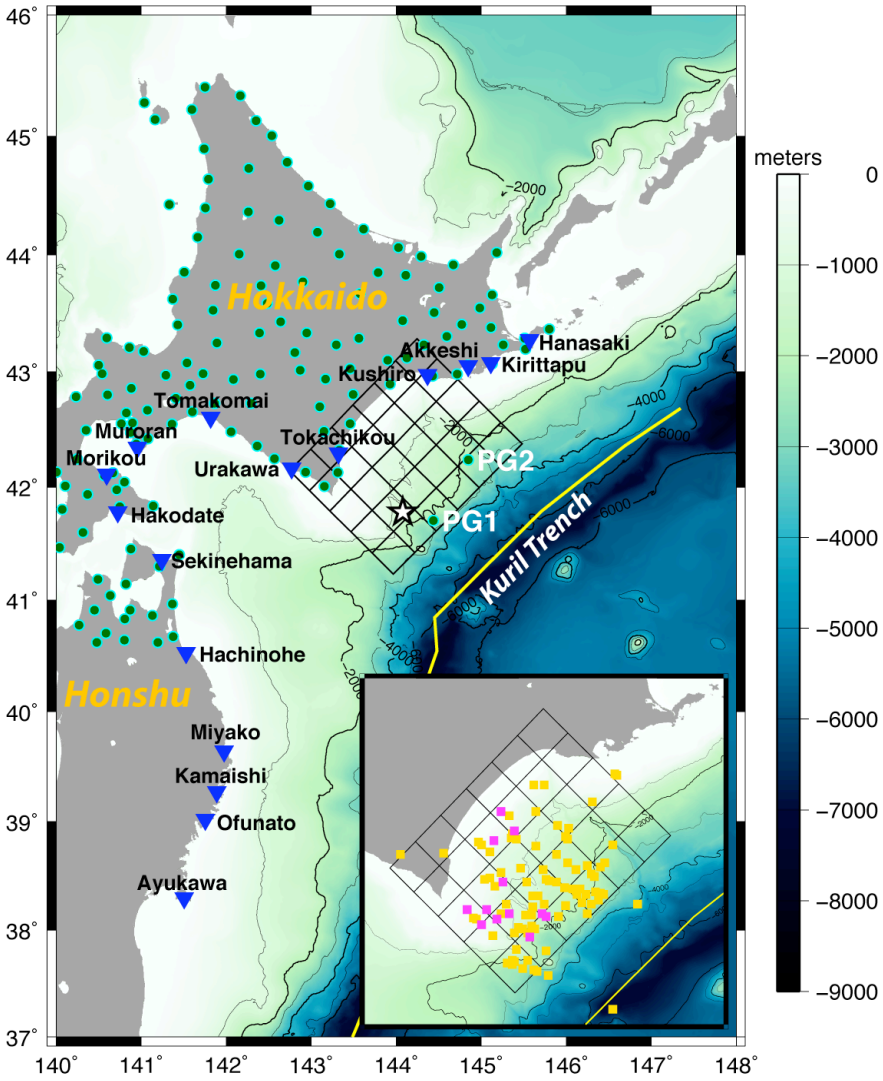

Figure 1. Map of the computational domain for the tsunami propagation. The star indicates the position of the Tokachi-Oki 2003 earthquake epicenter. Thin black lines are the surface projection of the boundaries of the subfaults used in this study. The red triangles are the tide-gauges stations used in the inversions (Tab. 1). The green dots are the GPS stations used in the inversion and the positions of the two ocean bottom pressure gages (PG1 and PG2) (Tab. 2). Into the inset the magenta squares indicate the earthquakes occurred before the major aftershock (M7.4); yellow squares indicate the aftershocks during the five days following the 2003 Tokachi-Oki event.

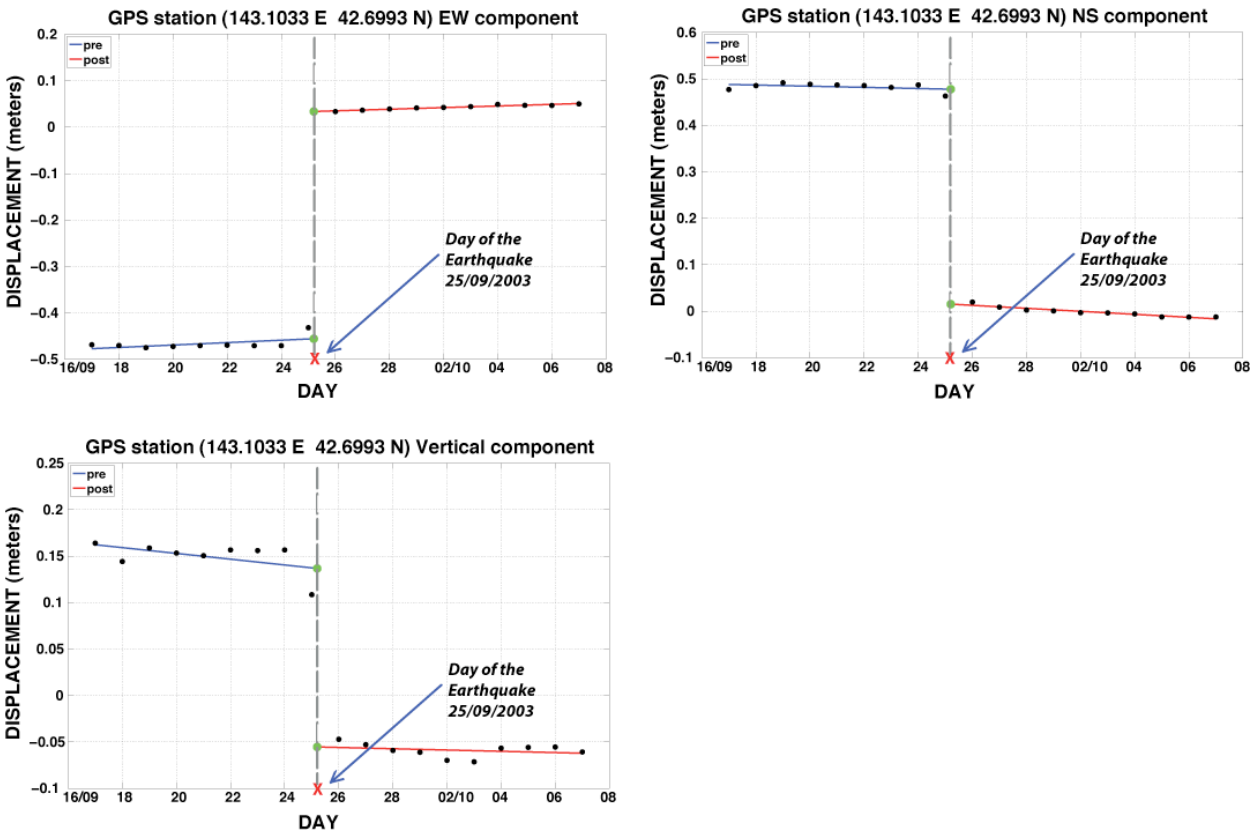

Figure 2. Observed GPS time series following the 25 September 2003 earthquake at continuous GPS site positioned at (144.1033E, 42.6993N). Eastward (top left panel), northward (top right panel), and vertical (bottom panel) displacements are shown. Superimposed in solid blue and red are the straight-line fits to 9-day portions of the preseismic and 10-day portions of the postseismic time series respectively. Red cross indicates the day of the Tokachi-Oki earthquake. The coseismic offsets and corresponding errors are reported in Tab. 2.

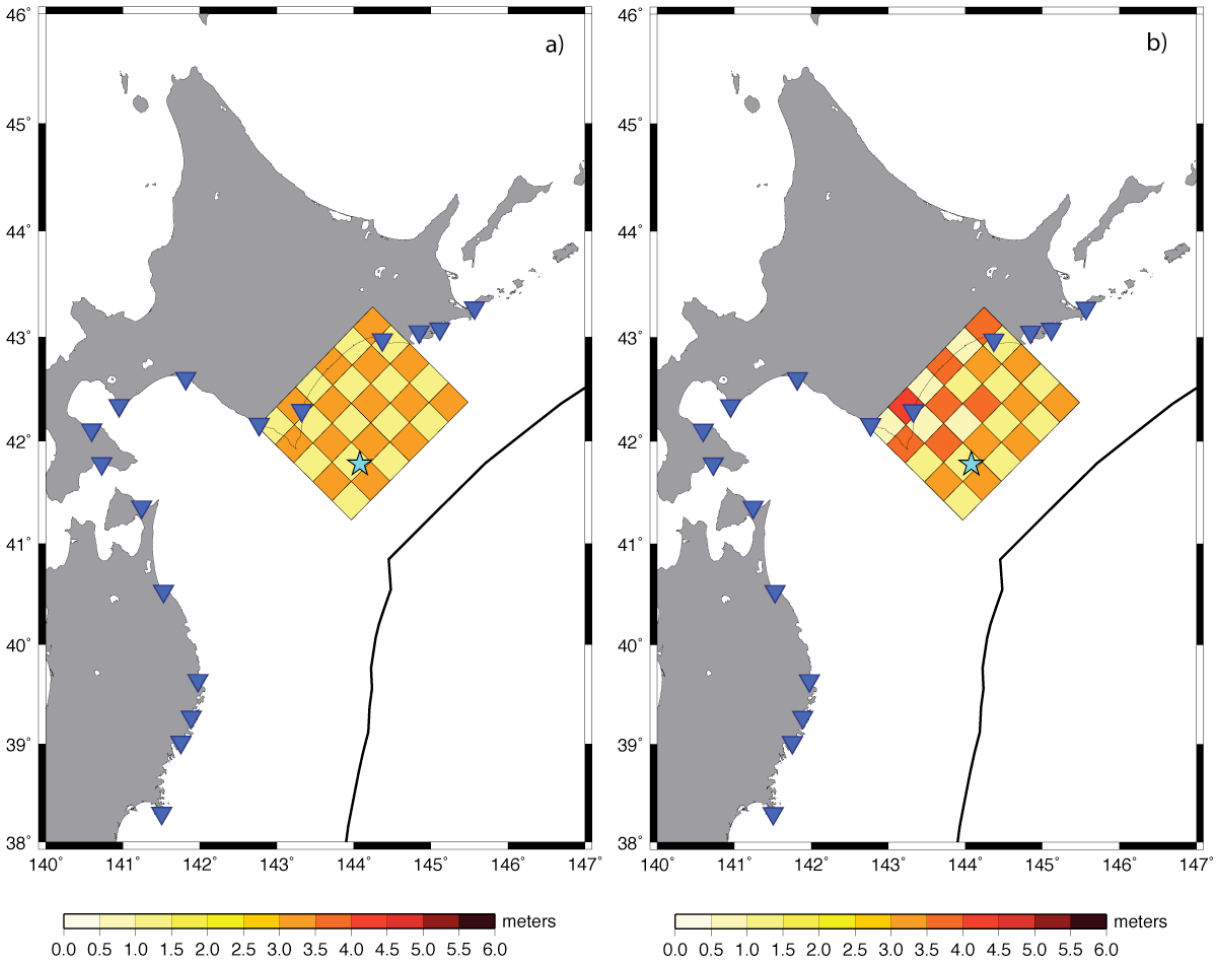

Figure 3. (a) Slip distribution of the target model. (b) Slip distribution obtained by the checkerboard test inverting only for the tsunami data. The star indicates the position of the Tokachi-Oki 2003 earthquake epicenter. The slip values are reported in Tab. 5.

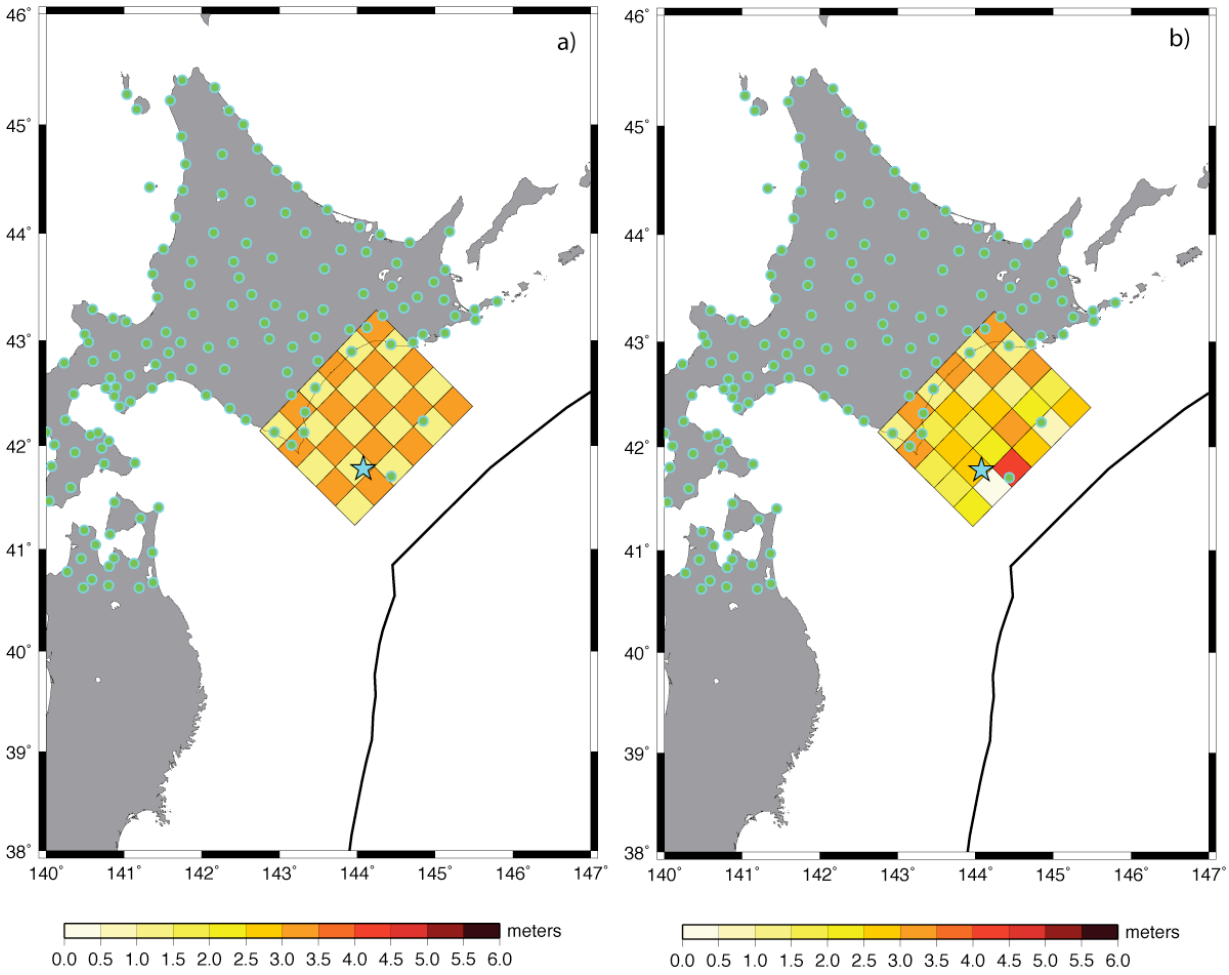

Figure 4. (a) The slip distribution of the target model. (b) Slip distribution obtained by the checkerboard test inverting only for the geodetic data. The star indicates the position of the Tokachi-Oki 2003 earthquake epicenter. The slip values are reported in Tab. 5.

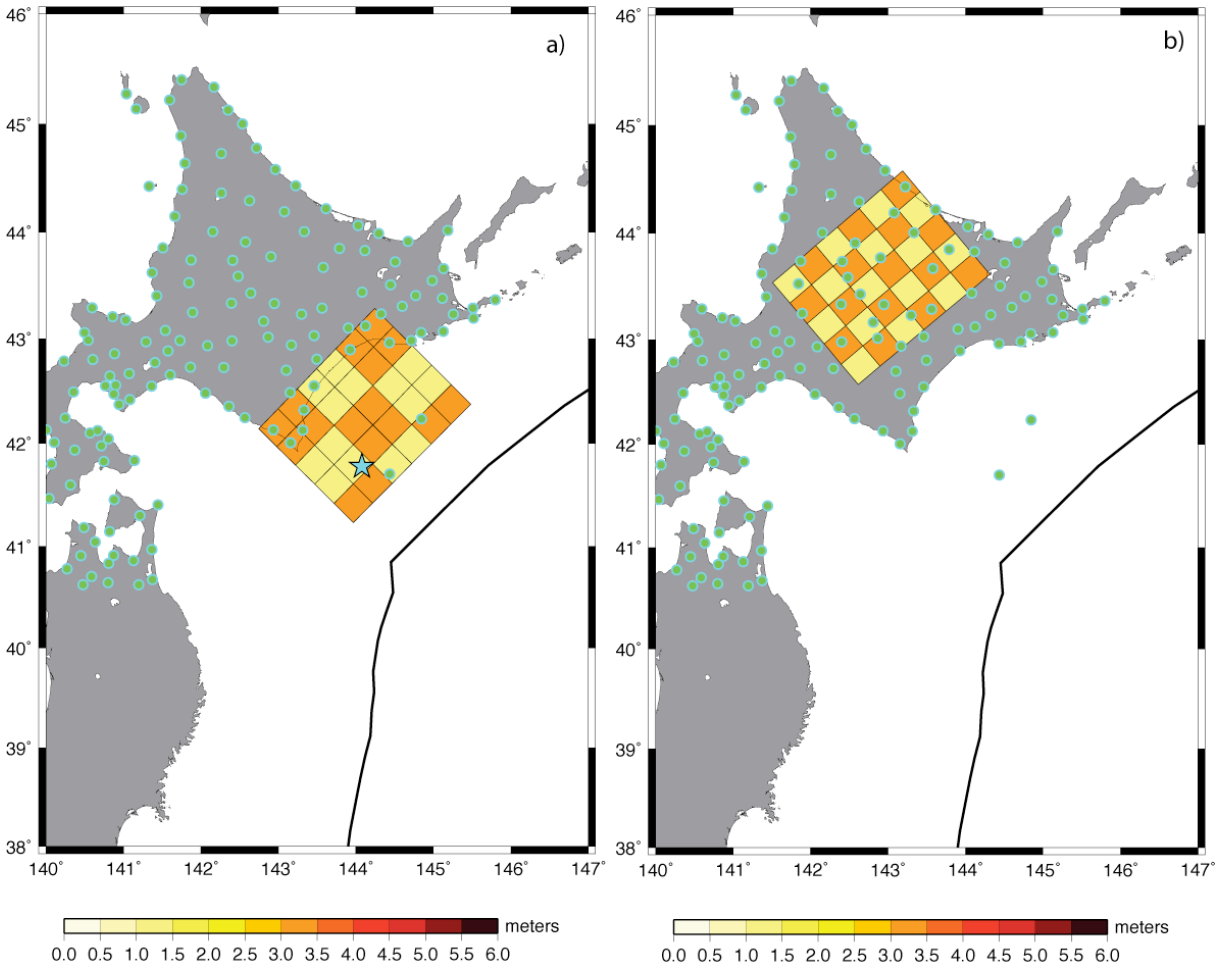

Figure 5. (a) Slip distribution obtained by the checkerboard test inverting only for the geodetic data and with subfaults of size 60x60 km. (b) The slip distribution obtained by the checkerboard test inverting only for the geodetic data and shifting the entire fault area beneath the Hokkaido region. The star indicates the position of the Tokachi-Oki 2003 earthquake epicenter. The slip values are reported in Tab. 5.

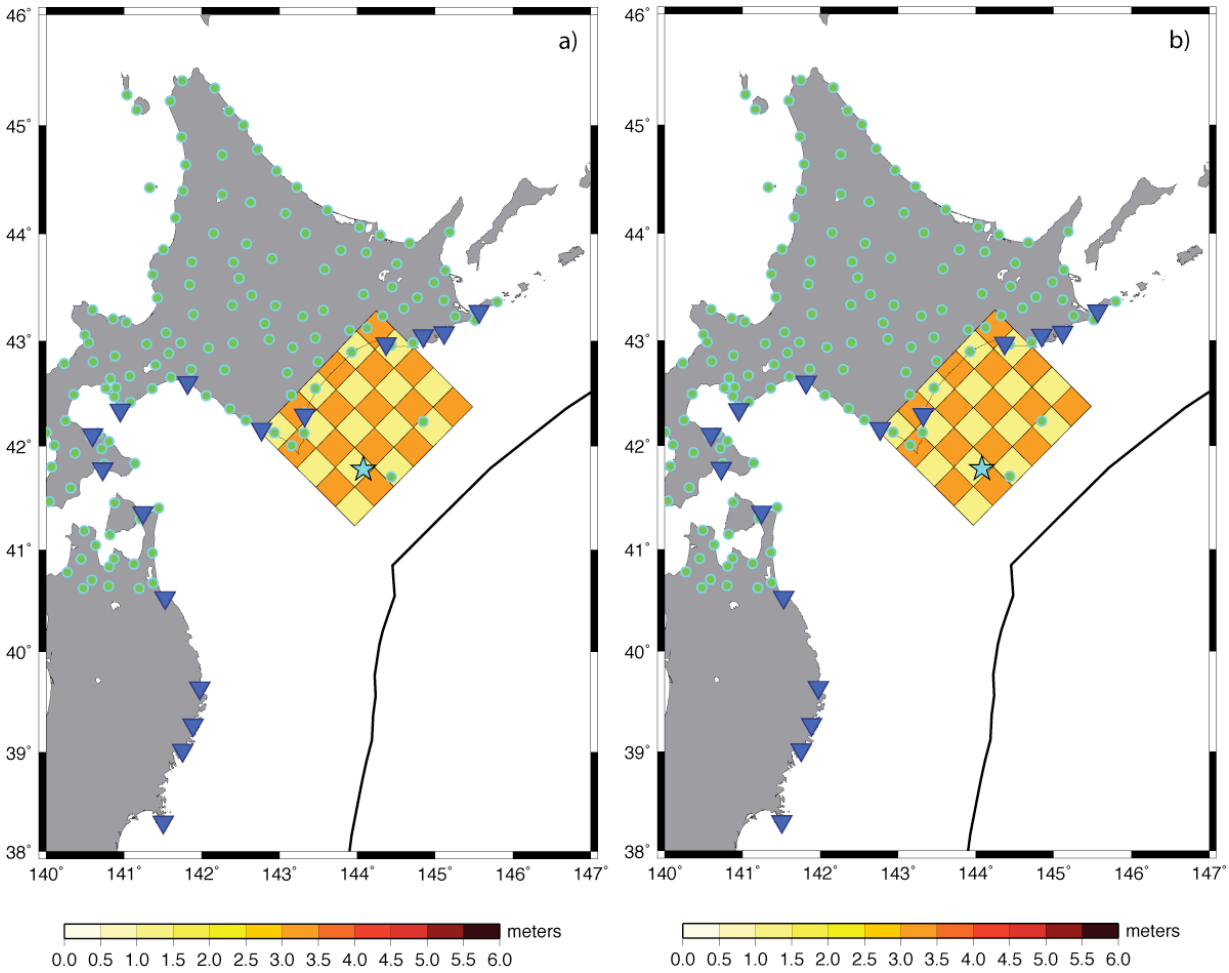

Figure 6. (a) Slip distribution of the target model. (b) Slip distribution obtained by the checkerboard test inverting jointly for the tsunami waveforms and the geodetic data. The star indicates the position of the Tokachi-Oki 2003 earthquake epicenter. The slip values are reported in Tab. 5.

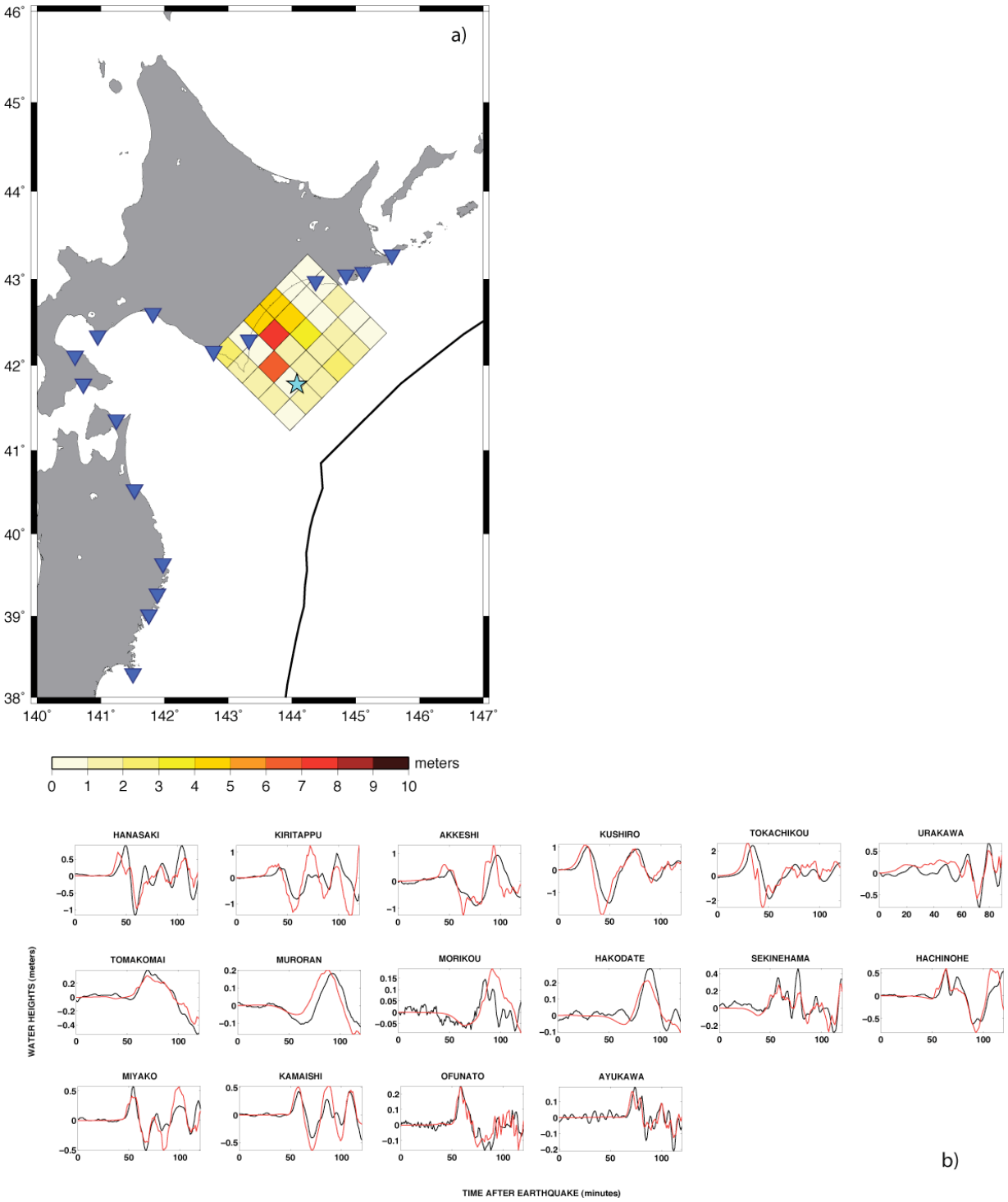

Figure 7. (a) Best model for the slip distribution obtained by inverting only for the tsunami data. (b) The comparison between the tsunami waveforms observed (black line) and inverted (red line) data. The star indicates the position of the Tokachi-Oki 2003 earthquake epicenter. The slip values are reported in Tab. 6.

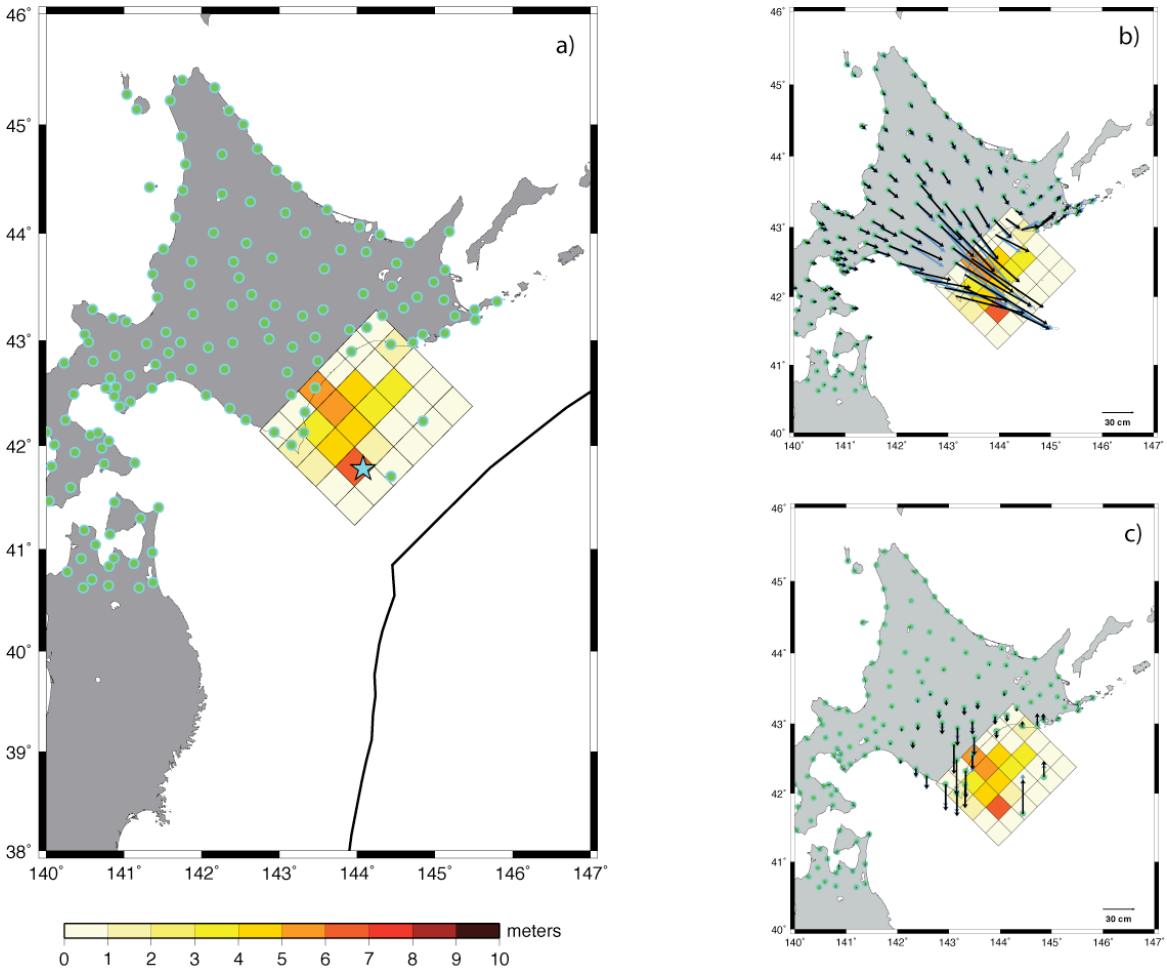

Figure 8. (a) Best model for the slip distribution obtained by inverting only for the geodetic data. (b,c) The comparison between the coseismic observed (cyan line) and inverted (black line) data. The star indicates the position of the Tokachi-Oki 2003 earthquake epicenter. The slip values are reported in Tab. 6.

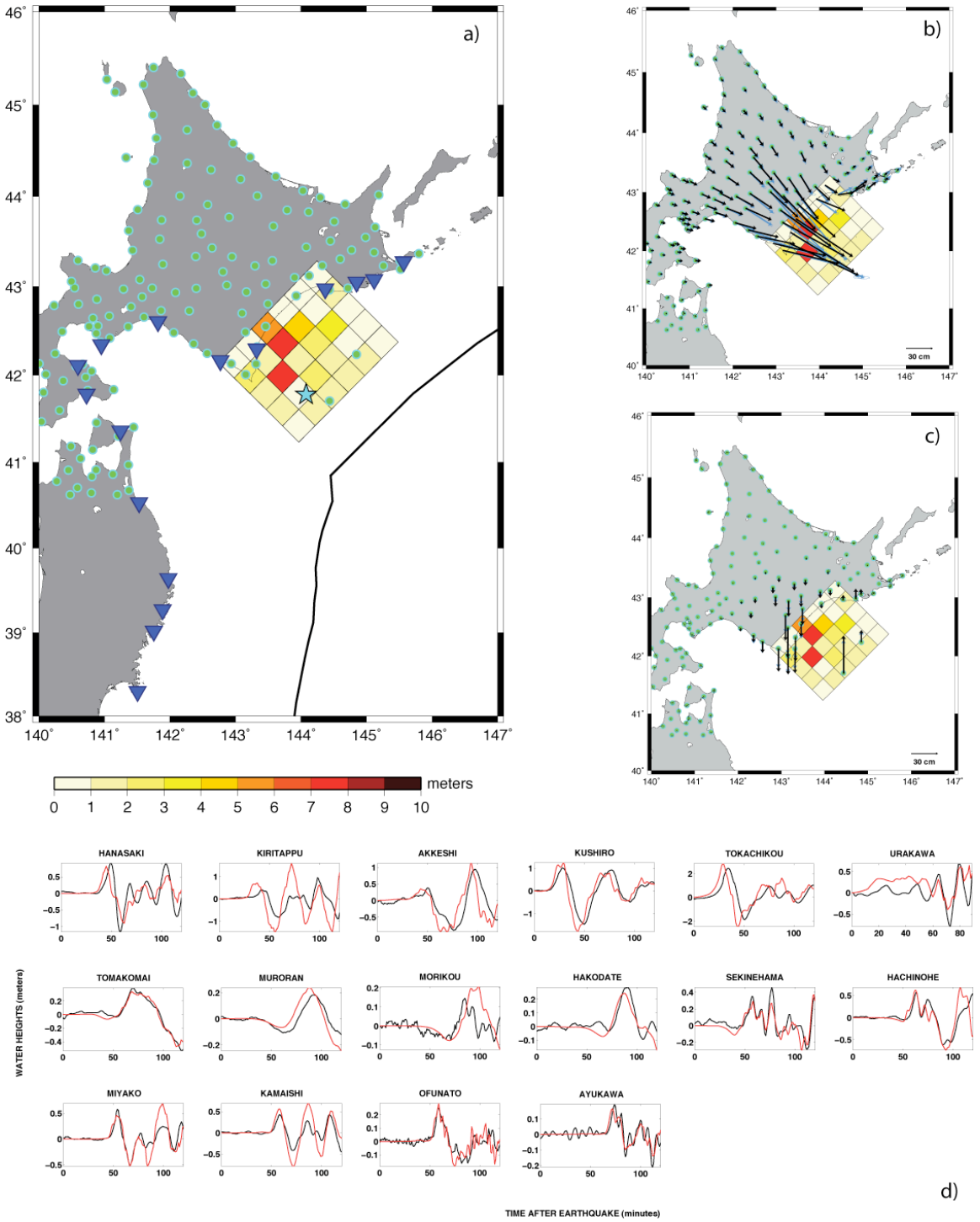

Figure 9. (a) Best model for the slip distribution obtained by inverting jointly for the tsunami waveforms and geodetic data. (b,c) The comparison between the coseismic displacements observed (cyan line) and inverted (black line) data. (d) The comparison between the tsunami waveforms observed (black line) and inverted (red line) data. The star indicates the position of the Tokachi-Oki 2003 earthquake epicenter. The slip values are reported in Tab. 6.

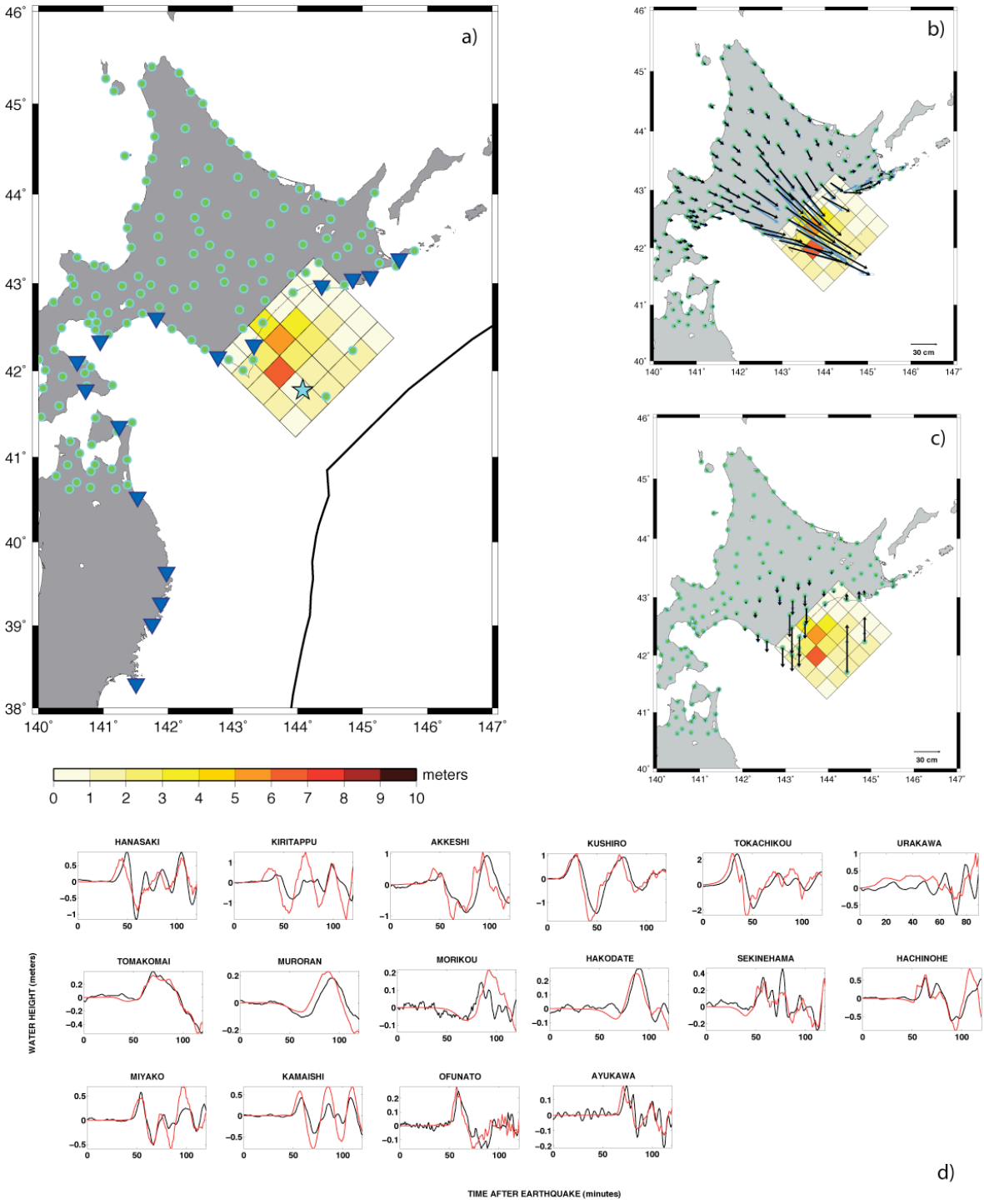

Figure 10. (a) Average model for the slip distribution obtained by inverting jointly for the tsunami waveforms and geodetic data. (b,c) The comparison between the coseismic displacements observed (cyan line) and inverted (black line) data. (d) The comparison between the tsunami waveforms observed (black line) and inverted (red line) data. The star indicates the position of the Tokachi-Oki 2003 earthquake epicenter. The slip values are reported in Tab. 6.

Chapter 5

Inverting for slip distribution and rupture velocity: the 2007 Sumatra earthquake

The 2007 Sumatra earthquake (Mw 8.4) generated a tsunami that resulted in 25 fatalities and 92 injured. In spite of event's magnitude the recorded tsunami wave was been very small. In this work the slip distribution is inferred by inverting several tsunami waveform. Furthermore, the large spatial extent of the fault area allowed us to also infer the average rupture velocity. Since the largest patch of slip was concentrated on the deepest part of the fault, this is the likely reason for the small tsunami waves that followed the earthquake, we also showed that the 2007 earthquake did not rupture the whole source zone of the previous 1833 event nor released the likely accumulated moment since then. This feature indicates that some slip has still to occur.

The results of this work have been published in the following paper:
Lorito S., **F. Romano**, A. Piatanesi and E. Boschi, (2008), Source process of the September 12, 2007, Mw 8.4 southern Sumatra earthquake from tsunami tide gauge record inversion, *Geophys. Res. Lett.*, *35*, L02310, doi:10.1029/2007GL032661.

GEOPHYSICAL RESEARCH LETTERS, VOL. 35, L02310, doi:10.1029/2007GL032661, 2008

Source process of the September 12, 2007, M_W 8.4 southern Sumatra earthquake from tsunami tide gauge record inversion

Stefano Lorito,[1] Fabrizio Romano,[1] Alessio Piatanesi,[1] and Enzo Boschi[1]

Received 13 November 2007; revised 20 December 2007; accepted 31 December 2007; published 31 January 2008.

[1] We infer the slip distribution and average rupture velocity of the magnitude M_W 8.4 September 12, 2007, southern Sumatra earthquake from available tide-gauge records of the ensuing tsunami. We select 9 waveforms recorded along the west coast of Sumatra and in the Indian Ocean. Slip distribution and rupture velocity are determined simultaneously by means of a non linear inversion method. We find high slip values (~10 m) into a patch 100 km long and 50 km large, between 20 and 30 km of depth, about 100 km north-west from the epicenter. We conclude this earthquake did not rupture the whole area of the 1833 event, indicating some slip has still to occur. Our estimate of rupture velocity is of 2.1 ± 0.4 km/sec. The relatively large depth of the main slip patch is the likely explanation for the low damaging observed tsunami. **Citation:** Lorito, S., F. Romano, A. Piatanesi, and E. Boschi (2008), Source process of the September 12, 2007, M_W 8.4 southern Sumatra earthquake from tsunami tide gauge record inversion, *Geophys. Res. Lett.*, *35*, L02310, doi:10.1029/2007GL032661.

1. Introduction

[2] On September 12, 2007 at 11:10:26 UTC an earthquake of magnitude M_W 8.4 occurred off the west coast of Sumatra about 130 km SW of Bengkulu. The epicenter was at 4.517°S and 101.382°E, between the Sunda trench and Bengkulu (Figure 1). The induced sea-floor displacement generated a tsunami of a moderate intensity given the earthquake magnitude, that nevertheless propagated through the Indian Ocean and was recorded, for example, by the tide-gauge at Salalah, Oman. In addition to minor aftershocks, the main shock was followed, 12 hours later, by another earthquake of magnitude M_W 7.9 near the Sumatra coast, 185 km SSE of Padang (Figure 1), that also generated a small tsunami recorded at Pointe La Rue and Rodrigues. Both earthquakes caused a total of 25 fatalities and 161 injuries (USGS; http://earthquake.usgs.gov/eqcenter/). The seismic sequence continued during the next two days, including a magnitude M_W 7.1 earthquake on September 13. This sequence took place in the same zone where the historical earthquakes of 1797 and 1833 generated significant tsunamis [*Nalbant et al.*, 2005].

[3] This is the third very large earthquake to occur on the Sunda megathrust in less than three years, each of which generated a significant tsunami (Figure 1). The great Sumatra-Andaman Mw = 9.2 earthquake and tsunami of December 26, 2004 ruptured an extent of almost 1,300 km, causing widespread casualties and destruction on the Indian Ocean coasts. The Sumatra-Andaman 2004 event was followed by the M_W 8.6 Nias earthquake and tsunami on March 28, 2005, generated along the Sunda trench contiguous with the southern end of the Sumatra-Andaman 2004 rupture zone. The Nias earthquake may have been a consequence of increased Coulomb failure stress induced by the Sumatra-Andaman earthquake [*McCloskey et al.*, 2005]. The rupture zone of the 2005 Nias earthquake significantly overlapped the rupture zone of the historic 1861 tsunamigenic earthquake [*Nalbant et al.*, 2005].

[4] The inversion of tsunami waveforms is an important tool for characterizing the seismic source of off-shore earthquakes. Recently, such inversions have been performed by *Piatanesi and Lorito* [2007] and by *Fujii and Satake* [2007] to characterize the kinematic rupture of the 2004 Sumatra-Andaman earthquake. A better understanding of the rupture process of tsunamigenic earthquakes originating on the Sunda megathrust is, in turn, a key issue for evaluating the possible consequences of future events both for risk mitigation and the design of warning strategies [*Borrero et al.*, 2006; *Geist et al.*, 2007; *McCloskey et al.*, 2007; *McCloskey et al.*, 2008].

[5] Here we perform the inversion of the waveforms recorded by 9 tide-gauge stations distributed in the Indian Ocean both in the near and in the far field with respect to the source zone. Our goal is to resolve the slip distribution and the average rupture velocity for the September 12, 2007 earthquake.

2. Sea-Level Data

[6] The tsunami waves generated by the September 12, 2007 earthquake were recorded by tide-gauge stations distributed throughout the Indian Ocean in the shallow waters of harbors and coastal sites. The data were downloaded in near real time at the website of the University of Hawaii Sea Level Center (UHSLC; http://ilikai.soest.hawaii.edu/RSL/). Most of these stations are operated by the Global Sea Level Observing System (GLOSS; http://www.gloss-sealevel.org/).

[7] The tsunami was also recorded by the DART buoy 23401 in the deep ocean northwest of Sumatra. This buoy is owned and operated by the Thailand Meteorological Department (TMD) in conjunction with National Disaster Warning Center of the Kingdom of Thailand. Data were available in real-time at the National Data Buoy Center (NDBC) website (http://www.ndbc.noaa.gov/dart.shtml), maintained by the U.S. National Oceanic and Atmospheric Administration (NOAA).

[8] Both the UHSLC and the DART 23401 available records of this tsunami have a sampling rate of one minute. The positions of the stations we choose for the inversion are

[1]Istituto Nazionale di Geofisica e Vulcanologia, Rome, Italy.

0094-8276/08/2007GL032661$05.00

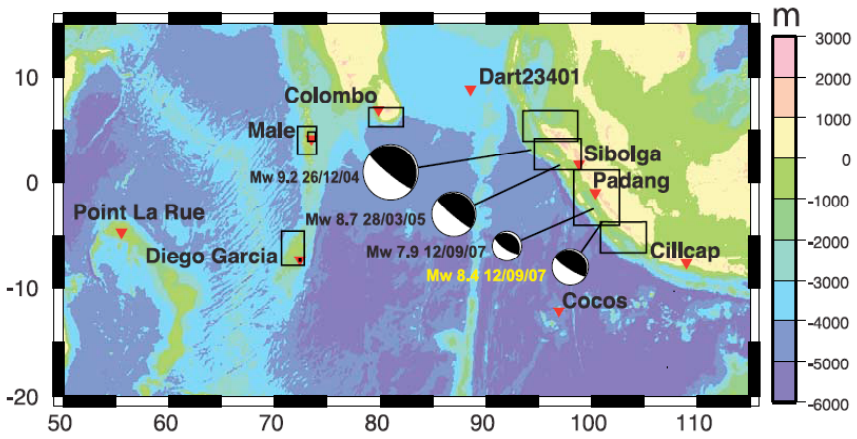

Figure 1. Epicenter and focal mechanism of the M_W 8.4 earthquake of 12 September 2007, and of the recent tsunamigenic earthquakes along the Sunda trench. Triangles indicate the positions of tide-gauge stations and DART buoy 23401. Bathymetry used for the simulation is represented by the colorscale. Rectangles are the limits of the nautical charts digitized to construct the bathymetric dataset.

plotted on the map of Figure 1. Before using these data in the inversion, we removed the tidal components calculated using least squares harmonic analysis to extract the tsunami signal. Then we selected only the first cycles of the waveforms as they carry more information about the source than later arrivals. We use an even narrower time window for Padang and Sibolga stations since they clearly show a resonant character in the later phases, likely associated with waves trapped in the channel between the forearc islands and the coast of Sumatra.

3. Seismic Source Parameters

[9] To define the dimensions of the causative fault, we use the spatial distribution of the aftershocks that occurred during 12 hours after the mainshock, available from the National Earthquake Information Center website of the U.S. Geological Survey (USGS; http://neic.usgs.gov/neis/epic/epic.html). A rupture area of length 350 km and width 200 km is large enough to contain all the aftershocks (Figure 2).

[10] The strike of the source is 323° roughly parallel to the Sunda trench [*Bird*, 2003]. The dip is fixed at 12°, using the quick moment tensor solution from the Global CMT project. We adopt a slip direction (rake) of 105°, roughly corresponding to that of the finite fault model calculated by C. Ji (http://www.geol.ucsb.edu/faculty/ji/big_earthquakes/2007/09/sumatra_seismic.html).

[11] We split the source region into 28 square subfaults of dimension 50 × 50 km (see Table S1 of the auxiliary material).[1]

4. Tsunami Modeling and Bathymetric Dataset

[12] For each of the subfaults we calculate the corresponding marigrams at the coordinates of the tide-gauges, which are the Green's functions we will use for the inversion.

[13] The initial seawater elevation is assumed to be equal to the coseismic vertical displacement of the sea bottom corresponding to an assumed "unitary" slip of 3 meters [*Piatanesi and Lorito*, 2007], as this is our initial guess for the average slip, and computed through the Okada's analytical formulas [*Okada*, 1992], while the initial velocity field in the ocean is assumed to be identically zero. The boundary conditions are pure wave reflection at the solid boundary (coastlines) and full wave transmission at the open boundary (open sea). The tsunami wave propagation from the source region to the tide-gauges is calculated by solving the non linear shallow water equations, with a finite differences scheme on a staggered grid. More detailed description of the equations as well as of the numerical method are given by *Lorito et al.* [2008], *Piatanesi and Lorito* [2007] and *Mader* [2001].

[14] The computational domain is shown in Figure 1. We choose a grid resolution for tsunami propagation of 1 arc-minute. The bathymetry grid is obtained by merging different bathymetric datasets [e.g., *Geist et al.*, 2007; *Fujii and Satake*, 2007]. We use as a background the 1 arc-min GEBCO bathymetry [*British Oceanographic Data Center*, 2003], version 1.02, available at the British Oceanographic Data Center website (http://www.bodc.ac.uk/data/online_delivery/gebco/). To improve the bathymetry in shallow waters, particularly along the coast of Sumatra and around some of the tide-gauges, we digitize the available 9 nautical charts [*United Kingdom Hydrographic Office*, 2005] (see Figure 1) in place of the GEBCO bathymetry and interpolate both on local 0.5 arc-min subgrids, before resampling to 1 arc-min and merging the rest of the whole domain.

5. Inversion

[15] We use a non linear inversion method based on the simulated annealing technique to simultaneously infer both

[1] Auxiliary materials are available in the HTML. doi:10.1029/2007GL032661.

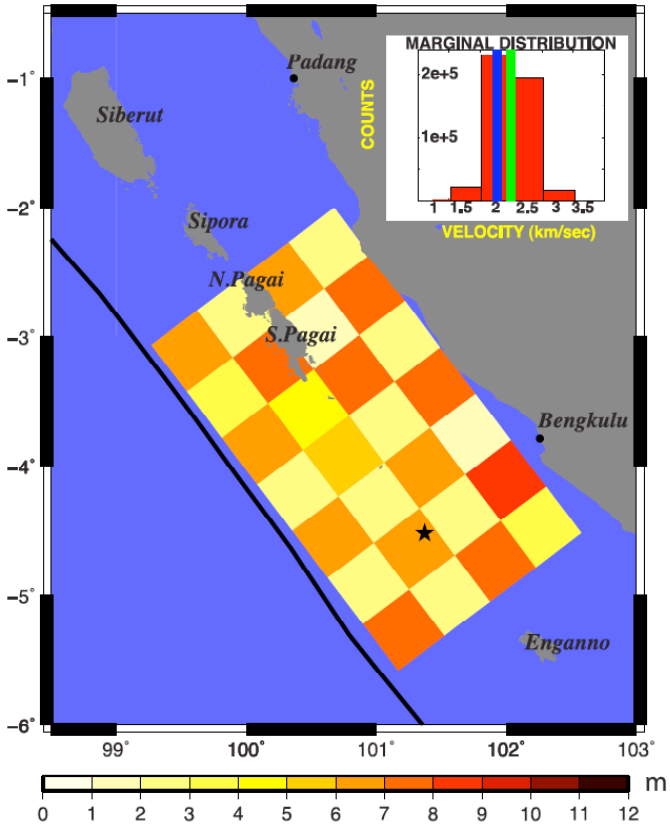

Figure 2. Slip distribution of the best model resulting from the checkerboard test, to be compared with the target values of alternately 2 and 6 meters. Rectangles represent the projection of the subfaults to the Earth's surface. Inset shows the marginal distribution of rupture velocities during the inversion; blue and green vertical solid lines represent the best and average model value respectively. The black star indicates the epicenter position of the September 12, 2007, event. Black line indicates the boundary between the Australian and Sunda plates [*Bird*, 2003].

slip distribution and average rupture velocity, with a L1–L2 hybrid norm as a cost function. The details are given by *Piatanesi and Lorito* [2007], *Lorito et al.* [2008], and references therein.

[16] The average rupture velocity is assumed to be the uniform velocity of a circular rupture front propagating out from the hypocenter on the fault plane. We consequently add the appropriate delay to the Green's function corresponding to each subfault, according to their distance along the rupture path.

[17] The resolving power of the inversion setup (azimuthal coverage, sampling rate, fault parametrization, etc.) is tested by means of a checkerboard experiment, with target slip values of alternatively 2 and 6 meters on adjacent subfaults. We first tune the subfault size by means of several checkerboard experiments, starting with larger sizes and ending up with 50 by 50 km. The synthetic waveforms generated with the checkerboard slip distribution are corrupted with Gaussian noise, with a variance that is 20% of the clean time series variance. To determine the optimal solution, for each subfault we let the slip range between 0 and 15 meters, at 1 meter steps, while the velocity ranges between 0.5 and 3.5 km/sec, at 0.5 km/sec steps.

[18] The target slip distribution, i.e. the checkerboard pattern, is reproduced fairly well by the best model (Figure 2, and Table S2 of the auxiliary material), with a root mean square of the differences between target and inverted values of 0.8 meters. Conversely, the target rupture velocity of 2.5 km/sec is not inferred exactly, as our best model estimation is 2 km/sec. Following *Piatanesi and Lorito* [2007], we estimate the uncertainty of each inverted parameters through an appraisal of the ensemble of the models explored during the search stage (see Table S2 of the auxiliary material). In particular, the marginal distribution of the explored rupture velocity values shows quite a broad peak ranging between 2 and 2.5 km/sec (see inset of Figure 2). The average model estimation of the rupture velocity is 2.2 ± 0.3 km/sec, is consistent with the target velocity of 2.5 km/sec. Later, in the real case inversion, we will therefore use the average model value, in place of the best model, as our estimate of the rupture velocity. The checkerboard experiment results indicate that the dataset has

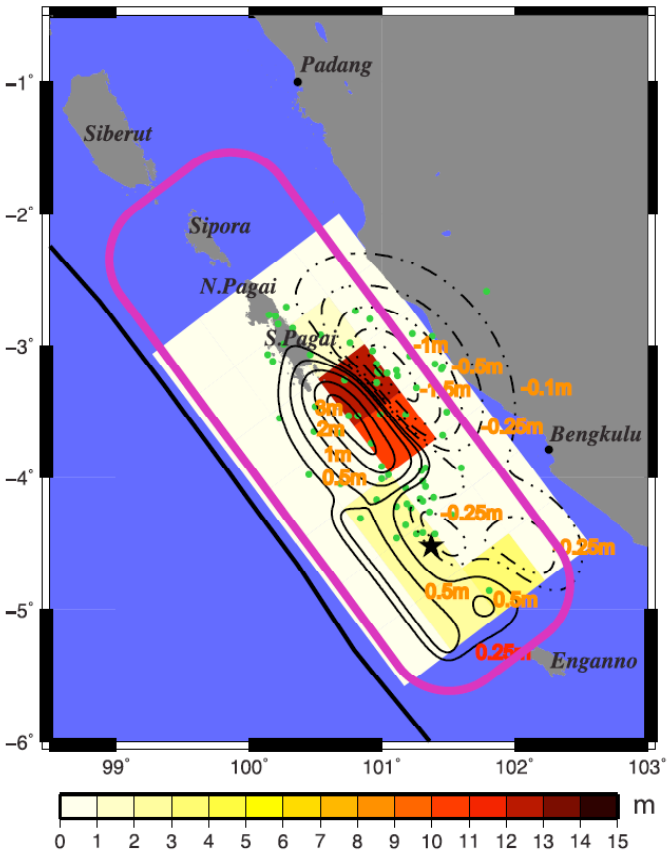

Figure 3. Slip distribution of the best model resulting from the September 12, 2007, Sumatra event. Rectangles represent the projection of the subfaults to Earth's surface. The black star indicates the epicenter of the mainshock and the green circles are the epicenter of the aftershocks that occurred 12 hours after the main event. Solid and dashed contour lines represent positive and negative vertical displacement respectively. Black line indicates the boundary between the Australian and Sunda plates [*Bird*, 2003]. Magenta line encompasses the approximate extent of the 1833 rupture.

the capability of resolving the main features of the rupture kinematics, with a good resolution for the slip and a lightly poorer resolution for the rupture velocity.

[19] To retrieve the rupture features of the September 12, 2007 earthquake, timing corrections of the Green's functions for the Cocos, Sibolga, Colombo, Diego Garcia and Pointe La Rue stations were made, in which we observed systematic differences between recorded and simulated phases. Relatively low resolution and uncertain nearshore bathymetry could have lead to travel times inaccuracy. An adjustment of travel times was also made by *Fujii and Satake* [2006], who observed discrepancies at the Cocos station while analyzing the 2006 Java tsunami. In the present case, however, we verified that the inverted rupture velocity is only slightly dependent on such arrival time adjustments.

[20] The slip distribution of the best model we find is shown in Figure 3. According to our results, the rupture propagated with a velocity of 2.1 ± 0.4 km/sec, and a relatively low slip (2 to 3 meters) near the hypocenter. The rupture then propagated to the northwest with a high slip concentration (up to 12 meters) at about 3–3.5°S and 101°E and a depth ranging between 20 to 30 km. We note that this high slip patch is surrounded by most of the aftershocks. We also plot the resulting coseismic vertical displacement, to be compared with the geodetic data when available. The whole set of results, best model and average model with associated errors is reported in Table S2 in the auxiliary material. The best model slip values always fall well inside the error bars. Conversely, the best model velocity lies at the upper edge of the error bar, confirming the best model is an extreme one for this case.

[21] The match between the recorded and inverted waveforms is generally good (Figure 4). At some stations, such as Padang (the nearest station to the source) and the DART buoy (the most reliable data) the fit is excellent. The worst fit is for Diego Garcia, with the period well reproduced but the amplitude overestimated. Overall, we satisfactorily

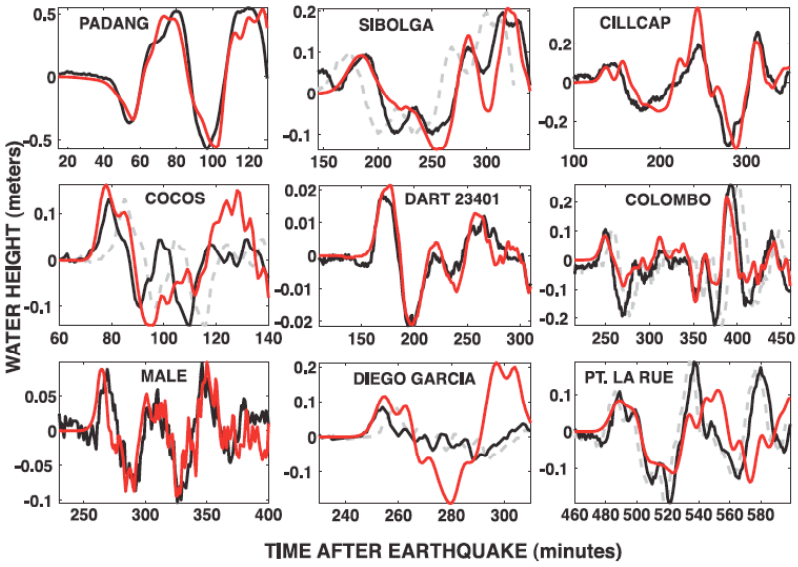

Figure 4. Comparison between the observed time-shifted records (black solid lines) and computed waveforms using the inverted best model (red solid lines). Grey dashed lines are the original observed records.

reproduce the main features of the September 12, 2007 tsunami wave amplitudes and periods.

6. Discussion

[22] The depth of the earthquake is an important factor in controlling the tsunami amplitude especially in the near field. Slip at greater depths produces relatively small vertical displacement of the sea bottom. In addition, high slip at intermediate depths on the megathrust produces maximum sea floor displacement in shallow waters, thus generating tsunamis with relatively small potential energy. The absence of significant slip at shallow depths is therefore a likely explanation for the generation of a relatively moderate tsunami associated with the 2007 earthquake, as it was the case for the M_W = 8.6 2005 Nias earthquake, that also released most of the slip at a similar depth [*Konca et al.*, 2007].

[23] Our results are in fair agreement, at least as regards the localization of the main slip patches, with the seismic inversions from Chen Ji (http://www.geol.ucsb.edu/faculty/ji/big_earthquakes/2007/09/sumatra_seismic.html), and in a lesser extent with Yuji Yagi (http://www.geo.tsukuba.ac.jp/press_HP/yagi/EQ/20070912/). Nevertheless, the above teleseismic inversions infer a lower maximum slip than our inversion of tsunami waveforms. Our best model features a seismic moment of 4.2×10^{21} N·m (using a shear modulus $\mu = 2.0 \times 10^{10}$ N/m^2 in the depth range 10–20 km, and $\mu = 6.0 \times 10^{10}$ N/m^2 in the range 20–30 km [*Geist and Bilek*, 2001]), corresponding to a magnitude M_W = 8.35 earthquake.

[24] *Nalbant et al.* [2005] indicated that the greatest current seismic threat from the Sunda megathrust may came from a repeat of the M ~ 9 1833 earthquake that overlaps with the source of the September 12, 2007 earthquake. Actually, the maximum slip we infer is consistent with tectonic loading but concentrated in a smaller area than the 1833 earthquake [*Natawidjaja et al.*, 2006].

7. Conclusions

[25] The source of the September 12, 2007 southern Sumatra earthquake is characterized by high slip values (~10 m) concentrated in a patch 100 km long and 50 km wide, located at depths between 20 and 30 km, and about 100 km north-west from the epicenter. Close to the trench the slip release in the 2007 earthquake is small or even absent at depths less than 10–15 km. A shallower slip patch of about 2–3 meters occurred only near the hypocenter. This resulted in a relatively low damaging tsunami if compared with the magnitude of the earthquake.

[26] The 2007 earthquake didn't rupture the whole source zone of the 1833 event nor released the likely accumulated moment since then. This poses a serious threat for a future big earthquake that will possibly occur in the unruptured area extending between South Pagai and the south of Siberut island.

[27] **Acknowledgments.** We gratefully acknowledge the contribution of Alessio Mautone, at the INGV SISMOS laboratory, who scanned the nautical charts we used in this work. Some figures have been produced with Generic Mapping Tools software [*Wessel and Smith*, 1998]. We thank Eric Geist and an anonymous reviewer: their careful reviews led to an improvement of the manuscript.

References

Bird, P. (2003), An updated digital model of plate boundaries, *Geochem. Geophys. Geosyst.*, *4*(3), 1027, doi:10.1029/2001GC000252.

Borrero, J. C., K. Sieh, M. Chlieh, and C. E. Synolakis (2006), Tsunami inundation modeling for western Sumatra, *Proc. Natl. Acad. Sci. U. S. A.*, *103*, 19,673–19,677.

British Oceanographic Data Center (2003), *The Centenary Edition of the GEBCO Digital Atlas* [CD-ROM], Liverpool, U. K.

Fujii, Y., and K. Satake (2006), Source of the July 2006 West Java tsunami estimated from tide gauge records, *Geophys. Res. Lett.*, *33*, L24317, doi:10.1029/2006GL028049.

Fujii, Y., and K. Satake (2007), Tsunami source of the 2004 Sumatra–Andaman earthquake inferred from tide gauge and satellite data, *Bull. Seismol. Soc. Am.*, *97*, S192–S207, doi:10.1785/0120050613.

Geist, E. L., and S. L. Bilek (2001), Effect of depth-dependent shear modulus on tsunami generation along subduction zones, *Geophys. Res. Lett.*, *28*, 1315–1318.

Geist, E. L., V. V. Titov, D. Arcas, F. F. Pollitz, and S. L. Bilek (2007), Implications of the 26 December Sumatra-Andaman earthquake on tsunami forecast and assessment models for great subduction-zone earthquakes, *Bull. Seismol. Soc. Am.*, *97*, S249–S270, doi:10.1785/0120050619.

Konca, A. O., V. Hjorleifsdottir, T.-R. A. Song, J.-P. Avouac, D. V. Helmberger, C. Ji, K. Sieh, R. Briggs, and A. Meltzner (2007), Rupture kinematics of the 2005 *M*w 8.6 Nias–Simeulue earthquake from the joint inversion of seismic and geodetic data, *Bull. Seismol. Soc. Am.*, *97*, 307–322, doi:10.1785/0120050632.

Lorito, S., A. Piatanesi, and A. Lomax (2008), Rupture process of the 18 April 1906 California earthquake from near-field tsunami waveform inversion, *Bull. Seismol. Soc. Am.*, in press.

Mader, C. L. (2001), *Numerical Modeling of Water Waves*, *Los Alamos Ser. Basic Appl. Sci.*, vol. 8, CRC Press, Boca Raton, Fla.

McCloskey, J., S. S. Nalbant, and S. Steacy (2007), Indonesian earthquake risk from co-seismic stress, *Nature*, *434*, 291, 2005.

McCloskey, J., A. Antonioli, A. Piatanesi, K. Sieh, S. Steacy, S. S. Nalbant, M. Cocco, C. Giunchi, J. D. Huang, and P. Dunlop (2007), Near-field propagation of tsunamis from megathrust earthquakes, *Geophys. Res. Lett.*, *34*, L14316, doi:10.1029/2007GL030494.

McCloskey, J., A. Antonioli, A. Piatanesi, K. Sieh, S. Steacy, S. S. Nalbant, M. Cocco, C. Giunchi, J. D. Huang, and P. Dunlop (2008), Tsunami threat in the Indian Ocean from a future megathrust earthquake west of Sumatra, *Earth Planet. Sci. Lett.*, *265*, 61–81, doi:10.1016/j.epsl.2007.09.034.

Nalbant, S. S., S. Steacy, K. Sieh, D. Natawidjaja, and J. McCloskey (2005), Seismology: Earthquake risk on the Sunda trench, *Nature*, *435*, 756–757, doi:10.1038/nature435756a.

Natawidjaja, D. H., K. Sieh, M. Chlieh, J. Galetzka, B. W. Suwargadi, H. Cheng, R. L. Edwards, J.-P. Avouac, and S. N. Ward (2006), Source parameters of the great Sumatran megathrust earthquakes of 1797 and 1833 inferred from coral microatolls, *J. Geophys. Res.*, *111*, B06403, doi:10.1029/2005JB004025.

Okada, Y. (1992), Internal deformation due to shear and tensile faults in a half-space, *Bull. Seismol. Soc. Am.*, *82*, 1018–1040.

Piatanesi, A., and S. Lorito (2007), Rupture process of the 2004 Sumatra-Andaman earthquake from tsunami waveform inversion, *Bull. Seismol. Soc. Am.*, *97*, 223–231, doi:10.1785/0120050627.

United Kingdom Hydrographic Office (2005), *Catalogue of Admiralty Charts and Publications, 2005 Edition*, Taunton, U. K.

Wessel, P., and W. H. F. Smith (1998), New, improved version of the Generic Mapping Tools released, *Eos Trans. AGU*, *79*, 579.

E. Boschi, S. Lorito, A. Piatanesi, and F. Romano, Istituto Nazionale di Geofisica e Vulcanologia, Via di Vigna Murata 605, I-00143 Rome, Italy. (lorito@ingv.it)

Chapter 6

Inverting for slip distribution, rupture velocity, rake and rigidity: the 2004 Sumatra earthquake

The 2004 Sumatra earthquake became famous over the world for its intensity (one of the largest in the last centuries) and for the tsunami that spread distruction all around the Indian Ocean interesting also very far places as the African continent. In this work we infer the slip distribution, the rupture velocity and the slip direction along the entire fault plane by performing a joint inversion of tsunami waveforms, GPS mesurements and satellite altimetry data. Moreover, we propose a new method, as we also estimate self-consistently the rigidity of the source zone. The latter resulted significantly lower than the PREM values at the corresponding depths. This rheological parameter is very important since it may play a significant role in the tsunami generation: in particular for slow earthquakes, a low rigidity value is sometimes necessary to explain how a relatively low seismic moment earthquake may generate significant tsunamis.

This work resulted in the following research paper now accepted with revision:
Lorito S., A. Piatanesi, V. Cannelli, **F. Romano**, and D. Melini (2009), Kinematics and Source Zone Properties of the 2004 Sumatra-Andaman Earthquake and Tsunami: Nonlinear Joint Inversion of Tide-Gage, Satellite Altimetry and GPS data, *J. Geophys. Res.*

Kinematics and Source Zone Properties of the 2004 Sumatra-Andaman Earthquake and Tsunami: Nonlinear Joint Inversion of Tide-Gage, Satellite Altimetry and GPS data

S. Lorito, A. Piatanesi, V. Cannelli, **F. Romano**, and D. Melini

Istituto Nazionale di Geofisica e Vulcanologia, Department of Seismology and Tectonophysics, Via di Vigna Murata 605, 00143 Rome, Italy

Abstract

We (re)analyzed the source of the 26 December 2004 Sumatra-Andaman earthquake and tsunami through a nonlinear joint inversion of an in-homogeneous dataset made up of tide-gages, satellite altimetry, and far-field GPS recordings. The purpose is two-fold: (1) the retrieval of the main kinematics rupture parameters (slip, rake, rupture velocity); (2) the inference of the rigidity of the source zone. We independently estimate the slip from tsunami data and the seismic moment from geodetic data, so to derive the rigidity. Our results confirm that the source of the 2004 Sumatra-Andaman earthquake has a complex geometry, constituted by three main slip patches, with slip peaking at ~30 meters in the Southern part of the source. The rake direction rotates counter-clockwise at North, according to the direction of convergence along the trench. The rupture velocity is higher in the deeper than in the shallower part of the source, consistently with the expected increase of rigidity with depth. It is also lower in the Northern part, consistently with known variations of the incoming plate properties and shear velocity. Our model features a rigidity (20-30 GPa), that is lower than PREM average for the seismogenic volume [*Dziewonski and Anderson*, 1981]. The source rigidity is one of the factors controlling the tsunamigenesis: for a given seismic moment, the lower the rigidity, the higher the induced seafloor displacement. The general consistence between our source model and previous studies supports the effectiveness of our approach to the joint inversion of geodetic and tsunami data for the rigidity estimation.

1. Introduction

The 26 December 2004 M=9.1-9.3 [*Stein and Okal*, 2005; *Chlieh et al.*, 2007] earthquake struck the Sumatra-Andaman region and generated a huge tsunami. This was the most devastating and deadly seismic event occurred during the last centuries, causing more than 250,000 fatalities and spreading destruction along the coasts of the whole Indian Ocean.

The 2004 Sumatra event produced the biggest and most complete ever dataset for a great earthquake and its associated tsunami. For example, the associated tsunami wave has been recorded by several tide-gages in the Indian Ocean, as well as in both the Pacific and Atlantic Oceans [*Merrifield et al.*, 2005; *Titov et al.,* 2005; *Dragani et al.,* 2006; *Joseph et al.,* 2006; *Nagarajan et al.*, 2006; *Obura,* 2006; *Rabinovich et al.*, 2006; *Tanioka et al.*, 2006b; *Tsuji et al.* 2006; *Rabinovich and Thomson*, 2007; *Thomson et al.,* 2007].

Since then, many researchers all over the world have been studying this earthquake, as testified by at least four special issues on scientific journals [*Gu,* 2006; *Tanioka et al.*, 2006a; *Bilek et al.*, 2007; *Satake et al.,* 2007], and by a number of other papers. In particular, some researchers investigate the (kinematical) properties of the source of this earthquake. Its unusual size (moment, extent, duration) made this earthquake a real benchmark for the refinement of inversion methods, based on many different types of geophysical data. In this paper we have used both tsunami (as recorded by tide-gages and altimeter satellites) and geodetic data.

Tanioka et al. [2006b] and *Piatanesi and Lorito,* [2007] propose models of the slip distribution and average rupture velocity of the seismic source based on the inversion of tide-gage records of the 2004 tsunami in the Indian Ocean. *Hirata et al.* [2006] estimate the tsunami source model by inverting the altimetry signals recorded by two satellites, which flew above the Indian Ocean about two hours after the earthquake. *Fujii and Satake* [2007] combine tide-gage and three satellite recordings of the tsunami and infer the rupture characteristics through a joint inversion of the two datasets.

On the other hand, geodetic data have been inverted by a number of authors to constrain the seismic source properties. *Banerjee et al.,* [2005], *Catherine et al.*, [2005], *Vigny et al.,* [2005], and *Hashimoto et al.* [2006] use far-field GPS recordings; *Gahalaut et al.* [2006] use near-field GPS recordings; *Subarya et al.* [2006], and

Banerjee et al. [2007] use both GPS records in the near-field and vertical motion of coral reefs. *Chlieh et al.* [2007] and *Pietrzak et al.* [2007] combine near- to far-field GPS and coral reefs data, and successively validate their results against tsunami data. A joint inversion of GPS and seismic data is performed by *Rhie et al.* [2007].

Nevertheless, there are still some open questions about the details of the source process solutions proposed by different authors. The situation is somewhat ameliorated when refining the modeling strategies, as demonstrated by the most recent inversions. *Sladen and Hébert* [2008] use an up-to-date structural model of the causative fault. *Hoechner et al.* [2008] reconciliate near- and far-field modeling of the coseismic displacement, by using a continental Earth's layering rather than an oceanic one.

In the present work, we combined tsunami and geodetic datasets in a joint inversion. Our in-homogeneous dataset is made up of (1) tide-gages, (2) satellite altimetry, and (3) far-field GPS recordings. In light of the results described above, we adopted a fault geometry with variable strike and dip [*Subarya et al.*, 2006]. We modeled the coseismic displacement at GPS sites by taking into account Earth's sphericity and layering, due to their importance in the far-field [*Banerjee et al.,* 2005]. However, we conservatively decided not to include near-field (campaign) GPS recordings in the inversion, because there is still some controversy about the real entity of the afterslip and post-seismic displacement they may contain, so that any modeling attempt unavoidably requires some *a-priori* assumptions [cf. *Banerjee et al.,* 2007; *Chlieh et al.,* 2007; *Hoechner et al.,* 2008].

The purpose of the present paper is two-fold. First, to infer simultaneously the main kinematics rupture parameters (slip, rake, rupture velocity); second, the estimation of the rigidity of the source zone. These estimations have been performed by means of a nonlinear inversion combining datasets of different nature. In order to have the rigidity as a free parameter in the inversion, we combined a slip-based model for the tsunami generation with a moment-based model for the coseismic displacement at the far-field GPS stations. We thus exploited the proportionality between the slip and the seismic moment, through the rigidity (and area) of the source zone.

As pointed out in a series of papers [*Bilek and Lay,* 1998; *Bilek and Lay,* 1999; *Geist and Bilek,* 2001], rigidity values along interplate megathrust faults in subduction zones can be significantly lower than Preliminary Reference Earth Model (PREM) values [*Dziewonski and Anderson*, 1981]. This has the net effect of increasing the slip

corresponding to a given seismic moment – because of the proportionality between the moment and the slip through rigidity (and fault area) – and consequently to increase the coseismic displacement and the initial tsunami amplitude. The above estimates are based on the proportionality existing between rigidity itself and source duration, when assuming constant stress drop [*Bilek and Lay,* 1999]. In particular, depth-dependent variations of the rigidity are suggested by the analysis of both 2004 Sumatran earthquake aftershocks and of earthquakes occurred before 2004, which feature longer durations for shallower events [*Bilek*, 2007].

Here, we independently determined rupture velocity and rigidity for different portions of the source zone. We also investigated along-strike variations of the fault-zone character. There is in fact strong evidence of a unilateral rupture propagating from South to North, but propagating slower in the northern part [e.g. *Ammon et al.*, 2005; *Menke et al., 2006*]. This is perhaps due either to a change in the frictional conditions and/or source zone rigidity, or resulting from structural variations of the subduction zone [*Kennett and Cummins,* 2005; *Shapiro et al.,* 2008].

In what follows, we first describe the data selection and pre-processing, along with the Green's functions generation strategy relative to each of the datasets. Then, we discuss the adopted source geometry parameterization. Later, synthetic checkerboard tests are used to assess the resolving power, both for separate and joint inversions. Finally, the results obtained for the Sumatra earthquake and tsunami are shown and discussed.

2. Data and modeling

Tsunami (tide-gage and satellite altimetry) data selection and processing

After a careful inspection of the available tide-gage records in the Indian Ocean, we selected 13 stations (Fig. 1, and Tab. 1), which is more or less the same dataset used in previous tide-gage inversions [*Tanioka et al.,* 2006b; *Piatanesi and Lorito,* 2007; *Fujii and Satake*, 2007]. The criteria for selection have been a good signal to noise ratio, as well as a sufficient azimuthal distribution around the earthquake source.

Some of the records were available as plots made by analogic devices [HDRTN]. We digitized them with a sampling interval of 5 minutes. The digitized marigrams as well as the Sibolga marigram [GGCI] included ocean tides that we removed by high-pass

filtering the records. All other marigrams were recorded by digital instruments [GLOSS/UHSLC; NIO], with sampling intervals ranging from 2 to 10 minutes. They were available on the web as de-tided residuals, and then they are directly comparable to our simulated marigrams that do not include tidal effects. We chose for each of the selected records a time window that includes, in most of the cases, only the first few oscillations after the first tsunami wave arrival. We thus try to minimize the contribution to signals of local effects (e.g. resonance of the bays, reflections), which could shadow information about the seismic source and are more difficult to simulate, due to eventual inaccuracy of the bathymetric model.

The tsunami wave was also recorded at open sea – in the middle of the Indian Ocean – by radar altimeters on board of the Jason-1, Topex/Poseidon, Envisat and GFO satellites [*Gower*, 2005; *Smith et al.*, 2005]. We have downloaded the datasets recorded by two of them from the web archive of the Jet Propulsion Laboratory [PO.DAAC]. We chose to employ only Jason-1 and Topex altimetry records, as they captured the leading tsunami wave while it was propagating westward, roughly 2 hours after the earthquake. Other altimeter satellites recorded the tsunami later on, thus having a poorer signal to noise ratio and including secondary waves reflected by the Indian coasts.

The satellites cyclically cover the same tracks, that is the same orbits with respect to the Earth's surface, and each of those is termed a "pass". The portions of Jason-1 and Topex pass 129 we considered in this study are shown in Fig. 1. We chose such portions with attempting to include as much as possible the main wave and minimizing the presence of recording gaps [cf. *Ablain et al.*, 2006]. Jason-1 recorded the tsunami signal for about 11 minutes during its pass 129 (cycle 109). Topex recorded the tsunami wave on pass 129 (cycle 452). We first averaged a few cycles preceding the tsunami, and then subtracted the result from the signal in order to extract the tsunami signal from the background [cf. *Fujii and Satake*, 2007].

Tsunami forward modeling, bathymetry, and Green's functions

Tsunamis are considered long shallow-water gravity waves, since their wavelength is usually much larger than the sea depth. In this study we used the nonlinear shallow water equations written as follows

$$\begin{cases} \dfrac{\partial(z+h)}{\partial t} + \nabla \cdot [\mathbf{v}(z+h)] = 0 \\ \dfrac{\partial \mathbf{v}}{\partial t} + (\mathbf{v} \cdot \nabla)\mathbf{v} = -g\nabla z + \mathbf{C} \end{cases} \qquad (1)$$

In eqs. (1), z represents the water elevation above sea level, h the water depth in a still ocean, $\mathbf{v}$ the depth-averaged horizontal velocity vector, g the gravity acceleration, and $\mathbf{C}$ the Coriolis force. The boundary conditions are pure wave reflection at the solid boundary (coastlines) and full wave transmission at the open boundary (open sea). The equations are solved numerically by means of a finite difference technique on a staggered grid [*Mader*, 2001]. The initial seawater elevation is assumed to be equal to the coseismic vertical displacement of the sea bottom, computed through the Okada's analytical formulas [*Okada*, 1992], while the initial velocity field is assumed to be identically zero. Numerical modeling of the tsunami is carried out in the domain depicted in Fig. 1 with 1 arc-minute of spatial resolution for the simulation of the tide-gage records and 2 arc-minutes for the simulation of the satellite recordings, with consequently adjusted time step to ensure numerical stability.

As a bathymetric dataset for the generation of the tsunami Green's functions, we employed the GEBCO dataset [2003, and updates http://www.bodc.ac.uk/data/online_delivery/gebco/ (last accessed March 2009)]. This dataset is mainly based on ship soundings data; however, the location and density of the ship tracks are not explicitly stated in the GEBCO documentation [*Marks and Smith*, 2006]. We therefore decided to follow the practice broadly used in some recent papers [*Fujii and Satake*, 2007; *Geist et al.*, 2007; *Grilli et al.,* 2007; *Hébert et al.,* 2007; *Iouaualen et al.,* 2007; *Sindhu et al.,* 2007; *Lorito et al.*, 2008b; *Fujii and Satake*, 2008], whose authors merged different bathymetric datasets. We then scanned and geo-referenced 33 nautical charts (Fig. 1, Tab. 2) that we subsequently digitized, for a total of 1.945.328 data points. We paid special attention to include shallow water regions both around the tide-gage locations and in the source zone. The digitized bathymetric dataset is available upon request to S.L. (stefano.lorito@ingv.it). Before

merging the digitized and GEBCO bathymetries, we removed all the points with elevation z in the range -200 m < z < 10 m from the regions of GEBCO covered by the points digitized from the nautical charts. This step allowed to replace the most inaccurate points in GEBCO and to reconstruct the coastlines basing on the digitized dataset. At this point we merged the datasets and interpolated them on a regular grid of 0.5 arc-min spacing. We used an interpolation code (developed by Pavel Sakov, and available at http://geog-pc40.ulb.ac.be/grass/nnbathy/) that implements the natural neighbours algorithm [*Sambridge et al.*, 1995]. We then downsampled the gridded bathymetry to 1 arc-min with the "blockmean" GMT command, and finally smoothed the dataset by means of the GMT "surface" command, with a tension of 0.35 [*Smith and Wessel*, 1990].

The usual way to deal with the problem of retrieving the slip distribution on the fault from tsunami data is to first subdivide the fault plane into subfaults and then compute the Green's functions – i.e. the tsunami waveform at a station produced by each of the subfaults – by solving the linear form of eqs. (1). The tsunami waveforms produced by the whole source are then calculated as a linear combination of the Green's functions. The linear approximation is no longer valid for tsunami propagation in very shallow water and when the wave amplitude is relatively large. We faced this issue by following the approach of *Piatanesi and Lorito* [2007]. We used the nonlinear shallow-water equations to compute the Green's functions matrices $\mathbf{H}_{GAGE,sf}$ and $\mathbf{H}_{SAT,sf}$, corresponding to tide-gage and satellite datasets respectively (label sf indicates a generic subfault). We used "unit" slip amplitude $d_0 = 10m$ for each elementary subfault, since this is roughly the mean slip value along the whole fault, according to seismic moment estimations [*Stein and Okal*, 2005]. We repeated the calculations two times for each subfault, with mutually orthogonal rake angles of $\pi/4$ and $3/4\pi$. We exploited the linear approximation only when performing the linear combination of the Green's functions of the single subfaults (roughly speaking, we linearized the problem around the mean slip value).

Given any slip and rake distribution d_{sf}, r_{sf}, where the subscript sf ranges within the entire set of subfaults, the synthetic waveforms then read:

$$\begin{cases} \mathbf{H}_{GAGE}(\mathbf{X},t) = \sum_{sf} \frac{d_{sf}}{d_0}\left[\cos(r_{sf} - \pi/4)\mathbf{H}^{\pi/4}_{GAGE,sf}(\mathbf{X},t+\delta t_{sf}) + \sin(r_{sf} - \pi/4)\mathbf{H}^{3/4\pi}_{GAGE,sf}(\mathbf{X},t+\delta t_{sf})\right] \\ \mathbf{H}_{SAT}(\mathbf{X},t) = \sum_{sf} \frac{d_{sf}}{d_0}\left[\cos(r_{sf} - \pi/4)\mathbf{H}^{\pi/4}_{SAT,sf}(\mathbf{X},t+\delta t_{sf}) + \sin(r_{sf} - \pi/4)\mathbf{H}^{3/4\pi}_{SAT,sf}(\mathbf{X},t+\delta t_{sf})\right] \end{cases} \quad (2)$$

where the labels $\pi/4$ and $3/4\pi$ distinguish between orthogonal rake angles, for each of the subfaults. The rupture is moreover allowed to propagate at a velocity v_{sf} from the South to the North, reflected by the delay δt_{sf} from the earthquake origin time.

In detail, we obtained the Green's functions $\mathbf{H}_{GAGE,sf}$ at the tide-gage stations by sampling the simulated water height evolution in correspondence of the actual tide-gages coordinates and with the actual sampling rate (Tab .1). We conversely obtained the satellite Green's function $\mathbf{H}_{SAT,sf}$ for each point of the satellite track by spatially averaging the water height in square regions of 4 arc-minutes, as this roughly corresponds to what the satellite altimeter actually measure [cf. *Gower*, 2005]. We moreover took into account that the altimetry recording is a function of both space and time, as the satellites measure at different times along their tracks [cf. *Sladen and Hébert*, 2008].

Geodetic forward modeling and GPS dataset

Static surface deformation field data associated with the 2004 Sumatra earthquake shows that the elastic deformation of Earth caused static offsets recorded at continuously operating GPS stations at distances of up to 4500 kilometers off from the epicenter [*Boschi et al.*, 2006; *Banerjee et al.*, 2007].

We modeled the associated coseismic surface displacements adopting the theoretical model of global coseismic deformation originally proposed by *Piersanti et al.* [1995], and later refined by *Soldati et al.* [1998] and by *Boschi et al.* [2000]. It is a semi-analytical, spherical model which assumes an incompressible, layered, self-gravitating Earth with Maxwell linear viscoelastic rheology, and it is capable of modeling both elastic and viscoelastic responses induced by a seismic dislocation.

The set of differential equations governing the model is:

$$-\rho_0 \nabla \tilde{\phi}_1 - \nabla(\tilde{\mathbf{u}} \cdot \rho_0 g_0 \mathbf{e}_r) + \nabla \cdot \tilde{\mathbf{T}} = \rho_0 \tilde{\mathbf{f}} \tag{3}$$

$$\nabla \cdot \tilde{\mathbf{u}} = 0 \tag{4}$$

$$\nabla^2 \tilde{\phi}_1 = 0 \tag{5}$$

$$\tilde{\mathbf{T}} = 2\mu \tilde{\mathbf{E}} + \tilde{p}_1 \mathbf{I} \tag{6}$$

$$\tilde{\mathbf{E}} = \frac{1}{2}\left[\nabla \tilde{\mathbf{u}} + (\nabla \tilde{\mathbf{u}})^T\right] \tag{7}$$

where the tilde denotes the Laplace-transformed variables and the subscripts *0* and *1* refer to the equilibrium and perturbed values, respectively; g_0 is the reference gravity acceleration, p_1 is the incremental pressure, ρ_0 is the density, $\mathbf{u}$ is the deformation; ϕ_1 is the perturbation to geopotential and $\tilde{\mu}$ is a Laplace-trasformed rigidity defined as $\tilde{\mu} = \frac{\mu s}{s + \mu/\eta}$, where s is the Laplace complex variable, μ the rigidity and η the viscosity. Eq. (3) states the momentum conservation in the presence of a seismic dislocation represented by the equivalent body force $\tilde{\mathbf{f}}$. Eq. (4) is the incompressibility condition and eq. (5) is the Laplace equation for the perturbation to gravitational potential $\tilde{\phi}_1$ due to the displacement field $\tilde{\mathbf{u}}$. Eq. (6) relates the incremental stress field $\tilde{\mathbf{T}}$ to the infinitesimal strain tensor $\tilde{\mathbf{E}}$ via the viscoelastic constitutive relation. We refer the reader to works cited above for details concerning both the analytical solution of the eqs. (3-7) and the associated numerical issues.

We calculated the coseismic GPS offsets induced by the Sumatra earthquake at a station subset of the 108 far-fields GPS static offsets assembled by *Banerjee et al.* [2007] (their tables S1 and S2 in the electronic supplement). In particular, we selected 84 GPS stations with longitudes between 65° E and 130° E and latitudes between 25° S and 45° N (Tab. 3, some in Fig. 1) since the incompressibility approximation may lead to an overestimation of displacements in the very far-field [*Boschi et al.*, 2006; *Banerjee et al.*, 2005]. The selected data include the coseismic horizontal displacement vectors derived from the analysis of continuous GPS (CGPS) measurements by *Banerjee et al.* [2007] plus the CGPS and campaign GPS (SGPS) coseismic horizontal displacements derived from *Vigny et al.* [2005], and corrected

for postseismic relaxation by *Banerjee et al.* [2007]. The 84 far-field stations are both CGPS sites of permanent global and regional GPS networks (principally from IGS [*Dow et al.*, 2005] and SuGAr) and SGPS sites from surveys conducted by regional institutes (for further details, see *Banerjee et al.* [2007] and references therein).

In the joint inversion we excluded the northern Sumatra and the Andaman and Nicobar Islands SGPS coseismic horizontal surface displacements provided by *Banerjee et al.* [2007] (their tables S3 and S4 in the electronic supplement) because there are some (partly) controversial findings by different authors, regarding the amount of afterslip and/or post-seismic signal that may be superposed to the coseismic contribution in such measurements [cf. *Banerjee et al.*, 2007; *Chlieh et al.*, 2007; *Hoechner et al.*, 2008]. As we will discuss later, the exclusion of near-field data comes at the price of a resolution loss on small-scale source structure.

We employed a four-layer stratification model, which includes an 80 km elastic lithosphere, a 200 km thick asthenosphere, a uniform mantle, and a fluid core. All the mechanical parameters have been obtained by means of a weighted volume average of the corresponding parameters of the PREM [*Dziewonski and Anderson*, 1981].

Each subfault plane is subdivided into a two-dimensional distribution of point seismic sources, located on the nodes of a grid with 15 km spacing. A unit seismic moment $M_0 = \mu_0 A_0 d_0$ is fixed for each elementary subfault, where $\mu_0 = 56\ GPa$ is a "unit" subfault rigidity, A is the subfault area and $d_0 = 10m$ is a "unit" slip, which is the same value we used for the tsunami Green's functions. At the GPS stations coordinates $\mathbf{X}$, the total coseismic displacement $\mathbf{U}_{GPS,sf}$ due to each subfault – the Green's function – is computed by linear superposition of the displacements $\mathbf{u}^i_{GPS}$ due to N_{sf} equally spaced point sources, i.e.

$$\mathbf{U}_{GPS,sf}(\mathbf{X}) = \sum_{i=1}^{N_{sf}} \mathbf{u}^i_{GPS}(\mathbf{X}) \qquad (8)$$

For each of the subfaults, the calculation is performed for each of the mutually orthogonal rake angles $\pi/4$ and $3/4\pi$.

Given any slip, rake and rigidity distribution d_{sf}, r_{sf}, μ_{sf} over the entire source, the synthetic displacement at the GPS stations is then calculated as a combination of the contribution by the single subfaults Green's functions, and of mutually orthogonal rake pairs for each of the subfaults:

$$\mathbf{U}_{GPS}(\mathbf{X}) = \sum_{sf} \frac{\mu_{sf} d_{sf}}{\mu_0 d_0} \left[\cos(r_{sf} - \pi/4) \mathbf{U}^{\pi/4}_{GPS,sf}(\mathbf{X}) + \sin(r_{sf} - \pi/4) \mathbf{U}^{3/4\pi}_{GPS,sf}(\mathbf{X}) \right] \quad (9)$$

or, equivalently,

$$\mathbf{U}_{GPS}(\mathbf{X}) = \sum_{sf} \frac{M_{sf}}{M_0} \left[\cos(r_{sf} - \pi/4) \mathbf{U}^{\pi/4}_{GPS,sf}(\mathbf{X}) + \sin(r_{sf} - \pi/4) \mathbf{U}^{3/4\pi}_{GPS,sf}(\mathbf{X}) \right] \quad (10)$$

where $M_{sf} = \mu_{sf} A_{sf} d_{sf}$ is the seismic moment of the subfault with area equal to A_{sf}.

3. Parameterization

Fault geometry, subfaults

As a source zone model for the Sunda megathrust we used the structural representation proposed by *Subarya et al.* [2006], their "model B". This is a model based on teleseismic and local earthquakes observation as well as on volcanoes location. It is a curved plate interface, which dips at only a few degrees at the trench, and projects to about 100 km depth beneath the volcanic arc. The fault model features an increasing dip in the northern profiles. We averaged the nodes of *Subarya et al.* [2006] into much broader rectangular fault patches (Table 4, Fig. 1). We thus defined a set of 18 subfaults, with variable strike, dip, area, position, and depth. We ended up with two rows of 9 subfaults each, one shallower and one deeper, extending from about 1.5°N to 14°N, that is from Simeulue Island to the Andaman Islands. The total linear length spanned by the entire fault is almost 1500 km, with a subfault length of ~160 km and a width of ~105 km on the average. The subfaults in the shallower row extend in depth from about the surface down to ~10 km; those in the deeper row from ~10km to ~36km.

Inversion parameters

We have subdivided the fault plane into subfaults and used the Green's functions method.

In the case of the tsunami Green's functions, slip and rake (d_{sf}, r_{sf}), are the input parameters for the Okada's formula. The initial vertical displacement transferred to the water is then propagated to both the tide-gages and along satellite tracks by numerical solution of nonlinear shallow water equations. Additionally, we included a rupture velocity v_{sf}, representing the (variable) velocity of the rupture while propagating from South to North. We only imposed that the rupture be unilateral. Conversely, the 4 southernmost subfaults, around the epicenter and comprising Simeulue islands (Fig. 2), rupture simultaneously. We moreover allowed the shallow and deep subfaults subsets to rupture independently, so that the rupture may propagate at different velocities in the shallower and in the deeper part of the source.

The GPS Green's functions are calculated with the seismic moment $M_{sf} = \mu_{sf} A_{sf} d_{sf}$ (and rake r_{sf}) as input for a global coseismic deformation model, yielding the horizontal displacement at the far-field GPS sites.

To summarize, the synthetic marigrams and the synthetic offset at GPS stations can be represented as:

$$\begin{cases} \mathbf{H}_{GAGE}(\mathbf{X},t) = \sum_{sf} d_{sf} \tilde{\mathbf{H}}_{GAGE,sf}(\mathbf{X}, r_{sf}, v_{sf}) \\ \mathbf{H}_{SAT}(\mathbf{X},t) = \sum_{sf} d_{sf} \tilde{\mathbf{H}}_{SAT,sf}(\mathbf{X}, r_{sf}, v_{sf}) \end{cases} \qquad (11)$$

$$\mathbf{U}_{GPS}(\mathbf{X}) = \sum_{sf} \mu_{sf} d_{sf} \tilde{\mathbf{U}}_{GPS,sf}(\mathbf{X}, r_{sf}) \qquad (12)$$

where the tilde appears as we incorporated into the Green's functions all parameters but slip and rigidity of the single subfaults.

An inversion of the tsunami data alone would allow to retrieve slip, rake, and rupture velocity, by means of eqs. (11); an inversion of the GPS data alone would allow to retrieve seismic moment and rake, by means of eq. (12), and indirectly the slip for a given rigidity value. The joint inversion of the tsunami and GPS datasets allows to invert four free parameters: slip, rake, rupture velocity, and rigidity. Additionally, eqs. (11) are non-linear in the velocity, as well as eq. (12) is non-linear because of the

product between rigidity and slip: a simultaneous inversion of the whole parameter set therefore requires a non-linear inversion method.

With the use of a single modeling tool for coseismic displacement modeling (for both GPS and tsunami) the rigidity inversion would not have been possible. We thus chose a slip-based model to compute the vertical displacement in the near-field, and a moment-based model to calculate the horizontal displacement in the far-field. This approach has the advantage of letting only the slip as a coefficient in eqs. (11), then allowing the rigidity to be determined by means of eq. (12).

In what follows, we discuss our choices. The Okada's formulas, that is the elastic homogeneous half-space approximation, is widely used for the calculation of the near-field displacement [e.g., *Fujii and Satake*, 2007; *Pietrzak et al.*, 2007]. While sphericity may be ignored at the fault scale, crustal layering, or the presence of a superficial soft sediment layer, could play a significant role. In the present case of a low-angle thrust fault, however, the differences between the vertical displacement generated using Okada's formulas and using a layered model such as EDGRN/EDCMP [*Wang et al., 2003*] are not in fact really pronounced, say less than 10% [*Geist,* 1999; *Amoruso and Crescentini,* 2004; *Zhao et al.*, 2004; *Megna et al.*, 2008]. Additionally, slip-based source models are only slightly dependent on rigidity, if not at all [*Tinti and Tonini*, 2005; *Geist et al.,* 2007]. On the other hand, it is not uncommon to combine different modeling tools or geometries, depending on the nature of the data. An example is the combined inversion of seismic, tsunami and geodetic data of *Ichinose et al.* [2007]. They compute the vertical coseismic displacement Green's functions using a layered Earth's model, while the tsunami Green's functions are computed using the equations of Okada to derive the initial sea surface height changes. Our scheme is moreover comparable to that adopted by *Rhie et al.* [2007], who calculate the GPS offsets in the near-field with a flat layered model, and the long period Green's seismic waveforms by means of a normal mode summation method in spherical geometry with a PREM-layered rheology. Their formulas at page 2 are indeed the equivalent of our eqs. (11) and (12). The most remarkable difference is that they *a-priori* fix the fault rigidity.

4. Nonlinear inversion

Inversion technique

We simultaneously inverted for slip, rake, rupture front velocity, and fault rigidity. We then faced a nonlinear inversion problem and solved it following *Piatanesi and Lorito* [2007], and *Piatanesi et al.* [2007], which use the "heat bath algorithm" implementation of the simulated annealing technique [*Rothman*, 1986]. This technique is based on a large sampling of the model space, and progressive concentration of the search on regions characterized by low values of the cost function, i.e. where the optimal models are likely to be found.

We compared the observed and synthetic datasets by means of two different cost functions for the tsunami and geodetic datasets. For the tsunami dataset, which is composed of time series, we used a cost function that has proven to be sensible both to amplitude and phase matching [*Spudich and Miller*, 1990; *Sen and Stoffa*, 1991]. It is expressed as follows:

$$E(m) = \sum_{k=1}^{N} \left[1 - \frac{2 \sum_{t_i}^{t_f} (u_O(t) u_S(t))}{\sum_{t_i}^{t_f} u_O^2(t) + \sum_{t_i}^{t_f} u_S^2(t)} \right]_k \qquad (13)$$

In eq. (2) u_O and u_S are the observed and synthetic waveforms respectively, t_i and t_f are the lower and upper bounds of the time window and N is the number of records used in the inversion. At each inversion step, the above cost function (13) is evaluated two times, one for the tide-gage misfit, and one for the satellite data misfit. We assigned a relative weight to each tide-gage contributing to the cost function in order to take into account non-uniformity in the sampling rate of the records (see Table 1). We also assigned a relative weight of one fourth to Topex data with respect to Jason-1 data, to take into account the disproportion between their latitude coverage (Fig. 1). On the other hand, for the geodetic dataset, we used a standard L_2-norm as a cost function to quantify the misfit between experimental and synthetic datasets.

In the implementation of the joint inversion, the cost functions for the three datasets are summed up to obtain the global cost function. Relative weights are assigned to each cost function, in order to guarantee the maximum possible overlapping among their ranges of variation during the whole inversion. This is not straightforward, as the three separate cost functions have very different behaviors depending on their sensitivity to the variations of each parameter. We verified that a progressive increasing of the relative weight assigned to the tsunami dataset with respect to the geodetic dataset results in a progressive loss of resolution for the rigidity parameter, because the latter doesn't appear in eq. (11). On the other hand, the result of increasing the relative weight of the geodetic dataset implies a loss of resolution on both slip and rigidity, as a consequence of the intrinsic trade off between them (eq. (12)). We then empirically tried to give, on the average, similar weights to the three datasets, by means of synthetics checkerboard tests similar to those presented in a later section. We nevertheless verified that in the "real case" inversion, the results presented below in the case of the Sumatra 2004 earthquake are quite robust with respect to weights variations around the chosen values.

We introduce *a-priori* information in the solution by imposing lower and upper bounds to the range of variation of the source parameters, and on their steps between extreme values. The slip value is allowed to vary between 0 and 35 meters on each subfault, at 1 meter steps. The rake is allowed to range between 90° and 135°, at 5° steps. The rupture velocity between 0.25 and 5.0 km/s, at 0.25 km/s steps. Finally, the rigidity is allowed ranging between 5 and 50 GPa, at steps of 5 GPa.

Inversion of tsunami data: checkerboard test

As a first stage, we studied the resolution of the tsunami data, both recorded by satellites and tide-gages. To check the effectiveness of our method in inverting for both the slip and rake distribution and the rupture velocity, we performed a series of synthetic tests [cf. *Piatanesi and Lorito*, 2007; *Lorito et al.*, 2008a; *Lorito et al.*, 2008b].

Figure 2 (left panel) depicts the synthetic rupture model we used in the main synthetic test. It consists of a slip distribution having a checkerboard pattern, with slip values alternating between 5 and 15 meters on adjacent subfaults. We assigned three different values to the rake, letting its value change only along strike. We chose a rake of 90° for the group of the 6 southernmost subfaults (both shallow and deep), then

130° for the next 6, and again 90° for the 6 northernmost ones. We verified by means of some preliminary tests (not shown) that allowing three different values along strike is a good compromise between the resolving power of our dataset and the possibility of following the rake variation along strike for the 2004 earthquake [cf. *Menke et al.*, 2006]. During the inversion, we have consequently forced the rake values within each of the 6-subfaults groups to be equal, as in the target synthetic model. The rupture in this test is chosen unilateral from South to North, as in the Sumatra earthquake. The target model features four different rupture front velocities. The rupture front is fixed to propagate with different velocities in the shallower and the deeper subfaults, and for both of them it slows down in the second half of the rupture. Along the shallower ones, the rupture is imposed to propagate at an average velocity of 1.5 km/s from the epicenter to about 6°N, and then at 1 km/s. Along the deeper subfaults, the velocity is fixed to 2.5 km/s south of 6°N and to 2 km/s north of 6°N. Again, during the inversion, the explored models are forced to have the same velocity pattern. Similarly to what we have done for the rake, we have proven with other synthetic tests (not shown) that this is the spatial resolution limit for the inversion of the rupture front velocity.

The synthetic waveforms, produced with such a source process both for tide-gages and satellites, are corrupted by adding a gaussian random noise with a variance that is 10% of the clean waveform amplitude variance [cf. *Sen and Stoffa*, 1991; *Ji et al.*, 2002], to mimic eventually non-modeled uncertainties.

The results indicate that the source process is in principle very well constrained by the tsunami data, provided a careful tuning of the spatial resolution for each of the parameters. The best inverted model is in fact very similar to the target one: the checkerboard shape of the slip distribution is very well reproduced (right panel of Fig. 2, column 2 of Tab. 5), and the slip values have a maximum difference to the target ones of 1 meter. The rake distribution is estimated exactly (Tab. 5, col. 3). The rupture velocity distribution also is estimated exactly (see Table 5, col. 2), with the exception of the deeper northernmost stretch of the source, where the difference between the inverted and the target velocity is however only 0.25 km/s.

Inversion of geodetic data: checkerboard test

As a second stage, we repeated the checkerboard test with the geodetic dataset. In this case, the free parameters to be determined by means of the inversion are the slip and the rake distributions. We thus didn't allow the rigidity value to vary during the inversion, which is possible only in the joint inversion of tsunami and geodetic data. The target model (Fig. 3, left panel) we used to generate a synthetic dataset of horizontal displacements at the GPS stations is the same as in the checkerboard test with the tsunami data (Fig. 2, left panel). Of course, the static GPS measurements are insensitive to the rupture velocity. We corrupted both North and East components of each synthetic GPS data point by adding a normally distributed random value, with a variance equal to the square of the error on the real data.

The checkerboard test in the case of the geodetic data has given a negative result (right panel Fig. 3 and Tab. 5, cols. 3-4). Despite of the almost perfect agreement between the synthetic and the inverted GPS vectors, the checkerboard pattern of the slip distribution is totally missed. Only the rake distribution is quite well recovered, with exception of the northernmost stretch, where the difference between target and inverted values is 20°. We repeated the test even with a clean dataset, i.e. without noise added to the synthetic data, and obtained comparably loose results. On one side this supports the choice of inverting the rake on a broader spatial scale than that of the single subfaults, as already done for the tsunami data. On the other side though, because the cost function of the inverted model has a relatively low value (i.e. the synthetic and the inverted horizontal displacements are very similar), it is likely that the problem is ill conditioned and the solution is not unique. In other words, given the present geodetic data distribution, it is impossible to constrain the slip distribution at the scale of the single subfault.

We then repeated the checkerboard test with bigger patches of slip in the target model (Figure 4, left panel). This time we divided the fault into 3 broader groups of subfaults, having the same spatial scale of the rake distribution. So we imparted 5 meters of slip and a rake of 90° to the southernmost patch, 15 meters and 130° to the intermediate, 5 meters and 90° to the northernmost. We added noise as before to the synthetic dataset.

In this case we have been able to recover the target pattern fairly well, both in terms of slip and rake, as can be seen in figure 4 (and Table 5, cols. 6-7). This confirms that the geodetic dataset has a lower spatial resolution than the tsunami dataset, as far as

the slip distribution is concerned. Additionally, we noticed that the inversion performed better in the southernmost and middle part of the source, whilst both inverted slip and rake values are in comparison farther from the target values in the northernmost stretch of the source. The geodetic data then constrain the source process particularly well south of about 9°N.

The above results are consistent with the features of our geodetic dataset, in which the near-field stations have not been included for the reasons discussed above, so that it cannot be sensitive to detailed small-scale source structure [cf. Chlieh et al., 2007]. Nevertheless, the far-field geodetic dataset can contribute to the inference of the seismic moment on a broader scale, and consequently, in the joint inversion with the tsunami data, to the rigidity inference on the same scale.

Joint inversion of tsunami and geodetic data: checkerboard test

The last checkerboard test we performed is a joint inversion of the whole dataset of this study, i.e. the tide-gages, the satellites and the geodetic data.

The setup of the target source (Figure 5, left panel) is the same as in the case of the tsunami dataset. We moreover assigned two different rigidity values, 30 GPa to the group of the 8 southernmost subfaults, and 10 GPa to the group of the remainder 10 subfaults, which are those north of about 6°N (gray ellipses of Figure 5, left panel). Similarly to what we have done before, we verified with some preliminary checkerboard tests (not shown), performed on synthetic sources with rigidity varying at a finer scale, that two rigidity values on quite broad zones is in this case very close to our resolution limit.

The results of the checkerboard test are satisfactory in the case of the joint inversion (right panel in Fig. 5 and Tab. 5, cols.8-9). The tsunami and geodetic datasets combined are then in principle able to constrain both the source process and the source zone rigidity (even if on a broader scale). In particular, the test demonstrated that we have got rid of the intrinsic trade off between slip and rigidity implied by eq. (12), likely because the slip distribution is well constrained by the tsunami dataset. The checkerboard pattern of the slip distribution is in fact very well reproduced, and the slip values have a maximum difference to the target ones of 2 meters. The rake values are exactly recovered almost everywhere, with exception of the central part, where there is a slight difference (5°) between target and inverted values. The rupture velocity distribution is exactly estimated, as well as the rigidity values.

Joint inversion of tsunami and geodetic data: the Sumatra 2004 earthquake

We used the setup of the checkerboard test described in the previous section to retrieve the source process of the December 2004 Sumatra earthquake, by means of a joint inversion of the tsunami and geodetic datasets.

Timing corrections of the Green's functions for Ranong, Krabi, Trang, Tarutao, Visakapatnam, Paradip, and Tuticorin were made, because we observed at these stations systematic differences between recorded and simulated phases. Relatively low resolution and uncertain nearshore bathymetry could have lead to inaccurate calculated travel times. In the present case, however, we verified that the positions of the slip patches, as well as the inverted rupture velocity, are only slightly dependent on the travel time adjustments.

The best model results are shown in Figure 6, left panel. The numerical values of each of the inverted parameters are listed in Table 6, columns 1 and 2.

The best source model we estimated for the 2004 earthquake features the maximum slip concentration in a broad patch around the epicenter and South of 6°N. In this zone there are 4 subfaults with slip values greater than 20 meters, and with a peak value of 34 meters. The rake in this patch is 95°. Further to this southernmost and biggest patch of slip, there are two northernmost smaller slip patches. The first one is centered at about 8°N with slip ranging from 12 to 18 meters and a rake of 95°. A third slip concentration is seen at depth – 10 to 36 km – below the Andaman islands (11 to 14°N), with slip between 6 and 8 meters, and rake 135°.

Our model features a rupture that propagates at a velocity that is 3.25 km/sec in the deeper southernmost segment (up to about 6°N), before slowing down to 2 km/sec in the northernmost and deeper part of the source. This corresponds to a total rupture duration of about 10 minutes. In the shallower southernmost segment the ruptures instead propagates slower from the beginning, at 2 km/s, and then much slower (0.5 km/s) in the northernmost shallower segment. This corresponds to a total rupture duration of 20 minutes, if one considers a front traveling along the shallower part and stopping at about 9-10°N. However, the rupture velocity cannot be well constrained here, for there is only one subfault slipping significantly, and then the slip goes rapidly to almost zero in the next subfault. This large uncertainty is highlighted by a question mark attached to the velocity value in Figure 6.

We estimated a rigidity value of 20 GPa for the source portion south of 6°N. This has to be considered as an average rigidity of the layer spanning from the surface down to

36 km of depth. Conversely, for the northernmost portion of the source, we estimated a rigidity value of 30 GPa. The latter has to be associated mostly to the deeper part of the source zone – 10 to 36 km – because, as already noticed, almost all the slip occurs on the deeper subfaults at North, with the exception of only one shallow subfault. Using these values for the rigidity, the seismic moment associated to our best solution is $6.63 \cdot 10^{22}$ Nm, corresponding to a magnitude Mw=9.15.

The errors on the model parameters are estimated, following *Piatanesi and Lorito* [2007], by means of an *a-posteriori* analysis of the ensemble of the models explored during the search for the best model. We here used only a subset of the explored models, i.e. we constructed the ensemble with only those models having a cost function exceeding by 1% the minimum value reached during the inversion. We first calculated the average model for each of the parameters, and then estimated the errors as the weighted standard deviation of each parameter. We used as a weighting function the inverse of the cost function. Both the average model and the associated errors are reported in Table 6, columns 3 and 4. The average source model is reported in Figure 6, right panel. The parameter values vary smoother along the average model than they did in the best model. For example, the rake changes more "gently" from 94° to 125°, passing through 104° in the middle of the source. Also, in the average model, the slip maxima in the southern portion of the source are lower than that of the best model, and the slip value never vanishes. This model is constructed by averaging all models featuring a low cost function, then having a significant probability of being good source models. Then, the average model, along with its associated errors, may indicate that the best model is eventually "overfitting" the data, so being a measure of how much epistemic and experimental errors are mapped into the retrieved source models. This may be the case, for example, when the best and average models are very different, or when the uncertainties are very large.

The comparison between the experimental datasets, and the synthetic ones generated with the best source model, is shown in Fig. 7. The simultaneous agreement of the tsunami waveforms at the tide-gages, the waveforms recorded by satellites, and the geodetic measurements with their synthetic counterparts is noticeable, particularly if one takes into account the intrinsic uncertainties in modeling, and the experimental dataset inhomogeneity. The comparison between the data and the predictions of the average model (Fig. 8) is only slightly worst than that found with the best model. This indicates that the fit between data and synthetics is still acceptable, in the range

defined by the comparison between Fig. 7 and 8, or by the errors listed in Table 6. Such variations are then likely to give a correct idea of the uncertainties associated to our source model.

5. Discussion

We found a slip distribution featuring most of the earthquake energy released around the Northern end of Sumatra, and further releases of slip through the Nicobar Islands and up to the Andaman Islands, with an overall length of the rupture of at least 1300 km. The magnitude Mw=9.15 we retrieved is consistent with previous estimations based on data of different nature [*Stein and Okal*, 2005; *Chlieh et al.*, 2007].

The presence of, at least, the two southernmost slip patches is a persistent feature of various models, as for example that of *Fujii and Satake* [2007], obtained by means of a joint inversion of tide-gage and satellite data, or the model proposed by *Pietrzak et al.* [2007], who combine GPS and coral reefs data.

In the present case, however, the slip in the best model is nearly zero in two of the southernmost subfaults near to the epicenter (namely subfaults 1 deep and 2 shallow, Table 6), while it is larger at the same places in the average model. This emphasizes the presence of a possible epistemic source of error due to the size of the subfaults. Nevertheless our source produces maximum water elevation values consistent with the maximum measured runup, which is around 30 meters in North-western Aceh [*Borrero*, 2005; *Tsuji et al.*, 2005; *Jaffe et al.*, 2006]. However, we do not expect to reproduce the details of the 2004 tsunami in the very near field, as we inverted for the entire source spanning about 1500 km and using far-field data [cf. *Geist et al.*, 2007]. Smaller subfaults, along with the constraints posed by near-field data such as the runup measurements in western Aceh, would help to better constrain the slip distribution for the 2004 earthquake at a finer spatial scale.

The third, deeper, and northernmost patch of slip is present in some recent models, as for example those presented by *Hoechner et al.* [2008], based on geodetic data, and *Sladen and Hébert* [2008], who pointed out that the relatively moderate tsunami observed at Andaman Islands may well be explained by the depth of the nearby patch.

The rake of the model rotates counter-clockwise as the rupture propagates northward, consistently to previous results [e.g. *Lay et al.,* 2005; *Subarya et al.*, 2006; *Banerjee et*

al., 2007], and is also consistent with the more oblique plates' convergence to the North.

Our model is characterized by a rupture that slows down in the northernmost segment of the source. The velocity of propagation of the rupture front has been decreasing, according to different investigators [*Bilham,* 2005; *Menke et al.*, 2006], while the rupture itself was proceeding northward. But we moreover inferred a slower rupture velocity for the shallower than for the deeper part of the southernmost source segment. The above corresponds to a total rupture duration of about 10 minutes. We find also an indication of a possibly slow rupture at about 8-9°N in the shallower part of the source, lasting up to about 20 minutes after the earthquake initiation. *Stein and Okal* [2005], first indicated the possibility of slow slip in the northern part of the source, and successively *Seno and Hirata* [2007] confirmed this finding, with a determination of the rupture velocity similar to what we found here. Nevertheless, others concluded that a slow slip component was not present or not necessary to explain the observations [Bilek, 2007; Chlieh et al., 2007; Fujii and Satake, 2007]. However, this feature is not completely constrained by our inversion, due to the limited spatial extent of the corresponding slip patch.

The model rigidity values, that we here derive for the first time self-consistently in a joint inversion are lower than the PREM average values at the corresponding depths. This supports previous findings concerning the Sumatra 2004 earthquake source zone [*Bilek*, 2007], as well as other subduction zones [*Bilek and Lay,* 1998; *Bilek and Lay,* 1999]. Such results are derived by assuming constant stress drop and the rigidity being inversely proportional to the rupture duration; conversely, in the present study we didn't make *a-priori* assumptions in this respect.

Moreover, we found that, in the southernmost source segment, the rupture is slower near to the Earth's surface than it is at depth. This is likely to be a consequence of the rigidity increase with depth, for the rupture velocity is generally found to scale with shear wave velocity [*Bilek and Lay,* 1998], which by definition is proportional to the rigidity itself. In other words, the rupture should propagate faster in the deeper part of the source, and this is what we found with our inversion. However, as we couldn't resolve properly the variations of the rigidity with depth, we couldn't independently establish such a detailed correlation between these two parameters.

As about the along-strike variation of the fault properties, we observe that the rupture is slowing down and deepening in the northern part of the source. Thus the rigidity

value we estimated (≤30GPa) is representative of the deeper portion of the source (10-36 km depth). This very low rigidity value, along with the relatively low velocity with respect to southernmost part of the source, is likely to be explained by the changes in the properties of the subducted slab indicated by *Kennett and Cummins* [2005], who find zones of relatively low ratios of shear velocities to bulk ratio in the northern part of the source, and by the presence of a low seismic velocity material under the Andaman Sea [*Shapiro et al.* 2008]. Nevertheless, *Bilek* [2007] found no evidence of frictional conditions changes at North, even if basing on a relatively scarce dataset of seismic events in the Northern Andaman segment.

Finally, we used our source model to predict ground displacements in the near-field, where some geodetic campaign data exists [*Gahalaut et al.*, 2006; *Jade et al.*, 2005; *Subarya et al.*, 2006], that have been excluded from the inversion dataset for the reasons discussed above. We observe (Fig. 9) that our model clearly under predicts the observed displacement [*Banerjee et al.* (2007), tables S3 and S4 of the electronic supplement] along the Andaman and Nicobar Island. A slight deficit of the predicted horizontal deformation is present in the Northern part of Sumatra (between 5° and 6°N). This would support a significant presence of afterslip/postseimic deformation in the campaign measurements, as suggested by Chlieh et al. [2007]., As the tsunami data used in the inversion (tide-gage plus satellite) are likely to offer a good control on the slip distribution in the Northern part of the source, we consider this result quite robust, at least in the framework of 1D (layered Earth) modeling. However, as most of the data have been measured just over the island arc, they are likely to be sensible to the 3D structure of the subduction zone [*Masterlark and Hughes*, 2008], and a more sophisticated model would be necessary to settle the question.

6. Conclusions

We presented a joint inversion of tide-gage, satellite altimetry, and far-field GPS data, conducted to infer the source process and the source zone rigidity of the December 2004 Sumatra-Andaman earthquake. We inverted four free parameters: slip, rake, rupture velocity, and source rigidity.

We first performed a series of synthetic checkerboard tests. We found that the tsunami data are able to constrain the slip distribution at the spatial scale of the single subfault, whilst the far-field geodetic data may constrain the slip distribution only on a broader

scale. The rake, velocity and rigidity are all constrained by the present dataset on a broader scale than the slip.

The joint inversion of the three datasets in the case of the Sumatran 2004 earthquake has confirmed results of previous inversions, with a rupture characterized by three main slip patches, among which the broadest is around the epicenter and with slip peaking at ~30 meters.

In addition to previously published papers, we found that the rupture propagated slower in the shallower than in the deeper part of the source, consistently with the fact that the rigidity should increase with depth. The rupture propagated slower also while releasing the two northernmost slip patches, where progressively less rigid material is likely to exist. The rake rotated counter-clockwise at North, according to the relative direction of the plates' convergence.

We also determined self-consistently the average rigidity of the source zone on a broad scale, which resulted significantly lower than the PREM values at the corresponding depths. The estimation of the source zone rigidity is important since it may play a significant role in the tsunami generation and, particularly for slow earthquakes, a low rigidity value is sometimes necessary to explain how a relatively low seismic moment earthquake may generate significant tsunamis [*Geist and Bilek,* 2001]. In the case of the Sumatran earthquake source, a lower-than-the-average rigidity could also be the key to explain why inversions that rely on slip-based source models [*Fujii and Satake*, 2007; *Piatanesi and Lorito*, 2007; *Pietrzak et al.*, 2007; *Hoechner et al.*, 2008; *Sladen and Hébert*, 2008] give generally greater maximum slip values (~30 meters, as in the present study) than those using moment-based models [*Ammon et al.*, 2005; *Chlieh et al.*, 2007; *Rhie et al.*, 2007]. The latter generally impose PREM like-values to deduce the slip through the rigidity. Conversely, both kind of methods give comparable moment and consequently magnitude estimates.

As a side effect of our investigation, we found that near-field (campaign) GPS data are likely to contain first order non-coseismic signals. This prevented us from including such data into the inversion, and unfortunately posed an upper bound to the resolution on the inference of the rigidity distribution. For the same reason, we could not establish a direct correlation between rupture velocity and source rigidity at a finer scale. In the future, e.g. when and where reliable near-field geodetic data will be available after a large subduction zone earthquake, it will be possible to apply – and further validate – the approach we proposed here. This will be more robust if

including a 3D modeling better representing the real structural complexity of a subduction zone.

Nevertheless, the general consistence between our source model with previous studies supports the validity of the method we proposed for the rigidity estimation from the joint inversion of geodetic and tsunami data, and will hopefully stimulate further research.

Acknowledgments

We gratefully acknowledge the contribution of A. Mautone at SISMOS/INGV, who scanned the nautical charts. Comments and suggestions by two anonymous reviewers have greatly improved this manuscript.

Some figures have been produced with Generic Mapping Tools software (Wessel and Smith, 1998). Natural Neighbours interpolation software was provided by Pavel Sakov and is available at URL: http://geog-pc40.ulb.ac.be/grass/nnbathy/ (last accessed March 2009).

References

Ablain, M., J. Dorandeu, P.-Y. Le Traon, and A. Sladen (2006), High resolution altimetry reveals new characteristics of the December 2004 Indian Ocean tsunami, *Geophys. Res. Lett.*, *33*, L21602, doi:10.1029/2006GL027533.

Ammon, C. J., C. Ji, H.K. Thio, D. Robinson, S. Ni, V. Hjorleifsdottir, H. Kanamori, T. Lay, S. Das, D. Helmberger, G. Ichinose, J. Polet and D. Wald (2005), Rupture process of the 2004 Sumatra-Andaman earthquake, *Science*, *308*, 1133-1139, doi:10.1126/science.1112260.

Amoruso, A, L. Crescentini, and C. Fidani (2004), Effects of crustal layering on source parameter inversion from coseismic geodetic data, *Geophys. J. Int., 159*, 353-364, doi:10.1111/j.1365-246X.2004.02389.x.

Banerjee, P., F.F. Pollitz and R. Bürgmann (2005), The size and duration of the Sumatra-Andaman earthquake from far-field static offsets, *Science*, *308*, 1769-1772, doi:10.1126/science.1113746.

Banerjee P., F.F. Pollitz, B. Nagarajan, and R. Bürgmann (2007), Coseismic Slip Distributions of the 26 December 2004 Sumatra–Andaman and 28 March 2005 Nias Earthquakes from GPS Static Offsets, *Bull. Seismol. Soc. Am., 97*(1A), S86–S102, doi:10.1785/0120050609.

Bilek, S.L. (2007), Using Earthquake Source Durations along the Sumatra–Andaman Subduction System to Examine Fault-Zone Variations, *Bull. Seismol. Soc. Am., 97*(1A), S62–S70, doi: 10.1785/0120050622.

Bilek, S.L., and T. Lay (1998), Variation of Interplate Fault Zone Properties with Depth in the Japan Subduction Zone, *Science, 281*, 1175-1178, doi:10.1126/science.281.5380.1175.

Bilek, S.L., and T. Lay (1999), Rigidity variations with depth along interplate megathrust faults in subduction zones, *Nature, 400*, 443-446, doi:10.1038/22739.

Bilek, S.L., K. Satake, and K. Sieh (2007), Introduction to the special issue on the 2004 Sumatra-Andaman earthquake and the Indian Ocean tsunami, *Bull. Seismol. Soc. Am.*, *97*, S1 – S5, doi:10.1785/0120050633.

Bilham, R. (2005), A flying start, then a slow slip, *Science*, *308*, 1126-1127, doi:10.1126/science.1113363.

Borrero, J. C. (2005), Field survey of northern Sumatra and Banda Aceh, Indonesia after the tsunami and earthquake of 26 December 2004, *Seism. Res. Lett.*, *76*, 312–320.

Boschi, E., E. Casarotti, R. Devoti, D. Melini, G. Pietrantonio and F. Riguzzi (2006), Coseismic deformation induced by the Sumatra earthquake, *J. Geodyn., 42*, 52-62.

Boschi, L., A. Piersanti and G. Spada (2000), Global postseismic deformation: deep earthquakes, *J. Geophys. Res., 105*, 631-652, doi:10.1029/1999JB900278.

Catherine, J.K., V.K. Gahalaut, and V.K. Sahu (2005), Constraints on rupture of the December 26, 2004, Sumatra earthquake from far-field GPS observations, *Earth Plan. Sc. Lett., 237,* 673-679, doi:10.1016/j.epsl.2005.07.012.

Chlieh, M. et al. (2007), Coseismic slip and afterslip of the Great (Mw9.15) Sumatra-Andaman Earthquake of 2004, *Bull. Seism. Soc. Am., 97*, S152–S173, doi:10.1785/0120050631.

Dow , J.M., R.E. Neilan, and G. Gendt (2005), The International GPS Service (IGS): Celebrating the 10th Anniversary and Looking to the Next Decade, *Adv. Space Res.* 36 vol. 36, no. 3, pp. 320-326, doi:10.1016/j.asr.2005.05.125.

Dragani, W.C., E.E. D'Onofrio, W. Grismeyera, and M.E. Fiore (2006), Tide gauge observations of the Indian ocean tsunami, December 26, 2004, in Buenos Aires coastal waters, Argentina, *Cont. Shelf. Res., 26*, 1543-1550, doi:10.1016/j.csr.2006.03.002.

Dziewonski, A. M., and D. L. Anderson (1981), Preliminary reference Earth model (PREM), *Phys. Earth Planet. Interiors, 25*, 297–356, doi:10.1016/0031-9201(81)90046-7.

Fujii, Y., and K. Satake (2006), Source of the July 2006 West Java tsunami estimated from tide gauge records, Geophys. Res. Lett., 33, L24317, doi:10.1029/2006GL028049.

Fujii, Y., and K. Satake (2007), Tsunami source of 2004 Sumatra-Andaman earthquake inferred from tide-gauges and satellite data, *Bull. Seismol. Soc. Am.*, *97*(1A), S192-S207, doi:10.1785/0120050613.

Fujii, Y., and K. Satake (2008), Tsunami Sources of the November 2006 and January 2007 Great Kuril Earthquakes, *Bull. Seismol. Soc. Am.*, *98*(3), 1559-1571, doi:10.1785/0120070221

Gahalaut, V.K., B. Nagarajan, J.K. Catherine, and S. Kumar (2006), Constraints on 2004 Sumatra–Andaman earthquake rupture from GPS measurements in Andaman–Nicobar Islands, *Earth Plan. Sc. Lett., 242,* 365-374, doi:10.1016/j.epsl.2005.11.051.

Geist, E.L. (1999), Local tsunamis and earthquake source parameters, *Advances in Geophysics*, *39*, 117-209.

Geist, E.L., and S.L. Bilek (2001), Effect of depth-dependent shear modulus on tsunami generation along subduction zones, *Geophys. Res. Lett.*, *28*(7), 1315-1318.

Geist, E.L., V.V. Titov, D. Arcas, F.P. Pollitz, and S.L. Bilek (2007), Implications of the December 26, 2004 Sumatra-Andaman earthquake on tsunami forecast and assessment models for great subduction zone earthquakes, *Bull. Seismol. Soc. Am.*, *97*(1A), S249-S270, doi:10.1785/0120050619.

GGCI. Geodesy and Geodinamics Center of Indonesia.

GLOSS. Global Sea Level Observing System, JCOMM/WMO/IOC UNESCO.

Gower, J. F. (2005), Jason 1 detects December 26, 2004 tsunami, *Eos. Transactions American Geophysical Union*, *86*, 37-38.

Grilli, S. T., M. Ioualalen, J. Asavanant, F. Shi, J. T. Kirby, and P. Watts (2007), Source constraints and model simulation of the December 26, 2004 Indian Ocean tsunami, *J. Waterw. Port Coastal Ocean Eng., 133*(6), 414-428, doi: 10.1061/(ASCE)0733-950X(2007)133:6(414).

Gu, Y. J. (2006), Preface to special issue, *Surv. Geophys., 27*, 601 – 602, doi:10.1007/s10712-006-9014-3.

Hashimoto, M., N. Choosakul, M. Hashizume, S. Takemoto, H. Takiguchi, Y. Fukuda, and K. Fujimori (2006), Crustal deformations associated with the great Sumatra-Andaman earthquake deduced from countinuous GPS observation, *Earth Planets Space*, *58*, 203-209.

HDRTN, Hydrographic Department, Royal Thai Navy, Thailand.

Hébert, H., A. Sladen, and F. Schindelé (2007), Numerical Modeling of the Great 2004 Indian Ocean Tsunami: Focus on the Mascarene Islands, *Bull. Seismol. Soc. Am.*, *97*(1A), S 08–S222, doi: 10.1785/0120050611.

Hirata, K., K. Satake, Y. Tanioka, T. Kuragano, Y. Hasegawa, Y. Hayashi and N. Hamada (2006), The 2004 Indian ocean tsunami: tsunami source model from satellite altimetry, *Earth Planets Space*, *58*, 195-201.

Hoechner A., A. Y. Babeyko, S. V. Sobolev (2008), Enhanced GPS inversion technique applied to the 2004 Sumatra earthquake and tsunami, *Geophys. Res. Lett.*, *35*, L08310, doi:10.1029/2007GL033133.

Ichinose G., P. Somerville, H.K. Thio, R. Graves, and D. O'Connell (2007), Rupture process of the 1964 Prince William Sound, Alaska, earthquake from the combined inversion of seismic, tsunami, and geodetic data, *J. Geophys. Res., 112,* B07306, doi:10.1029/2006JB004728.

IGS, International GNSS Service, http://igscb.jpl.nasa.gov/ (last accessed March 2009).

Ioualalen, M, J. Asavanant, N. Kaewbanjak, S.T. Grilli, J.T. Kirby, and P. Watts (2007), Modeling the 26 December 2004 Indian Ocean tsunami: Case study of impact in Thailand, *J. Geophys. Res., 112,* C07024, doi:10.1029/2006JC003850.

Jade, S., M. Ananda, P. Kumar, and S. Banerjee (2005), Co-seismic and post-seismic displacements in Andaman and Nicobar islands from GPS measurements, *Curr. Sci.,* 88, 1980–1984.

Jaffe, B. E., et al. (2006), Northwest Sumatra and Offshore Islands Field Survey after the December 2004 Indian Ocean tsunami, *Earthquake Spectra*, *22*, S105–S135.

Ji, C., D.J. Wald, D.V. Helmberger (2002), Source description of the 1999 Hector Mine, California earthquake; Part I: wavelet domain inversion theory and resolution analysis, *Bull. Seismol. Soc. Am.*, *92*, 4, 1192-1207,doi:10.1785/0120000916.

Joseph A., J.T. Odametey, E.K. Nkebi, A. Pereira, R.G. Prabhudesai, P. Mehra, A.B. Rabinovich, V. Kumar, S. Prabhu- desai and P. Woodworth (2006), The 26 December 2004 Sumatra tsunami recorded on the coast of West Africa, *Afr. J. Mar. Sci., 28*(3&4), 705–712.

Kennett, B.L.N., and P.R. Cummins (2005), The relationship of the seismic source and subduction zone structure for the 2004 December 26 Sumatra-Andaman earthquake, *Earth Plan. Sc. Lett., 239*, 1-8, doi:10.1016/j.epsl.2005.08.015.

Lay, T. et al. (2005), The great Sumatra-Andaman earthquake of 26 December 2004, *Science*, *308*, 1127-1133, doi:10.1126/science.1112250.

Lorito, S., A. Piatanesi, and A. Lomax (2008a), Rupture Process of the 18 April 1906 California Earthquake from Near-Field Tsunami Waveform Inversion, *Bull. Seismol. Soc. Am., 98*(2), 832–845, doi: 10.1785/0120060412.

Lorito, S., F. Romano, A. Piatanesi, and E. Boschi (2008b), Source process of the September 12, 2007, Mw 8.4 southern Sumatra earthquake from tsunami tide gauge record inversion, *Geophys. Res. Lett.*, *35*, L02310, doi:10.1029/2007GL032661.

Mader, C. L. (2001), *Numerical Modeling of Water Waves*, Los Alamos Ser. 341 Basic Appl. Sci., vol. 8, CRC Press, Boca Raton, Fla.

Marks, K.M., and W.H.F. Smith (2006), An evaluation of publicly available bathymetry grids, *Mar. Geophys. Res., 27*, 19-34.

Masterlark, T., and K.L. Hughes (2008) The next generation of deformation models for the 2004 M9 Sumatra-Andaman Earthquake, *Geophys. Res. Lett, 35*, L19310, doi:10.1029/2008GL035198.

Megna, A., S. Barba, S. Santini, and M. Dragoni (2008), Effects of geological complexities on coseismic displacement: hints from 2D numerical modelling, *Terra Nova*, *20*(3), 173-179, doi:10.1111/j.1365-3121.2008.00800.x.

Menke, W., H. Abend, D. Bach, K. Newman, and V. Levin (2006), Review of the source characteristics of the Great Sumatra–Andaman Islands earthquake of 2004, *Surv Geophys, 27*, 603–613, doi: 10.1007/s10712-006-9013-4.

Merrifield, M.A. et al. (2005), Tide gauge observations of the Indian Ocean tsunami, December 26, 2004, *Geophys. Res. Lett.*, *32*, L09603, doi:10.1029/2005GL022610.

Nagarajan, B., I. Suresh, D. Sundar, R. Sharma, A.K. Lal, S. Neetu, S.S.C. Shenoi, S.R Shetye, and D. Shankar (2006), The great tsunami of 26 December 2004: a description based on tide-gauge data from the Indian subcontinent and surrounding areas, *Earth Planet Space, 58*, 211–215.

NIO. National Institute of Oceanography, Goa, India.

Obura, D. (2006), Impacts of the 26 December 2004 tsunami in Eastern Africa, *Ocean Coast. Manage.*, *49*, 873–888, doi:10.1016/j.ocecoaman.2006.08.004.

Okada, Y. (1992), Internal deformation due to shear and tensile faults in a half-space, *Bull. Seismol. Soc. Am.*, *82*, 1018-1040.

Piatanesi, A., A. Cirella, P. Spudich and M. Cocco (2007) : A global search inversion for earthquake kinematic rupture history : application to the 2000 Western Tottori, Japan earthquake *J. Geophys. Res.* Vol. 112, No. B7, B07314, doi:10.1029/2006JB004821.

Piatanesi, A., and S. Lorito (2007), Rupture Process of the 2004 Sumatra–Andaman Earthquake from Tsunami Waveform Inversion, *Bull. Seismol. Soc. Am.*, *97*(1A), S223-S231, doi: 10.1785/0120050627.

Piersanti, A., G. Spada, R. Sabadini, and M. Bonafede (1995), Global post-seismic deformation, *Geophys. J.Int., 120,* 544–566, doi:10.1111/j.1365-246X.1995.tb01838.x.

Pietrzak, J., A. Socquet, D. Ham, W. Simon, C. Vigny, R. J. Labeur, E. Schrama, G. Stelling, and D. Vatvani (2007), Defining the source region of the Indian Ocean Tsunami from GPS, altimeters, tide gauges and tsunami models, *Earth Planet. Sci. Lett., 261*, 49-64, doi:10.1016/j.epsl.2007.06.002.

PO.DAAC. Physical Oceanography Distributed Active Archive Center, Jet Propulsion Laboratory Caltech/NASA, USA.

Rabinovich A.B., R.E. Thomson, and F.E. Stephenson (2006), The Sumatra tsunami of 26 December 2004 as observed in the North Pacific and North Atlantic oceans, *Surv. Geophys., 27*, 647–677, doi:10.1007/s10712-006-9000-9.

Rabinovich A.B., and R.E. Thomson (2007), The 26 December 2004 Sumatra Tsunami: Analysis of Tide Gauge Data from the World Ocean Part 1. Indian Ocean and South Africa, *Pure Appl. Geophys., 164*, 261–308, doi:10.1007/s00024-006-0164-5.

Rhie, J., D. Dreger, R. Bürgmann, and B. Romanowicz (2007), Slip of the 2004 Sumatra–Andaman Earthquake from Joint Inversion of Long-Period Global Seismic Waveforms and GPS Static Offsets, *Bull. Seismol. Soc. Am.*, *97*(1A), S115-S127, doi: 10.1785/0120050620.

Rothman, D. (1986), Automatic estimation of large residual statics corrections, *Geophysics*, *51*, 332-346.

Sambridge M., J. Braun and H. McQueen (1995), Geophysical parameterization and interpolation of irregular data using natural neighbours, *Geophys. J.Int.*, *122*, 837-857, doi:10.1111/j.1365-246X.1995.tb06841.x

Satake, K. , E.A. Okal, and J. C. Borrero (2007), Tsunami and its Hazard in the Indian and Pacific Oceans: Introduction, *Pure Appl. Geophys., 154*(2-3), 249-259, doi: 10.1007/s00024-006-0172-5.

Sen, M. and Stoffa P.L. (1991), Nonlinear one-dimensional seismic waveform inversion using simulated annealing, *Geophysics*, *56*, 1624-1638.

Seno, T. and K. Hirata (2007), Did the 2004 Sumatra–Andaman Earthquake Involve a Component of Tsunami Earthquakes? *Bull. Seismol. Soc. Am.*, *97*(1A), S296 - S306, doi: 10.1785/0120050615.

Shapiro, N.M., M.H. Ritzwoller, and E.R. Engdahl (2008) Structural context of the great Sumatra-Andaman Islands earthquake, *Geophys. Res. Lett.*, *35*, L05301, doi:10.1029/2008GL033381.

Sindhu B, I. Suresh, A.S. Unnikrishnan, N.V. Bhatkar, S. Neetu, and G.S. Michael (2007), Improved bathymetric datasets for the shallow water regions in the Indian Ocean, *J. Earth Syst. Sci.*, *116*(3), 261-274, doi: 10.1007/s12040-007-0025-3.

Sladen A., and H. Hébert (2008), On the use of satellite altimetry to infer the earthquake rupture, characteristics: application to the 2004 Sumatra event, *Geophys. J.Int.*, *172*, 707–714, doi: 10.1111/j.1365-246X.2007.03669.x

Smith, W. H. F., and P. Wessel (1990), Gridding with continuous curvature splines in tension, *Geophysics*, *55*, 293−305.

Smith, W.H.F., R. Scharroo, V. V. Titov, D. Arcas , and B. K. Arbic (2005), Satellite Altimeters Measure Tsunami, *Oceanography, 18*, 11-13.

Soldati, G., A. Piersanti, A., and E. Boschi (1998), Global postseismic gravity changes of a viscoelastic Earth*, J. Geophys. Res., 103,* 29,867-29,885, doi:10.1029/98JB02793.

Spudich, P. and D.P. Miller (1990), Seismic site effects and the spatial interpolation of earthquake seismograms: results using aftershocks of the 1986 North Palm Springs, California earthquake, *Bull. Seismol. Soc. Am., 80*, 1504-1532.

Stein, S., and E. A. Okal (2005), Speed and size of the Sumatra earthquake, *Nature*, *434*, 581-582, doi:10.1038/434581a.

Subarya, C., M. Chlieh, L. Prawirodirdjo, J-P. Avouac, Y. Boch, K. Sieh, A.J. Meltzmer, D.H. Natawidjaja and R. McCaffrey (2006), Plate-boundary deformation associated with the great Sumatra-Andaman earthquake, *Nature, 440,* 46-51, doi:10.1038/nature04522.

SuGAr, Sumatran GPS Array of Caltech's Tectonics Observatory, http://www.tectonics.caltech.edu/sumatra/data.html (last accessed March 2009).

Tanioka, Y., E.L. Geist, and N.T. Puspito (2006a), Preface to special issue ''The 2004 Great Sumatra Earthquake and Tsunami'', *Earth Planets Space 58(2),* 111.

Tanioka, Y., Yudhicara, T. Kususose, S. Kathiroli, Y. Nishimura, S.I. Iwasaki, and K. Satake (2006b), Rupture process of the 2004 great Sumatra-Andaman earthquake estimated from tsunami waveforms, *Earth Planet Space, 58*, 203-209.

Tinti, S., and R. Tonini (2005), Analytical evolution of tsunamis induced by near-shore earthquakes on a constant-slope ocean, *J. Fluid Mech., 535*, 33–64, doi:10.1017/S0022112005004532.

Titov, V., A.B. Rabinovich, H.O. Mofjeld, R.E. Thomson, and F.I. González (2005), The Global Reach of the 26 December 2004 Sumatra Tsunami, *Science, 309*, 2045-2048, doi:10.1126/science/1114576.

Thomson R.E. , A.B. Rabinovich, and M.V. Krassovski (2007), Double jeopardy: Concurrent arrival of the 2004 Sumatra tsunami and storm-generated waves on the Atlantic coast of the United States and Canada, *Geophys. Res. Lett.*, *34*, L15607, doi:10.1029/2007GL030685.

Tsuji, Y., H. Matsutomi, Y. Tanioka, Y. Nishimura, T. Sakakiyama, T., Kamataki, Y. Murakami, A. Moore, and G. Gelfenbaum (2005), Distribution of the tsunami heights of the 2004 Sumatera tsunami in Banda Aceh measured by the Tsunami Survey Team, edited, University of Tokyo, http://www.eri.u-tokyo.ac.jp/namegaya/sumatera/surveylog/eindex.htm (last accessed March 2009).

Tsuji, Y., Y. Namegaya, H. Matsumoto, S.-I. Iwasaki, W. Kambua, M. Sriwichai and V. Meesuk (2006), The 2004 Indian tsunami in Thailand: tsunami height and tide-gauge records, *Earth Planet Space*, *58*, 223-232.

UHSLC. University of Hawaii Sea Level Center, USA.

Vigny, C., W.J.F. Simons, S. Abu, R. Bamphenyu, C. Satirapod, N. Choosakul, C. Subaraya, A. Soquet, K. Omar, H.Z. Abidin and B.A.C. Ambrosius (2005), GPS in SE Asia provides unforeseen insights on the 2004 megathrust earthquake Insight into the 2004 Sumatra-Andaman earthquake from GPS measurements in Southeast Asia, *Nature*, *436*, 201-206, doi:10.1038/nature03937.

Wang, R., F. L. Lorenzo, and F. Roth (2003). Computation of deformation induced by earthquakes in multi-layered elastic crust — FORTRAN programs EDGRN/EDCMP, *Comput. Geosci.*, *29*, 195–207.

Wessel, P., and W.H.F. Smith (1998), New, improved version of the Generic Mapping Tools released, *EOS Trans. AGU, 79*, 579.

Zhao, S., R.D. Müller, Y. Takahashi, and Y. Kaneda (2004), 3-D finite-element modelling of deformation and stress associated with faulting: effect of inhomogeneous crustal structures, *Geophys. J. Int., 157,* 629-644, doi:10.1111/j.1365-246X.2004.02200.x.

Tables

Table 1. Tide gage stations list.

Station	Lat	Lon	a/d (*)	Sampling (min)	Weight
Krabi	08.05 N	98.92 E	a	5	0.75
Tarutao	06.70 N	99.65 E	a	5	0.75
Ranong	09.95 N	98.58 E	a	5	0.75
Ta pao	07.77 N	98.42 E	a	5	0.75
Sibolga	01.75 N	98.77 E	d	10	0.5
Diego garcia	07.28 S	72.40 E	d	6	0.75
Gan	00.68 S	73.15 E	d	4	1
Male	04.18 N	73.52 E	d	4	1
Hanimaadhoo	06.76 N	73.17 E	d	2	1
Visakhapatnam	17.68 N	83.28 E	d	5	0.75
Paradip	20.26 N	86.70 E	d	6	0.75
Chennai	13.10 N	80.30 E	d	5	0.75
Tuticorin	08.80 N	78.15 E	d	6	0.75

(*) a= analogical, d=digital

Table 2. Digitized charts list.

N°	Title	North	East	South	West	Scale
3	Chagos Archipelago	4.58S	72.83E	7.83S	70.65E	1:360000
400	Ujung Karang to Sibolga	4.17N	99.00E	1.22N	94.58E	1:500000
813	Colombo to Sangama Kanda Point	7.11N	82.17E	5.30N	78.93E	1:300000
814	The Sandheads - Paradip to Raimangal River	21.86N	89.34E	20.17N	86.58E	1:300000
825	Andaman Islands	15.33N	94.50E	10.03N	91.50E	1:500000
840	Little Andaman to Great Nicobar	10.83N	94.51E	6.25N	91.50E	1:500000
842	Chowra to Great Nicobar	8.59N	93.96E	6.74N	92.93E	1:175000
920	Diego Garcia	7.19S	72.50E	7.45S	72.35E	1:25000
1011	Addoo Atoll to North Huvadhoo Atoll	1.17N	74.00E	1.50S	72.20E	1:300000
1013	Mulaku Atoll to South Maalhosmadulu Atoll	5.33N	74.00E	2.67N	72.20E	1:300000
1014	South Maalhosmadulu Atoll to Ihavandhippolhu Atoll	7.45N	74.00E	4.80N	72.20E	1:300000
1509	Coondapoor to Vengurla	16.07N	74.75E	13.33N	72.95E	1:300000
1564	Sacrifice Rock to Coondapoor	14.02N	75.79E	11.25N	73.99E	1:300000
1565	Alleppey to Sacrifice Rock	11.75N	76.56E	8.97N	74.75E	1:300000
1566	Cape Comorin to Cochin	10.00N	77.58E	7.20N	75.78E	1:300000
1583	Little Basses Reef to Pulmoddai Roads	9.12N	82.47E	6.37N	80.67E	1:300000
1584	Trincomalee to Point Calimere	10.33N	81.67E	8.52N	78.88E	1:300000
1586	Pamban to Cape Comorin	9.50N	80.00E	7.73N	77.24E	1:300000
1587	Colombo to Cape Comorin	8.20N	80.00E	6.43N	77.24E	1:300000
2058	Puri to the Sandheads	21.22N	88.42E	19.55N	85.67E	1:300000
2060	Kalingapatnam to Puri	19.93N	86.77E	18.25N	84.00E	1:300000
2061	Kakinada to Kalingapatnam	18.52N	84.97E	16.82N	82.20E	1:300000
2062	False Divi Point to Kakinada	17.13N	83.17E	15.42N	80.17E	1:300000
2063	Madras to False Divi Point	15.83N	81.78E	12.92N	80.00E	1:300000
2067	Addoo Atoll	0.57S	73.27E	0.72S	73.04E	1:25000
2069	Point Calimere to Madras	13.17N	81.42E	10.08N	79.58E	1:300000
2777	Indira Point to Teluk Aru and Ujung Kareueng	6.83N	98.70E	3.90N	93.52E	1:500000
2779	Pulau Ilir to Pulau Nyamuk	1.37N	100.83E	1.50S	96.50E	1:500000
3052	Za Det Gyi Island to Mu Ko Similan	10.15N	98.67E	8.36N	97.50E	1:200000
3323	Male' Atoll	4.82N	73.88E	3.95N	73.17E	1:150000
3941	Mu Ko Similan to Ko Lanta Yai	8.56N	99.37E	7.39N	97.61E	1:200000
3942	Ko Lanta Yai to Ko Tarutao	7.60N	100.14E	6.43N	98.30E	1:200000
3943	Ko Tarutao to Pulau Pinang	6.59N	100.43E	5.45N	98.60E	1:200000

Table 3. Geodetic dataset used in this study. Data from *Banerjee et al.*, [2007] and references therein.

Lon	Lat	E_{offset}	N_{offset}	E_{sig}	N_{sig}	Site
°E	°N	mm	mm	mm	mm	
99.39	0.22	-4.22	-5.11	3.66	2.32	ABGS
100.28	6.45	-130.25	-33.76	9.14	4.05	ARAU
106.84	-6.49	0.06	-5.84	3.67	2.27	BAKO
77.51	13.03	11.18	-3.34	4.11	2.68	BAN2
78.6	30.8	0.89	-1.45	2.86	1.97	BHTW
85.8	20.3	7.22	-4.26	8.47	4.18	BHUB
100.61	13.67	-60.93	-42.55	4.26	2.61	BNKK
115.89	39.61	-4.6	-4.99	3.94	2.92	BJFS
98.97	18.77	-15.8	-24.9	4.89	2.96	CHMI
98.9	18.8	-14.04	-25.84	6.95	3.89	CMU
96.83	-12.19	4.63	-0.77	3.72	2.22	COCO
99.4	10.7	-127.39	-67.47	4.37	2.53	CPN
127.37	36.4	-2.34	-6.02	3.96	3.1	DAEJ
72.37	-7.27	6.73	-0.71	3.98	2.24	DGAR
78.55	17.42	6.8	-4.37	2.95	1.95	HYDE
77.57	13.02	12.34	-2.42	3	1.96	IISC
117.1	-20.98	-3.28	1.36	4.59	2.63	KARR
66.89	39.13	-1.53	-3.08	2.23	1.57	KIT3
100.8	13.7	-56.4	-44.26	5.1	3.08	KMI
103.14	5.32	-56.67	-5.59	7.69	4.12	KUAL
102.8	25.03	-4.66	-8.52	3.54	2.39	KUNM
91.1	29.66	-1.09	-2.76	4.45	2.87	LHAS
101.16	-2.29	5.53	-4.05	4.27	2.46	LNGG
80.9	26.9	0.1	-1.84	3.91	2.35	LUCK
101.09	-2.54	6.06	-5.93	4.37	2.47	MKMK
99.09	-1.33	2.85	-8.54	3.64	2.29	MSAI
76.3	32.2	1.76	0.61	3.26	2.01	NADI
99.27	-1.8	1.58	-7.94	3.99	2.36	NGNG
103.68	1.35	-14.62	1.65	3.22	2.22	NTUS
98.53	-0.03	-6.29	-0.69	18.19	4.73	PBAI
98.31	8.11	-239.3	-107.72	4.62	2.56	PHKT
121.08	14.64	-10.73	-5.49	3.89	2.55	PIMO
74.69	42.68	-4.32	2.93	2.59	1.89	POL2
100.4	-2.97	1.28	-7.23	4.31	2.42	PRKB
77.5	23.2	0.71	-3.58	4.1	2.34	RRLB
98.72	3.62	-132.52	-19.05	5.41	2.5	SAMP
91.9	25.6	-1.24	-2.45	4.43	2.68	SHL2
99.867	17.157	-30.4	-32.14	4.22	2.6	SIS2
127.05	37.28	-5.91	-3.02	4.17	3.28	SUWN
77	8.4	16.49	-1.86	10.07	3.76	TIR0
120.99	24.8	-10.39	-2.42	4.1	2.84	TNML
78	30.3	0.69	-1.11	2.74	1.9	WIH2
114.36	30.53	-6.02	-4.68	4.51	3.04	WUHN
101.52	3.77	-55.91	2.31	2.79	1.88	BEHR
113.07	3.26	-10.39	-6.17	5.18	2.32	BINT
116.04	5.91	-5.78	-0.21	4.84	2.2	KINA

103.35	3.83	-39.16	1.06	3.74	2.19	KUAN
115.25	5.28	-8.18	-2.7	4.58	2.1	LABU
119.91	-0.92	-1.18	0.13	4.21	1.75	PALP
121.2	31.1	-2.9	-0.38	5.11	4.84	SHAO
120.1	-0.71	1.51	0.75	5.09	2.15	TOBP
116.83	-1.27	-3.65	-0.51	4.71	1.92	UNO0
100.3	5.36	-115.13	-14.41	4.78	2.9	USMP
119.59	-0.87	-1.53	-0.98	4.29	1.8	WATP
103.64	1.57	-19.51	4.55	3.69	2.15	UTMJ
101.54	2.83	-45.01	3.47	3.93	2.45	BANT
101.96	4.86	-70.52	-2.37	4.58	3.03	GMUS
101.13	5.44	-90.92	-10.88	3.68	2.57	GRIK
103.8	1.54	-17.92	3.81	3.93	2.35	JHJY
101.09	4.6	-77.49	-1.93	3.59	2.48	JUIP
102.26	2.21	-27.73	5.23	3.81	2.35	JUML
101.66	3.56	-52.12	1.04	3.97	2.65	KKBH
103.32	2.03	-22.92	3.58	4.13	2.46	KLUG
103.45	1.33	-17.02	3.76	4.15	2.55	KUKP
99.85	6.33	-148.87	-34.99	3.51	2.73	LGKW
103.83	2.45	-26.65	3.08	4.37	2.63	MERS
101.41	3.14	-50.37	2.32	3.99	2.61	MERU
103.39	3.49	-35.15	1.71	4.06	2.56	PEKN
100.56	4.21	-85.62	-1.84	3.96	2.55	PUPK
100.7	5.22	-102.29	-11.99	3.54	2.54	SELM
100.49	5.64	-116.43	-14.03	3.5	2.64	SGPT
104.11	1.37	-16.18	3.84	3.95	2.31	TGPG
102.42	3.45	-41.55	1.49	4.6	3.16	TLOH
101.72	2.99	-42.63	4.54	4.41	2.77	UPMS
100.51	6.46	-122.47	-23.1	4.26	3.12	UUMK
118.12	5.84	-9.5	-6.02	8.22	3.37	SAND
117.88	4.26	-5.64	1.98	9.8	3.73	TAWX
99.08	10.61	-155.07	-74.82	3.95	2.37	BANH
101.05	13.12	-68.36	-38.35	2.65	2.03	CHON
100.12	15.67	-39.38	-44.04	4.12	2.75	NAKH
98.3	7.76	-252.5	-101.93	2.49	1.85	PHUK
101.03	12.76	-74.28	-37.1	2.36	1.81	RYNG
104.42	14.9	-32.64	-18	3.03	2.18	SRIS
100.01	15.38	-47.15	-39.54	2.36	1.92	UTHA

Table 4. Subfaults, listed – and counted – from South to North along the source zone.

Fault segment	LONG(*) E	LAT(*) N	W (km)	L (km)	Strike (deg)	Dip (deg)	Top (km)
1 deep	95.845	2.671	113.728	137.154	301.80	13.22	10.1
1 shallow	95.210	1.915	110.273	137.211	301.80	5.20	0.1
2 deep	94.964	3.312	113.624	109.662	309.14	13.23	10.1
2 shallow	94.300	2.583	110.137	123.126	309.50	5.21	0.1
3 deep	94.183	4.206	111.504	125.250	328.16	13.48	10.1
3 shallow	93.400	3.667	106.331	158.965	329.90	5.40	0.1
4 deep	93.582	5.473	103.985	182.400	336.16	14.48	10.1
4 shallow	92.850	5.133	90.568	183.497	341.05	6.34	0.1
5 deep	93.084	7.051	101.266	163.410	342.91	14.88	10.1
5 shallow	92.350	6.750	89.367	172.928	341.39	6.42	0.1
6 deep	92.524	8.416	101.569	176.108	334.56	14.83	10.1
6 shallow	91.733	8.1667	93.561	181.210	334.66	6.14	0.1
7 deep	92.089	10.085	98.863	167.488	357.33	15.25	10.1
7 shallow	91.312	10.075	88.300	204.321	0.77	6.50	0.1
8 deep	92.259	11.637	95.999	156.887	10.71	15.71	10.1
8 shallow	91.562	11.750	80.698	166.563	12.08	7.12	0.1
9 deep	92.602	13.067	92.323	167.403	15.94	16.36	10.1
9 shallow	91.988	13.250	73.763	172.847	17.23	7.79	0.1

(*) Longitude and latitude refer to central point on the upper edge of each subfault.

Table 5. Best model parameters values for the resolution (checkerboard) tests. Target values are in brackets. Subfaults are counted from South to North.

Subfault	T.G.+SAT		GPS		GPS Bigger patches		JOINT	
	Slip (m)	*Rake (deg)*	*Slip (m)*	*Rake (deg)*	*Slip (m)*	*Rake (deg)*	*Slip (m)*	*Rake (deg)*
1 deep	**4***(5)*	**90***(90)*	**10***(5)*	**90***(90)*	**4***(5))*	**95***(90)*	**4***(5)*	**90***(90)*
1 shallow	**16***(15)*		**12***(15)*				**14***(15)*	
2 deep	**15***(15)*		**1***(15)*				**16***(15)*	
2 shallow	**5***(5)*		**2***(5)*				**7***(5)*	
3 deep	**5***(5)*		**20***(5)*				**6***(5)*	
3 shallow	**14***(15)*		**4***(15)*				**15***(15)*	
4 deep	**16***(15)*	**130***(130))*	**11***(15)*	**130***(130))*	**15***(15)*	**130***(130)*	**16***(15)*	**135***(130)*
4 shallow	**5***(5)*		**7***(5)*				**4***(5)*	
5 deep	**5***(5)*		**21***(5)*				**6***(5)*	
5 shallow	**15***(15)*		**0***(15)*				**16***(15)*	
6 deep	**16***(15)*		**8***(15)*				**17***(15)*	
6 shallow	**4***(5)*		**27***(5)*				**5***(5)*	
7 deep	**5***(5)*	**90***(90)*	**5***(5)*	**110***(90)*	**9***(5)*	**100***(90)*	**5***(5)*	**90***(90)*
7 shallow	**14***(15)*		**7***(15)*				**14***(15)*	
8 deep	**16***(15)*		**13***(15)*				**15***(15)*	
8 shallow	**6***(5)*		**24***(5)*				**7***(5)*	
9 deep	**5***(5)*		**6***(5)*				**5***(5)*	
9 shallow	**16***(15)*		**1***(15)*				**16***(15)*	
	Vel. (km/s)						***Vel. (km/s)***	***Rigid. (GPa)***
Subf. 1-4 (shall.)	**1.50***(1.50)*						**1.50***(1.50)*	**30***(30)*
Subf. 1-4 (deep)	**2.50***(2.50)*						**2.50***(2.50)*	
Subf. 5-9 (shall.)	**1.00***(1.00)*						**1.00***(1.00)*	**10***(10)*
Subf. 5-9 (deep)	**2.25***(2.00)*						**2.00***(2.00)*	

Table 6. Best and average models for the 2004 Sumatran earthquake source from the joint inversion of tide-gage, satellite, and GPS data.

Subfault	BEST		AVERAGE	
	Slip (m)	*Rake (deg)*	*Slip (m)*	*Rake (deg)*
1 deep	**1**	**95**	**7±7**	**94±4**
1 shallow	**21**		**21±7**	
2 deep	**34**		**30±4**	
2 shallow	**0**		**4±5**	
3 deep	**22**		**23±4**	
3 shallow	**33**		**30±5**	
4 deep	**8**	**95**	**8±2**	**104±12**
4 shallow	**16**		**17±5**	
5 deep	**3**		**4±3**	
5 shallow	**0**		**5±5**	
6 deep	**12**		**13±4**	
6 shallow	**18**		**15±7**	
7 deep	**3**	**135**	**3±3**	**125±11**
7 shallow	**1**		**4±5**	
8 deep	**8**		**11±6**	
8 shallow	**0**		**4±6**	
9 deep	**6**		**8±6**	
9 shallow	**0**		**4±6**	
	Velocity (km/s)	*Rigidity (GPa)*	*Velocity (km/s)*	*Rigidity (GPa)*
First half of the rupture (shallow)	**2.00**	**20**	**1.9±0.3**	**20±2**
First half of the rupture (deep)	**3.25**		**3.3±0.2**	
Second half of the rupture (shallow)	**0.50**	**30**	**0.9±0.7**	**25±7**
Second half of the rupture (deep)	**2.00**		**2.2±0.7**	

Figures

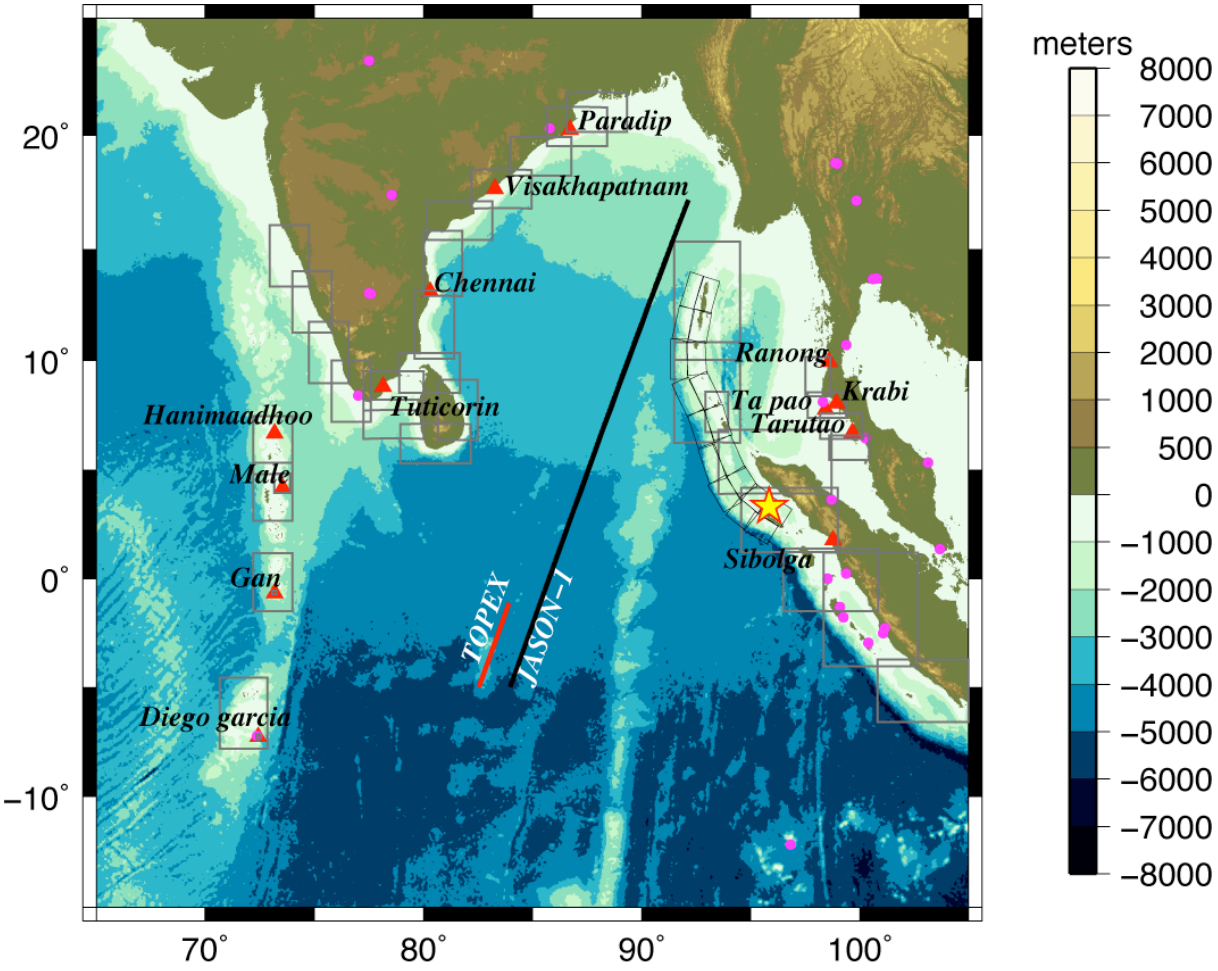

Figure 1. Map of the computational domain for the tsunami propagation. The star indicates the position of the Sumatra 2004 earthquake epicenter. Thin black lines mark the surface projection of the subfaults used in this study. Red triangles show the locations of tide-gages stations used in the inversions. The black and red lines are the projections at the sea surface of the altimetric satellites tracks portions used in the inversions. The magenta dots show the GPS stations used in the inversion, falling in the tsunami computational domain. Gray rectangles are the borders of the nautical charts we digitized (cf. Tab. 2).

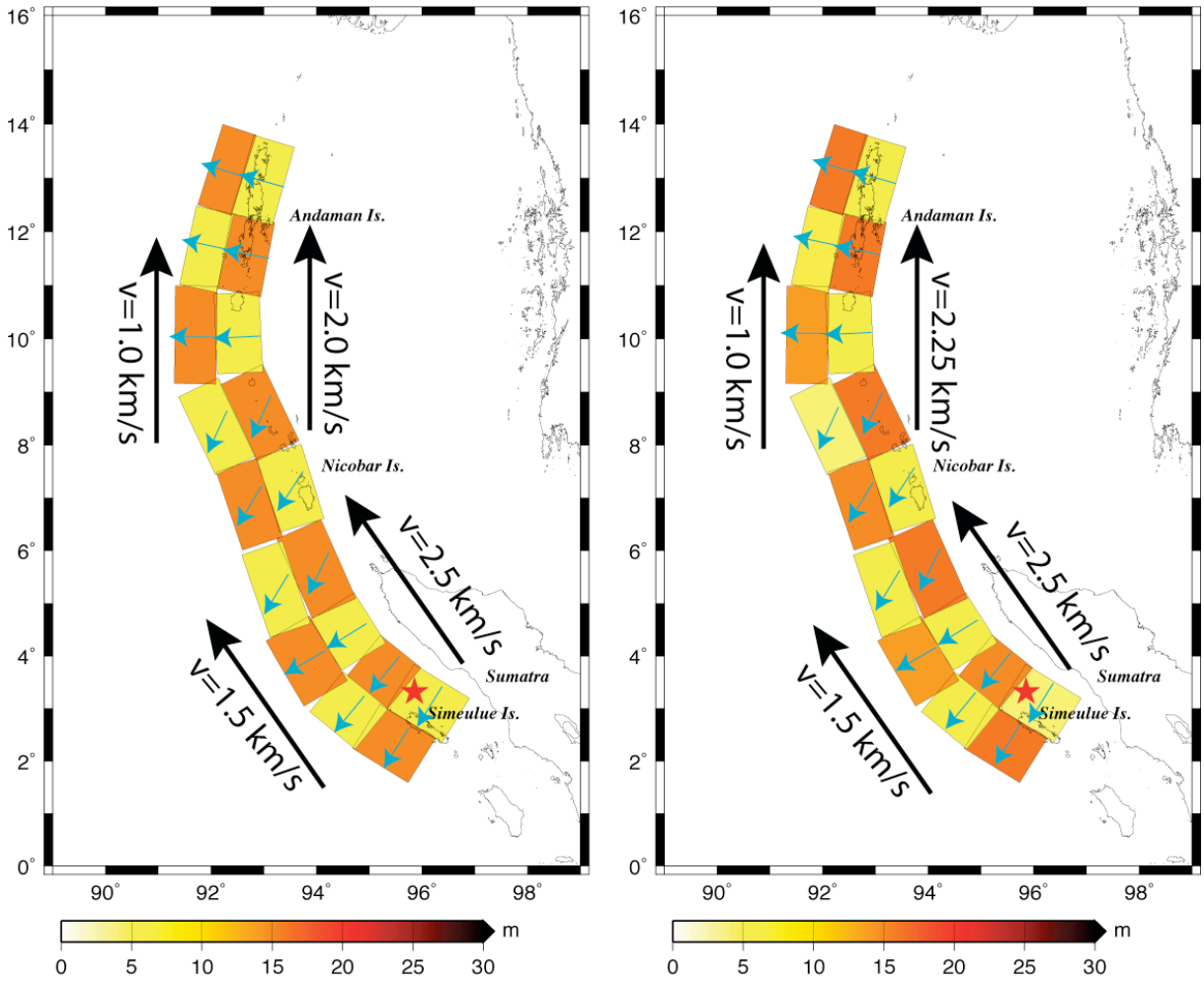

Figure 2. Checkerboard (resolution) test for the tsunami dataset, i.e. the tide-gage and the satellite altimeter data. The free inversion parameters are slip, rake, and rupture velocity. The target checkerboard model is shown in the left panel, and the best model retrieved by the inversion in the right panel. The target slip distribution, with alternating 5 and 15 meters values is represented by the subfault color. Rake directions are indicated by blue arrows, rupture velocities by the numbers besides the black arrows at both sides of the fault. The checkerboard slip pattern of the target model is recovered fairly well, as well as the rake and the rupture velocities. Numerical values of all inverted parameters (slip, rake and velocity) are reported in Table 5, columns 2-3.

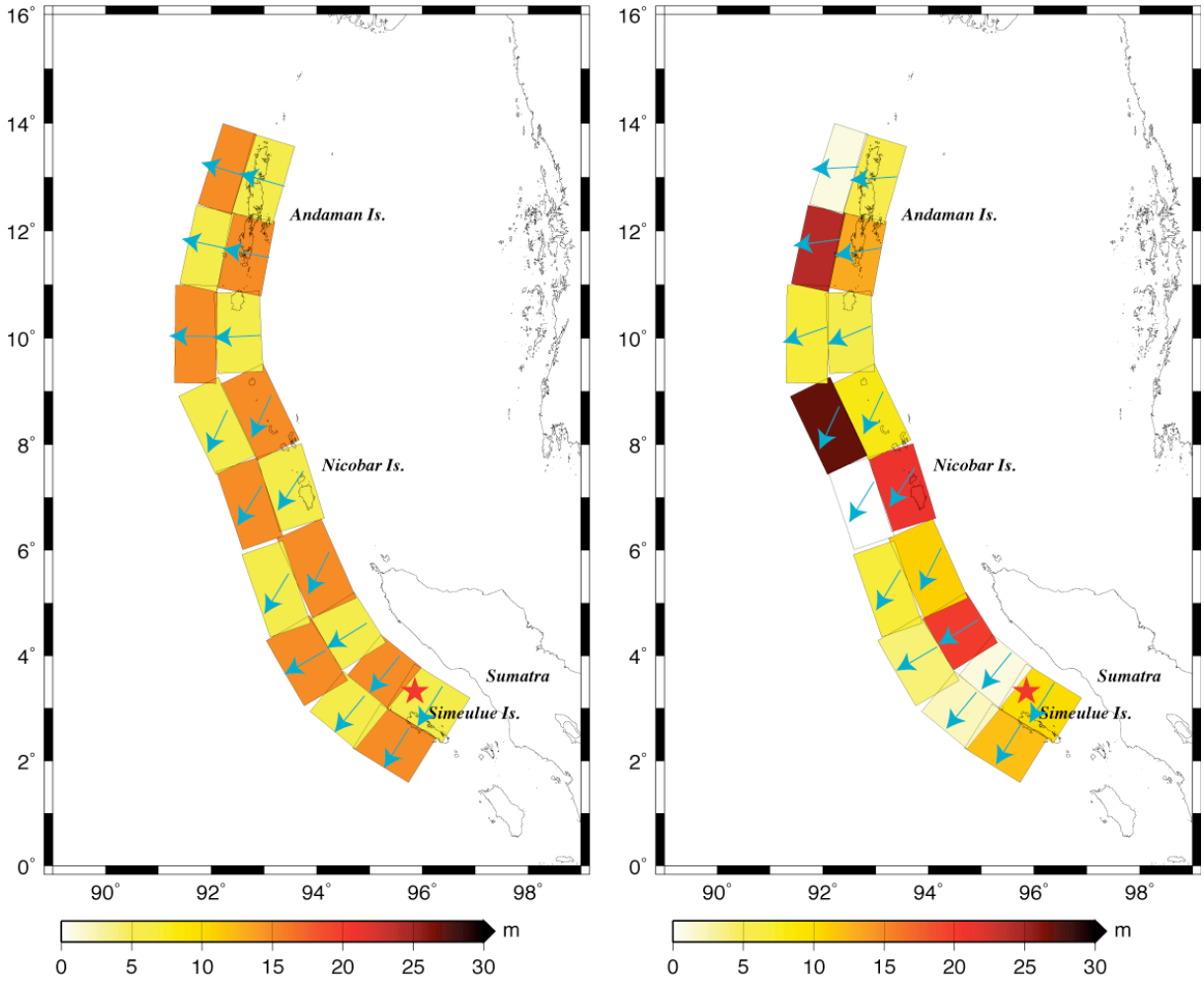

Figure 3. Checkerboard (resolution) test for the geodetic dataset. The free inversion parameters are slip and rake. Colors and symbols are as described in caption of Figure 2, with exception for the velocity, that is not inverted by static data. The checkerboard slip pattern (left panel) is totally missed in the best model (right panel), while the rake is correctly recovered with the exception of the northernmost subfaults. Numerical values of all inverted parameters (slip, rake) are reported in Table 5, columns 4-5.

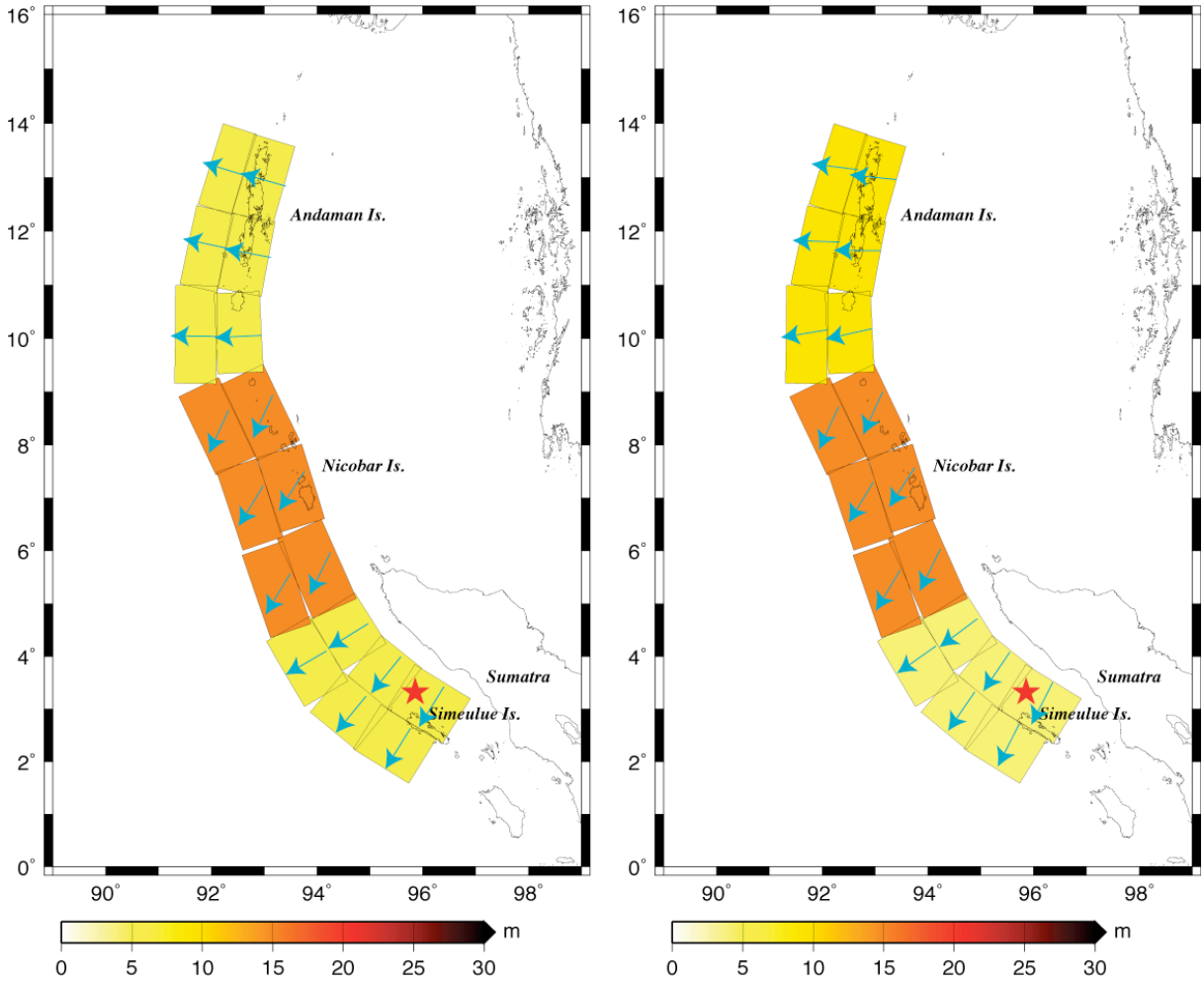

Figure 4. Resolution test for the geodetic dataset, with the target model featuring broader patches of slip (left panel); see also caption of Figure 3. In this case, with a lower spatial resolution on the slip distribution, the geodetic dataset is sufficient to recover the alternating slip pattern (see the best model in the right panel), even if the resolution further degrades in the northernmost stretch, where both slip and rake are partially missed. Numerical values of all inverted parameters (slip, rake) are reported in Table 5, columns 6-7.

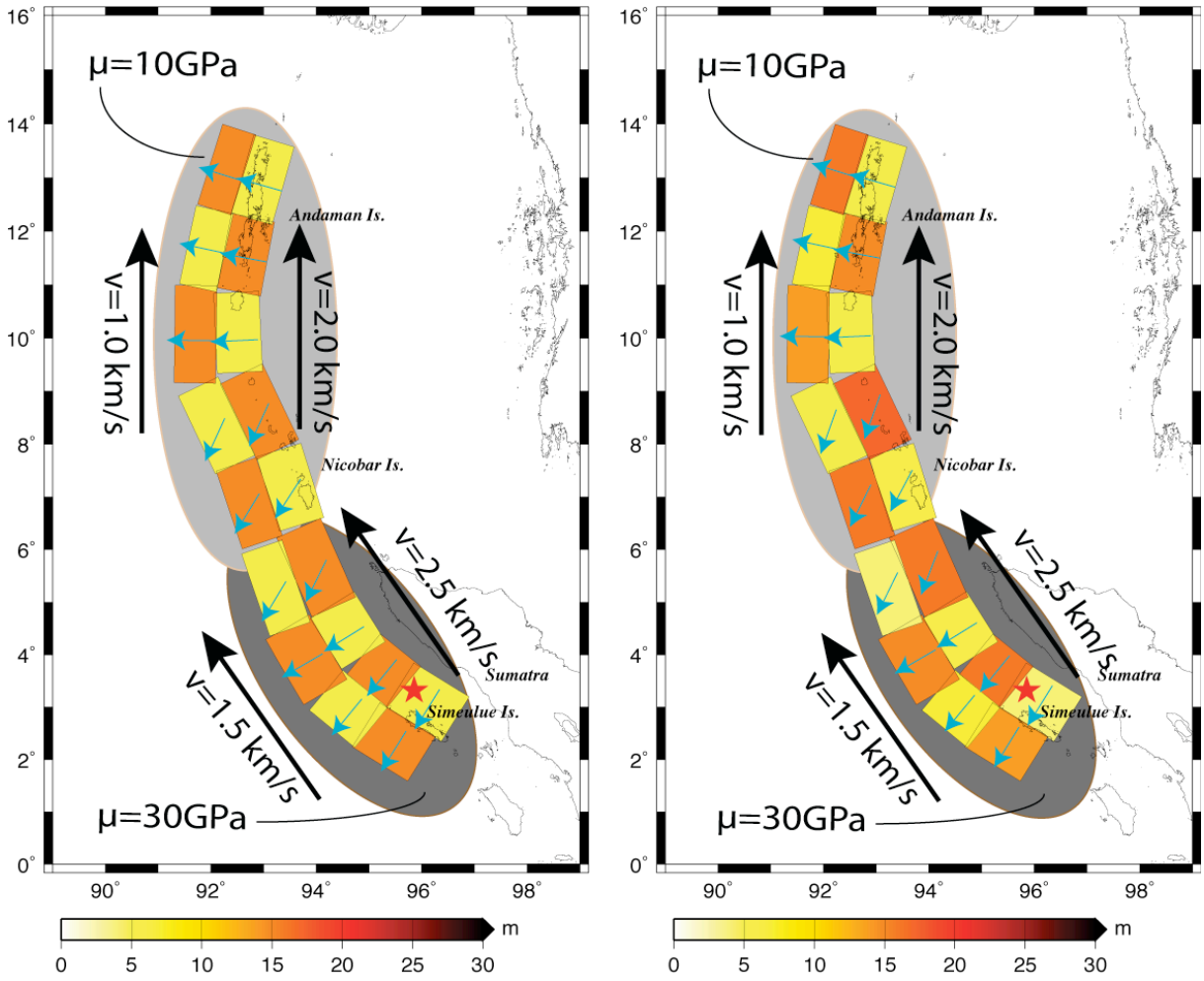

Figure 5. Checkerboard (resolution) test for the joint inversion of the tsunami and geodetic datasets. The free parameters in the joint inversion are: slip, rake, velocity, and rigidity. Gray ellipses under the source zone highlight that in the present case we have the rigidity as an extra free parameter. For a description of other colors and symbols see caption of Figure 2. The target model configuration is depicted in the left panel. The checkerboard slip pattern is recovered fairly well (best model shown in the right panel). Numerical values of the slip, rake, velocity, and rigidity featured by the best model are reported in the last two columns of Table 5.

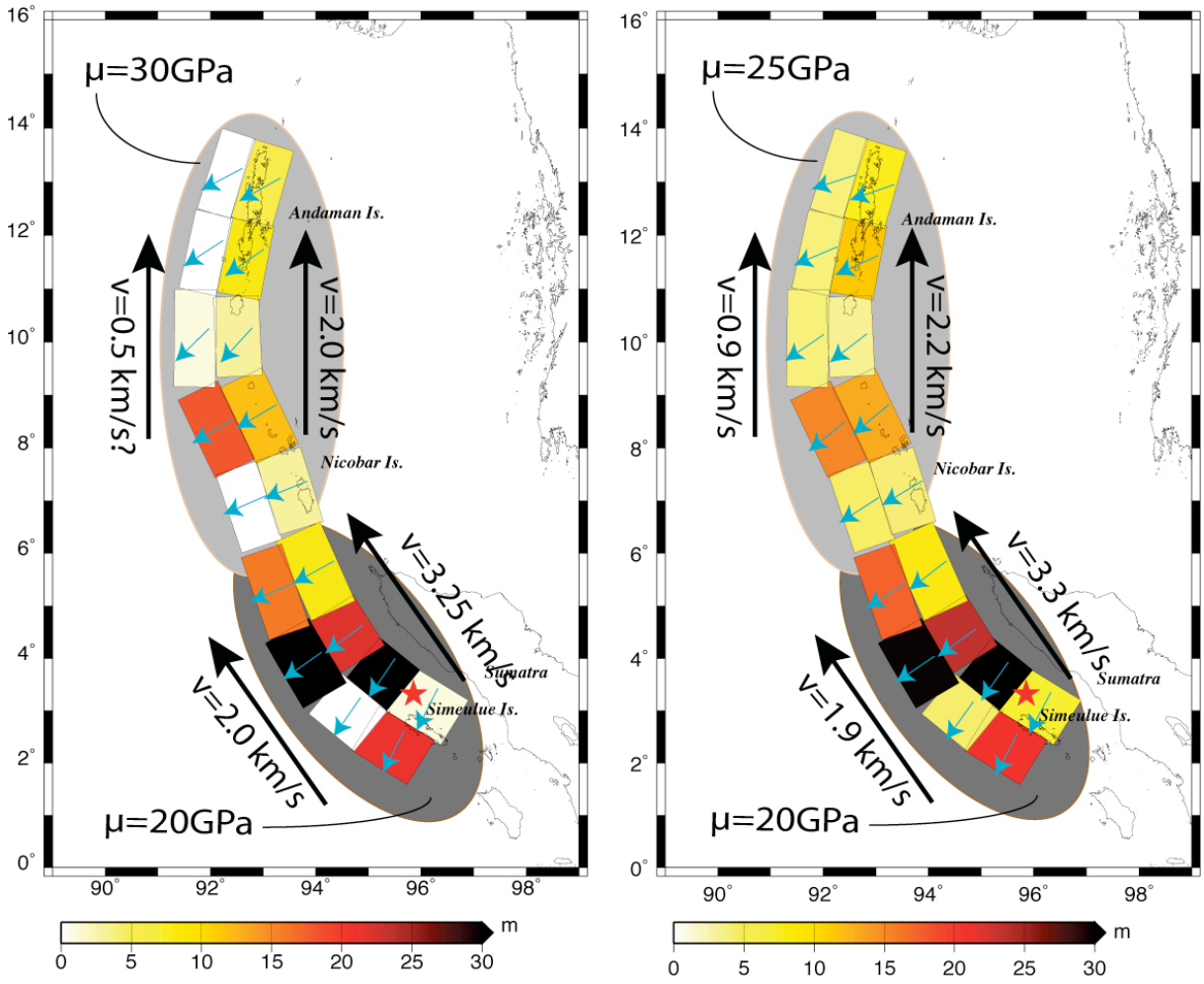

Figure 6. Best (left) and average (right) models for the 2004 Sumatran earthquake, as recovered by the joint inversion of the tsunami and geodetic datasets. Gray ellipses under the source zone highlight that in the present case we have the rigidity as an extra free parameter. Numerical values for the slip, rake, velocity and rigidity are reported in Table 6. The values featured by the best model are listed in columns 1 and 2; those of the average model, with their associated errors, in columns 3 and 4.

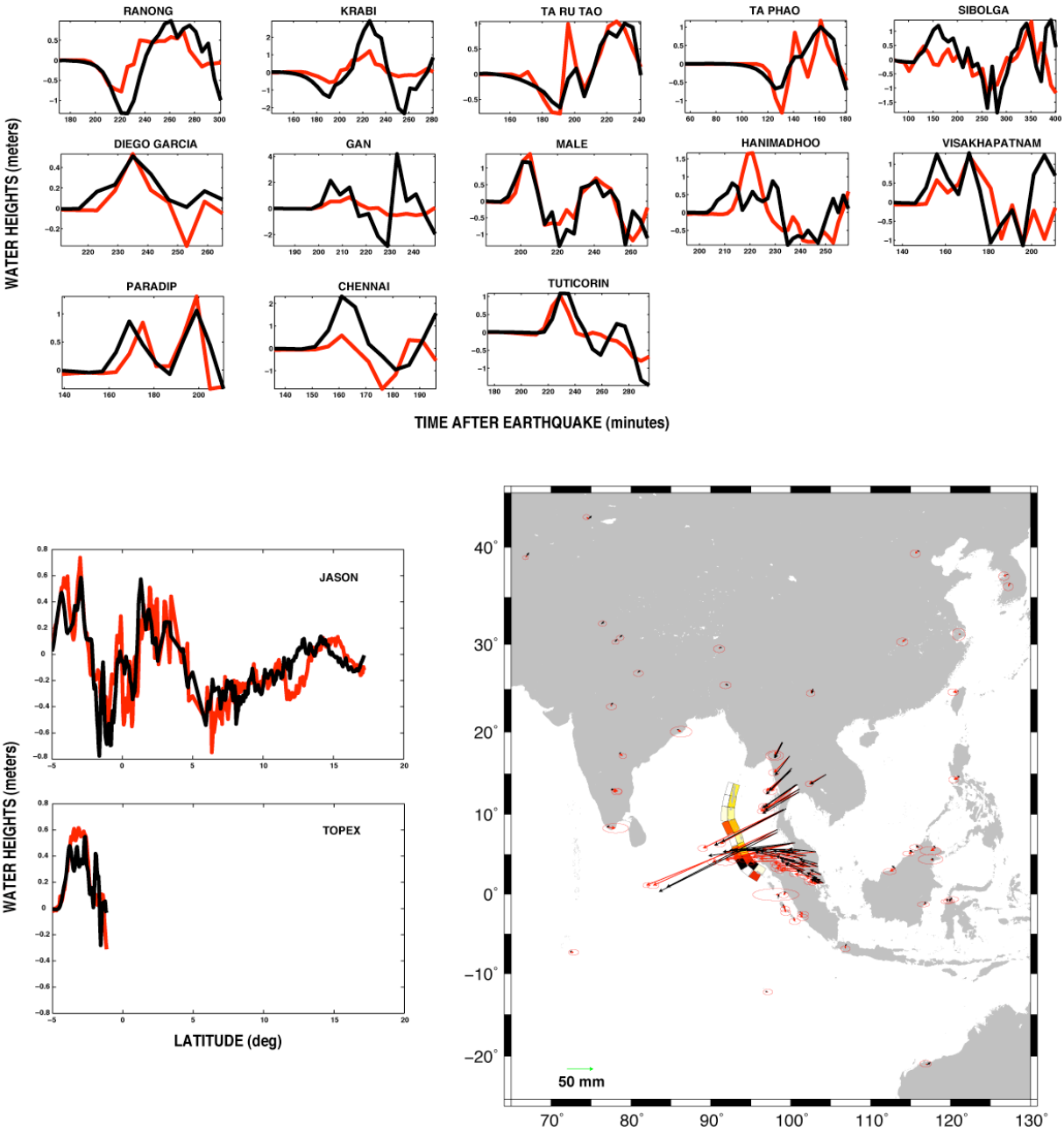

Figure 7. Comparison between the experimental and synthetic datasets obtained with the best source model for the 2004 earthquake. Tide-gage and satellite tsunami records are represented with red lines; their synthetic counterparts with black lines. Red arrows (with error ellipses) show the geodetic data, and black arrows their synthetic counterparts.

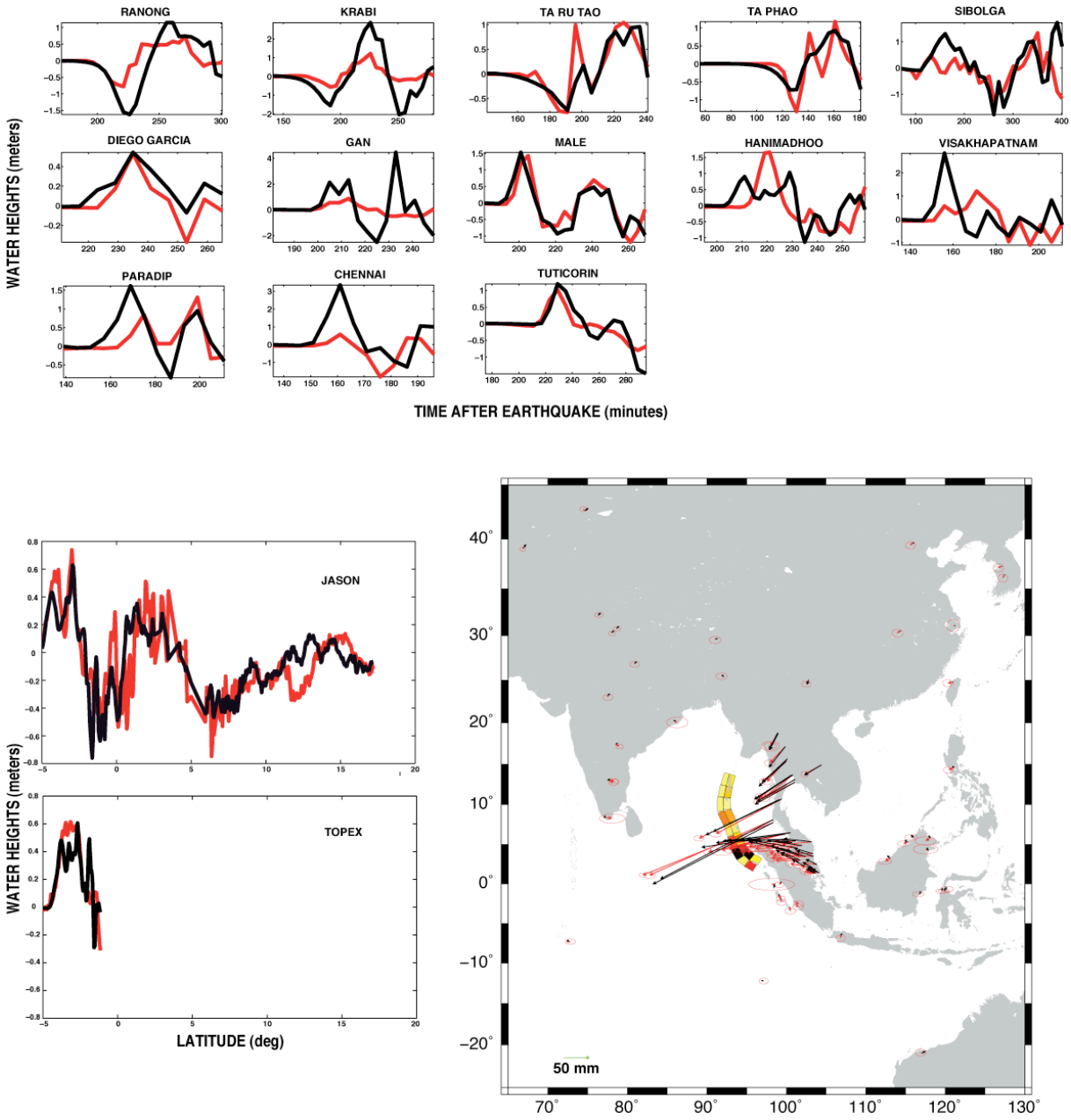

Figure 8. Comparison between the experimental and synthetic datasets obtained here with the average source model for the 2004. See also caption of Figure 7.

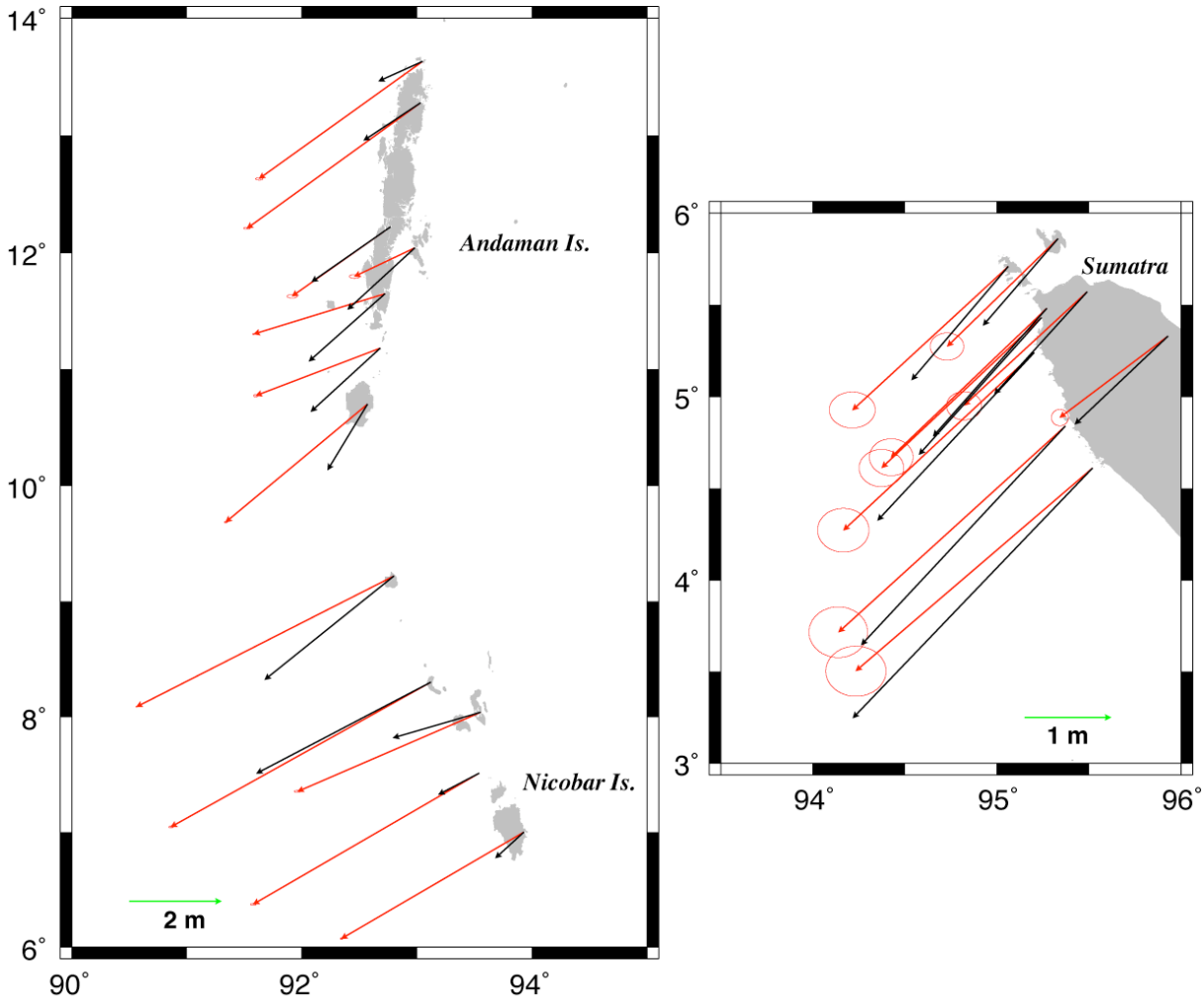

Figure 9. Comparison between the forward predictions of our best model (black arrows) with the geodetic (campaign) data in the near-field, represented by red arrows with error circles. The model under-predicts the data, particularly over the Andaman and Nicobar islands, and even in the Northern part of Sumatra.

Conclusions

Subduction zones are the favorite places to generate tsunamigenic earthquakes, where friction between oceanic and continental plates causes the occurrence of a strong seismicity. Large, shallow earthquakes in subduction zones contribute ~90% of the total seismic moment released worldwide [*Pacheco and Sykes,* 1992; *Stern,* 2002]. These earthquakes have a focal mechanism indicating thrust faulting along the subduction interface. Because such earthquakes are so powerful, they constitute a special hazard to people who live near convergent margins. Furthermore, since several of these earthquakes occur under the ocean, the sea-bottom displacement caused by the submarine fault motion may generate large tsunamis.

The topics and the methodologies discussed in this thesis are focussed to the understanding of the rupture process of the seismic sources of great earthquakes that generate tsunamis. A better knowledge of the tsunamigenic earthquakes and, more specifically, of the link existing between the earthquake magnitude and the tsunami magnitude is one of the open issues about tsunamis. Actually, it may happen that a large earthquake generates a small tsunami and *vice versa*. For example the 2007 M_W 8.4 Sumatra earthquake generated a much smaller tsunami than the weaker 2006 M_W 7.8 Java earthquake, which produced a very destructive waves over the adjacent coastline.

The tsunamigenesis is controlled by several kinematical characteristic of the parent earthquake, as the focal mechanism, the depth of the rupture, the slip distribution along the fault area and by the mechanical properties of the source zone. Each of these factors plays a fundamental role in the tsunami generation.

Therefore, inferring the source parameters of tsunamigenic earthquakes is crucial to understand the generation of the consequent tsunami and so to mitigate the risk along the coasts.

Unfortunately, the direct observation of an earthquake is not feasible, and this is true in particular for submarine earthquakes, which are the main subject of this thesis. Nevertheless, we can identify several observables that are measured by instruments positioned on the surface of the Earth and even on the ocean bottom. Therefore, the typical way to proceed when we want to gather information regarding the source process is to have recourse to the inversion of geophysical data that are available.

In the last years, the importance of tsunami data (for example tide-gage and ocean bottom pressure records or runup heights measured inland) to retrieve the seismic source parameters has been demonstrated in several occasions. Tsunami data, in fact, are useful to constrain the portion of the fault area that extends offshore, generally close to the trench that, on the contrary, other kinds of data are not able to constrain [*Satake*, 1993].

In this thesis we have discussed the rupture process of some recent tsunamigenic events, as inferred by means of an inverse method. Particular attention has been paid in investigating how well different geophysical datasets can constrain different source parameters, as well as various aspects of the rupture process.

The first tsunamigenic event that we have presented is the 2003 Tokachi-Oki (Japan) earthquake (Mw 8.1). In this study we have inferred the slip distribution on the fault by inverting tsunami waveform, GPS, and bottom-pressure data. Since this earthquake occurred near the Kuril trench, then a large part of the fault plane is positioned offshore. GPS data, since are instruments positioned on land, allow to well constraining the slip distribution onshore, whereas the tsunami data are very sensitive to the slip distribution offshore. The joint inversion of tsunami and geodetic data has revealed a much better constrain for the slip distribution on the fault rather than the separate inversions of single datasets. The study of the Tokachi-Oki earthquake, in particular, demonstrates that the installation of offshore geodetic stations could have important implications in the planning of tsunami warning systems, and therefore it could help to mitigate the tsunami risk along the coastlines.

Then we have studied the earthquake occurred on 2007 in southern Sumatra (Mw 8.4), which in spite of its high magnitude it generated only a small tsunami. By inverting several tsunami waveforms, both in the near and in the far field, we have determined the slip distribution and the mean rupture velocity along the causative fault. Since the largest patch of slip was concentrated on the deepest part of the fault, this is the likely reason for the small tsunami waves that followed the earthquake, pointing out how much the depth of the rupture plays a crucial role in controlling the tsunamigenesis. Moreover the 2007 earthquake did not rupture the whole source zone of the previous 1833 event nor released the likely accumulated moment since then. Thus it has been made an hypothesis about a future big earthquake that will possibly occur in the unruptured area extending between South Pagai and the south of Siberut island.

Finally, we have presented a new rupture model for the great 2004 Sumatra earthquake (Mw 9.2), one of the most important tsunamigenic events in the last century. This event has been studied following several different approaches and using different kinds of data. In this thesis we have performed the joint inversion of tsunami waveform, GPS and satellite altimetry data, to infer the slip distribution, the slip direction, and the rupture velocity on the fault. Furthermore, in this work we have presented a novel method to estimate, in a self-consistent way, the average rigidity of the source zone, which resulted significantly lower than the PREM values at the corresponding depths. The estimation of the source zone rigidity is important since it may play a significant role in the tsunami generation and, particularly for slow earthquakes, a low rigidity value is sometimes necessary to explain how a relatively low seismic moment earthquake may generate significant tsunamis [*Geist and Bilek,* 2001]; this latter point may be relevant for explaining the mechanics of the tsunami earthquakes, one of the open issues in present day seismology.

The investigation of these tsunamigenic earthquakes has underlined the importance to use a joint inversion of different geophysical data to determine the rupture characteristics.

The results shown in this thesis are a step toward future tsunami investigations, as several improvements in tsunami modeling and in the source parameterization can be done. One of the future developments of this work will be to use parallel codes to model the tsunami propagation; these codes also implement a system of nested grids that allow using high-resolution bathymetric datasets without increasing the computation time. Using high-resolution bathymetry, in fact, allows for better modeling the tsunami waves, for example into the harbors, where the nonlinear effects of the propagation become relevant.

It will be important also to parameterize the fault area by using smaller subfaults and smoothing factors to estimate the slip distribution in a more detailed way.

Furthermore, since the rheological properties play a role in the tsunamigenesis, the layering of the lithosphere should be taken into account for both tsunami and geodetic modeling. Even if a vertical layered Earth's model is more realistic than a homogeneous half-space, another future development of this thesis will be the implementation of a 3D model for the Earth – by using for example finite or spectral element modeling – which allows to take into account also some strong lateral

heterogeneities of the litosphere in tectonically complex regions like the subduction zones.

The developments outlined above, supported by high-performance computing, can improve the capability to accurately estimate the kinematical source parameters controlling the fault motion and the consequent tsunamis. Furthermore the results shown here have important implications for the implementation of new tsunami warning systems – particularly in the near-field – the improvement of the current ones, and furthermore for the planning of the inundation maps for tsunami-hazard assessment along the coastal area.

Appendix A

Simulated annealing

A.1 Heat Bath Algorithm

Simulated Annealing (SA) is became in the last years an amply discussed heuristics. *Johnson et al.* [1989] provide excellent descriptions of the SA with analogies and comparisons respect with the physics of the phenomenon of the crystalline structures formation. The most widespread applications of the SA regard combinatorial problems, but this technique revealed very efficient also with geophysical inverse problems.

Then SA is a research methodology strongly suitable for many optimization problems and has its bases in the statistics mechanics. *Kirkpatrick et al.* [1983] were developed this technique originally to solve combinatorial optimization problems. SA was born as a method for the simulation of the solid *annealing*. Annealing is a process by which a solid, led to the fluid state - by means of high temperature heating - then it is brought back to the solid or crystalline state – at low temperatures - gradually checking and reducing the temperature. At high temperatures, the atoms of the system are in a highly disordered state and therefore the energy of the system is high. To bring back these atoms at one highly ordered crystalline configuration (statistically), the temperature of the system must be lowered. During this process however the quick lowering of the temperature can cause some imperfections in the crystalline lattice with a consequent metastable state, characterized by fractures or cracking (*thermal stress*). Annealing avoids this phenomenon proceeding with a gradual cooling of the system, leading it to a globally stable structure.

In this configuration the system is called in a *thermal equilibrium* at the temperature *T* if the probability *P*(*Ei*) of a state with energy *Ei* is governed by the *Boltzmann distribution* :

$$P(E_i) = \frac{\exp\left(-\frac{E_i}{KT}\right)}{\sum_{j \in S} \exp\left(-\frac{E_j}{KT}\right)} \qquad \text{(A.1)}$$

where the set *S* consists of all possible configurations, *K* is Boltzmann's constant and *T* is the temperature.

At high temperatures all the states of energy are equally likely, whereas at low temperatures the system is characterized surely by states of minimum energy.

Basing on this physical process *Metropolis et al.* [1953] developed an algorithm to simulate the behaviour of a collection of atoms in thermal equilibrium at a certain temperature. This algorithm has a fundamental role for the application of SA technique in the optimization problems.

Main feature of the Metropolis algorithm is that it generates a set of configurations for each temperature *T* with the property that the energies of the different configurations can be represented by the Boltzmann's distribution.

The procedure of this method starts assigning an initial configuration for the parameters (atoms) in a system with energy E_0. In a next step are generated then other configurations perturbing lightly and in a random way the current configuration. The decision to accept or reject the configuration is based on the difference between the energy of the current configuration and that of the *new* configuration.

The algorithm accepts always a new configuration if its energy E_j is lower than that current (E_i).

On the other hand, if the energy of the current configuration is lower than that new then it is accepted with the probability

$$P(\Delta E) = \exp\left(-\frac{\Delta E_{ij}}{KT}\right) \quad \text{(A.2)}$$

where

$$\Delta E_{ij} = E_j - E_i$$

This algorithm can be defined as a two-step procedure, because in a first step is choose a configuration (model) and then the algorithm decide to accept or reject it. This procedure thus has the problem that many of these models will be rejected, especially at low temperatures.

Several algorithms have been proposed to remedy this situation, one of which is the *Heat Bath* [*Rothman,* 1986].

To avoid a high rejection to acceptance ratio this procedure computes the relative probabilities of acceptance of each trial "move" before any random guesses are made; in this sense this one is a one-step procedure.

Briefly, we explain the way of working of this algorithm.

Consider a model vector **m** consisting of N model parameters. Next assume that each of these parameters m_i can take M possible values. Assigning some lower and upper bounds and a search increment for each parameter can obtain this. In this way we obtain M^N models.

Call with m_{ij} the model parameters with i=1…N and j=1…M (the index i is the model parameter number and j is the discrete values of the model parameter). The algorithm starts choosing an initial random model we call $\mathbf{m_0}$, and then each of model parameters is visited sequentially (Fig. A.1).

Heat Bath Algorithm

---

start from a random model $\mathbf{m_0}$ with energy $E(\mathbf{m_0})$

loop over temperature (T)

* loop over number of iterations/temperature

* * loop over number of model parameters (i=1,……..,N)

* * * loop over model values j, j=1,……..,M

* * * * evaluate $E(\mathbf{m} \mid m_i = m_{ij})$ and calculate

$$\hat{P}_{ij} = \exp\left(-\frac{E(\mathbf{m} \mid m_i = m_{ij})}{T}\right)$$

* * * end loop

* * * draw a j from the above distribution

* * end loop

* end loop

end loop

Figure A.1. Schematic representation of the Heath Bath Algorithm (after *Sen and Stoffa,* [1995]).

At this point we compute for each model parameter the marginal probability density function

$$\hat{P}\left(\mathbf{m} \mid m_i = m_{ij}\right) = \frac{\exp\left(-\frac{E(\mathbf{m} \mid m_i = m_{ij})}{T}\right)}{\sum_{k=1}^{M}\left(-\frac{E(\mathbf{m} \mid m_i = m_{ij})}{T}\right)} \qquad \text{(A.3)}$$

where $E(\mathbf{m} \mid m_i = m_{ij})$ is the energy for a model $\mathbf{m}$ whose i^{th} model parameter has value $m_{ij.}$ At this point we extract a random number from the uniform distribution U[0,1] and we map it onto the pdf defined by the (A.3). We first compute a cumulative probability C_{ij} from $\hat{P}\left(\mathbf{m} \mid m_i = m_{ij}\right)$ and then we draw a random number r from the uniform distribution; we select m_{ij}=m_{ik}=m_i at the point j=k where C_{ij}=r.

The effect of this procedure is that at high temperatures the distribution is practically uniform and therefore we can consider every model parameter as equally likely. On the other hand, at very low temperatures the pdf of the single model parameter is

peaked and then this parameter is most probable than others. In this sense the cost function is much more influenced and therefore its value is lowered. Thus, the new model parameter replace that old in **m** and this process is repeated sequentially for each model parameter.

The temperature in the SA technique has not a direct analogy into the optimization; it is a *control parameter* that defines the region of the state-space explored by the algorithm in a particular phase. It is not so easy setting this control parameter; establishing when and until what appropriate value the temperature has to decrease during the annealing permits to avoid the cost function remains entrapped in some local minimum. Before starting with the algorithm therefore we have to set a *cooling scheduling*. In this phase we select the *start* and *final Temperatures* values, and the number of *baths* for the model parameters. The selection for each of these control parameters is not simple to decide a priori and does not exist a gold rule to set up the cooling scheduling; however, generally the experience and an heuristic approach is sufficient to perform a reasonable global search.

References

Ablain M., J. Dorandeu, P. Y. Le Traon, and A. Sladen (2006), High resolution altimetry reveals new characteristics of the December 2004 Indian Ocean tsunami, *Geophys. Res. Lett.*, *33*, L21602, doi:10.1029/2006GL027533.

Ammon C. J., C. Ji, H.K. Thio, D. Robinson, S. Ni, V. Hjorleifsdottir, H. Kanamori, T. Lay, S. Das, D. Helmberger, G. Ichinose, J. Polet and D. Wald (2005), Rupture process of the 2004 Sumatra-Andaman earthquake, *Science*, *308*, 1133-1139, doi:10.1126/science.1112260.

Amoruso A., L. Crescentini, and C. Fidani (2004), Effects of crustal layering on source parameter inversion from coseismic geodetic data, *Geophys. J. Int., 159*, 353-364, doi:10.1111/j.1365-246X.2004.02389.x.

Baba T., K. Hirata, T. Hori, and H. Sakaguchia (2006), Offshore geodetic data conducive to the estimation of the afterslip distribution following the 2003 Tokachi-oki earthquake*, Earth Planet. Sci. Lett. 241*, 281 – 292, doi:10.1016/j.epsl.2005.10.019.

Banerjee P., F.F. Pollitz and R. Bürgmann (2005), The size and duration of the Sumatra-Andaman earthquake from far-field static offsets, *Science*, *308*, 1769-1772, doi:10.1126/science.1113746.

Banerjee P., F.F. Pollitz, B. Nagarajan, and R. Bürgmann (2007), Coseismic Slip Distributions of the 26 December 2004 Sumatra–Andaman and 28 March 2005 Nias Earthquakes from GPS Static Offsets, *Bull. Seismol. Soc. Am., 97*(1A), S86–S102, doi:10.1785/0120050609.

Bilek S.L. (2007), Using Earthquake Source Durations along the Sumatra–Andaman Subduction System to Examine Fault-Zone Variations, *Bull. Seismol. Soc. Am., 97*(1A), S62–S70, doi: 10.1785/0120050622.

Bilek S.L., and T. Lay (1998), Variation of Interplate Fault Zone Properties with Depth in the Japan Subduction Zone, *Science, 281*, 1175-1178, doi:10.1126/science.281.5380.1175.

Bilek S.L., and T. Lay (1999), Rigidity variations with depth along interplate megathrust faults in subduction zones, *Nature, 400*, 443-446, doi:10.1038/22739.

Bilek S.L., K. Satake, and K. Sieh (2007), Introduction to the special issue on the 2004 Sumatra-Andaman earthquake and the Indian Ocean tsunami, *Bull. Seismol. Soc. Am.*, *97*, S1 – S5, doi:10.1785/0120050633.

Bilham R. (2005), A flying start, then a slow slip, *Science*, *308*, 1126-1127, doi:10.1126/science.1113363.

Bird P. (2003), An updated digital model of plate boundaries, *Geochem. Geophys. Geosystems*, *4*, 1027, doi:10.1029/2001GC000252.

Borrero J.C., K. Sieh, M. Chlieh, and C. E. Synolakis (2006), Tsunami inundation modeling for western Sumatra, *Proc. Nat. Acad. Sci.*, *103*, 19673-19677.

Boschi E., E. Casarotti, R. Devoti, D. Melini, G. Pietrantonio and F. Riguzzi (2006), Coseismic deformation induced by the Sumatra earthquake, *J. Geodyn., 42*, 52-62.

Boschi L., A. Piersanti and G. Spada (2000), Global postseismic deformation: deep earthquakes, *J. Geophys. Res., 105*, 631-652, doi:10.1029/1999JB900278.

British Oceanographic Data Center (2003). *The Centenary Edition of the GEBCO Digital Atlas* [CD-ROM], Liverpool, UK.

Bryant E. (2008), *Tsunami (The Underrated Hazard)*, Springer.

Catherine J.K., V.K. Gahalaut, and V.K. Sahu (2005), Constraints on rupture of the December 26, 2004, Sumatra earthquake from far-field GPS observations, *Earth Plan. Sc. Lett., 237,* 673-679, doi:10.1016/j.epsl.2005.07.012.

Chlieh M. et al. (2007), Coseismic slip and afterslip of the Great (Mw9.15) Sumatra-Andaman Earthquake of 2004, *Bull. Seism. Soc. Am., 97*, S152–S173, doi:10.1785/0120050631.

DART Buoy, http://nctr.pmel.noaa.gov/Dart/index.html

Dow J.M., R.E. Neilan, and G. Gendt (2005), The International GPS Service (IGS): Celebrating the 10th Anniversary and Looking to the Next Decade, *Adv. Space Res.* 36 vol. 36, no. 3, pp. 320-326, doi:10.1016/j.asr.2005.05.125.

Dragani W.C., E.E. D'Onofrio, W. Grismeyera, and M.E. Fiore (2006), Tide gauge observations of the Indian ocean tsunami, December 26, 2004, in Buenos Aires coastal waters, Argentina, *Cont. Shelf. Res., 26*, 1543-1550, doi:10.1016/j.csr.2006.03.002.

Dziewonski A. M., and D. L. Anderson (1981), Preliminary reference Earth model (PREM), *Phys. Earth Planet. Interiors, 25*, 297–356, doi:10.1016/0031-9201(81)90046-7.

Fujii Y., and K. Satake (2006), Source of the July 2006 West Java tsunami estimated from tide gauge records, *Geophys. Res. Lett.*, *33*, L24317, doi:10.1029/2006GL028049.

Fujii Y., and K. Satake (2007), Tsunami Source of the 2004 Sumatra–Andaman Earthquake Inferred from Tide Gauge and Satellite Data, *Bull. Seismol. Soc. Am.*, *97*, S192–S207, doi:10.1785/0120050613.

Fujii Y., and K. Satake (2008), Tsunami Sources of the November 2006 and January 2007 Great Kuril Earthquakes, *Bull. Seismol. Soc. Am*., *98*(3), 1559-1571, doi:10.1785/0120070221

Gahalaut V.K., B. Nagarajan, J.K. Catherine, and S. Kumar (2006), Constraints on 2004 Sumatra–Andaman earthquake rupture from GPS measurements in Andaman–Nicobar Islands, *Earth Plan. Sc. Lett., 242,* 365-374, doi:10.1016/j.epsl.2005.11.051.

Geist E.L. (1999), Local tsunamis and earthquake source parameters, *Advances in Geophysics*, *39*, 117-209.

Geist E.L., and S. L. Bilek (2001), Effect of depth-dependent shear modulus on tsunami generation along subduction zones, *Geophys. Res. Lett.*, *28*, 1315-1318.

Geist E.L., V.V. Titov, D. Arcas, F.P. Pollitz, and S.L. Bilek (2007), Implications of the December 26, 2004 Sumatra-Andaman earthquake on tsunami forecast and assessment models for great subduction zone earthquakes, *Bull. Seismol. Soc. Am.*, *97*(1A), S249-S270, doi:10.1785/0120050619.

GGCI. Geodesy and Geodinamics Center of Indonesia.

GLOSS. Global Sea Level Observing System, JCOMM/WMO/IOC UNESCO.

Gower J. F. (2005), Jason 1 detects December 26, 2004 tsunami, *Eos. Transactions American Geophysical Union*, *86*, 37-38.

Grilli S. T., M. Ioualalen, J. Asavanant, F. Shi, J. T. Kirby, and P. Watts (2007), Source constraints and model simulation of the December 26, 2004 Indian Ocean tsunami, *J. Waterw. Port Coastal Ocean Eng., 133*(6), 414-428, doi: 10.1061/(ASCE)0733-950X(2007)133:6(414).

GSI (*Geodetic Survey Institute*), http://mekira.gsi.go.jp/ENGLISH/index.html

Gu Y. J. (2006), Preface to special issue, *Surv. Geophys., 27*, 601 – 602, doi:10.1007/s10712-006-9014-3.

Gutenberg B., and C. F. Richter (1944). Frequency of earthquakes in California, *Bull. Seism. Soc. Am.* 34, 185-188.

Hartzell S. H. (1989), Comparison of seismic waveform inversion results for the rupture history of a finite fault: Application to the 1986 North Palm Springs, California, earthquake, *J. Geophys. Res.*, 94, 7515–7534.

Hashimoto M., N. Choosakul, M. Hashizume, S. Takemoto, H. Takiguchi, Y. Fukuda, and K. Fujimori (2006), Crustal deformations associated with the great Sumatra-Andaman earthquake deduced from countinuous GPS observation, *Earth Planets Space*, *58*, 203-209.

Hayashi Y. (2008), Extracting the 2004 Indian Ocean tsunami signals from sea surface height data observed by satellite altimetry, *J. Geophys. Res.*, 113, C01001, doi:10.1029/2007JC004177.

HDRTN, Hydrographic Department, Royal Thai Navy, Thailand.

Hébert H., A. Sladen, and F. Schindelé (2007), Numerical Modeling of the Great 2004 Indian Ocean Tsunami: Focus on the Mascarene Islands, *Bull. Seismol. Soc. Am.*, *97*(1A), S 08–S222, doi: 10.1785/0120050611.

Heinrich P., A. Piatanesi, and H. Hébert (2001), Numerical modelling of tsunami generation and propagation from submarine slumps: the 1998 Papua New Guinea event, *Geophys. J. Int.,* 145, 97-111.

Hirata K., E. L. Geist, K. Satake, Y. Tanioka, and S. Yamaki (2003), Slip distribution of the 1952 Tokachi-Oki earthquake (M8.1) along the Kuril Trench deduced from tsunami waveform inversion, *J. Geophys. Res., 108*(B4), 2196, doi:10.1029/2002JB001976.

Hirata K., Y. Tanioka, K. Satake, S. Yamaki, and E. L. Geist (2004), The tsunami source area of the 2003 Tokachi-oki earthquake estimated from tsunami travel times and its relationship to the 1952 Tokachi-oki earthquake, *Earth Planets Space 56*, 367–372.

Hirata K., K. Satake, Y. Tanioka, T. Kuragano, Y. Hasegawa, Y. Hayashi and N. Hamada (2006), The 2004 Indian ocean tsunami: tsunami source model from satellite altimetry, *Earth Planets Space*, *58*, 195-201.

Hirata K., K. Satake, Y.Tanioka and Y.Hasegawa (2007), A Review on recent studies of tsunamis in the southernmost Kuril Trench, *Proceedings of International Workshop on Tsunami - Wave Propagation, Theory, Numerical Approach and Data Inversion*, Keio Univ.

Hoechner A., A. Y. Babeyko, S. V. Sobolev (2008), Enhanced GPS inversion technique applied to the 2004 Sumatra earthquake and tsunami, *Geophys. Res. Lett.*, *35*, L08310, doi:10.1029/2007GL033133.

Honda R., S. Aoi, N. Morikawa, H. Sekiguchi, T. Kunugi, and H. Fujiwara (2004), Ground motion and rupture process of the 2003 Tokachi-oki earthquake obtained by strong-motion data of K-NET and KiK-net, *Earth Earth Planets Space*, 56, 317–322

Horikawa H. (2004), Fault geometry and slip distribution of the 2003 Tokachi-oki earthquake as deduced from teleseismic body waves, *Earth Planets Space 56*, 1011–1017.

Ichinose G., P. Somerville, H.K. Thio, R. Graves, and D. O'Connell (2007), Rupture process of the 1964 Prince William Sound, Alaska, earthquake from the combined inversion of seismic, tsunami, and geodetic data, *J. Geophys. Res., 112,* B07306, doi:10.1029/2006JB004728.

IGS, International GNSS Service, http://igscb.jpl.nasa.gov/ (last accessed March 2009).

Ioualalen M., J. Asavanant, N. Kaewbanjak, S.T. Grilli, J.T. Kirby, and P. Watts (2007) Modeling the 26 December 2004 Indian Ocean tsunami: Case study of impact in Thailand, *J. Geophys. Res., 112,* C07024, doi:10.1029/2006JC003850.

Ito Y., H. Matsubayashi, H. Kimura, T. Matsumoto, Y. Asano, and S. Sekiguchi (2004), Spatial distribution for moment tensor solutions of the 2003 Tokachi-oki earthquake (M_{JMA} = 8.0) and aftershocks, *Earth Planets Space 56*, 301-306.

Jade S., M. Ananda, P. Kumar, and S. Banerjee (2005), Co-seismic and post-seismic displacements in Andaman and Nicobar islands from GPS measurements, *Curr. Sci.,* 88, 1980–1984.

JAMSTEC (*Japan Agency for Marine-earth Science and Technology*), http://www.jamstec.go.jp/scdc/top_e.html

Ji C., Wald D.J., and D.V. Helmberger (2002), Source description of the 1999 Hector Mine, California earthquake; Part I: wavelet domain inversion theory and resolution analysis, *Bull. Seismol. Soc. Am.*, *92*, 4, 1192-1207,doi:10.1785/0120000916.

Johnson D.S., C.R. Argon, L.A. McGeoch, and C. Schevon (1989), Optimization by Simulated Annealing: an Experimental evaluation ; Part I, Graph Partitioning, *Operations Research*, 37, pp. 365-892.

Joseph A., J.T. Odametey, E.K. Nkebi, A. Pereira, R.G. Prabhudesai, P. Mehra, A.B. Rabinovich, V. Kumar, S. Prabhudesai and P. Woodworth (2006), The 26 December 2004 Sumatra tsunami recorded on the coast of West Africa, *Afr. J. Mar. Sci., 28*(3&4), 705–712.

Kajiura K. (1981), Tsunami energy in relation to parameters of the earthquake fault model, *Bull. Earthquake Res. Ins.*, 56, 415–440.

Kanamori H. (1972), Mechanism of Tsunami Earthquakes, *Phys. Earth Planet. Inter.*, 6, 246 – 259.

Katsumata K., N. Wada, and M. Kasahara (2003), Newly imaged shape of the deep seismic zone within the subducting Pacific plate beneath the Hokkaido corner, Japan-Kurile arc-arc junction, *J. Geophys. Res. 108*, doi:10.1029/2002JB002175.

Kennett B.L.N., and P.R. Cummins (2005), The relationship of the seismic source and subduction zone structure for the 2004 December 26 Sumatra-Andaman earthquake, *Earth Plan. Sc. Lett., 239*, 1-8, doi:10.1016/j.epsl.2005.08.015.

Kirkpatrick S.C., D. Gelatt, and M. P. Vecchi (1983), Optimization by simulated annealing, *Science*, 220, 671-680.

Konca A. O., V. Hjorleifsdottir, T.-R. A. Song, J.-P. Avouac, D. V. Helmberger, C. Ji, K. Sieh, R. Briggs, and A. Meltzner (2007), Rupture kinematics of the 2005 Mw 8.6 Nias – Simeulue earthquake from the joint inversion of seismic and geodetic data, Bull. Seismol. Soc. Am., 97, 307 – 322, doi:10.1785/0120050632.

Koketsu K., K. Hikima, S. Miyazaki, and S. Ide (2004), Joint inversion of strong motion and geodetic data for the source process of the 2003 Tokachi-oki, Hokkaido, earthquake, *Earth Planets Space, 56*, 329 – 334.

Lay T. et al. (2005), The great Sumatra-Andaman earthquake of 26 December 2004, *Science*, *308*, 1127-1133, doi:10.1126/science.1112250.

Lay T., and T. C. Wallace (1995), *Modern Global Seismology*, 521 pp., Academic Press, San Diego, California.

Lorito S., F. Romano, A. Piatanesi, and E. Boschi (2008a), Source process of the September 12, 2007, Mw 8.4 southern Sumatra earthquake from tsunami tide gauge record inversion, *Geophys. Res. Lett.*, *35*, L02310, doi:10.1029/2007GL032661.

Lorito S., A. Piatanesi, and A. Lomax (2008b), Rupture Process of the 18 April 1906 California Earthquake from Near-Field Tsunami Waveform Inversion, *Bull. Seismol. Soc. Am., 98*(2), 832–845, doi: 10.1785/0120060412.

Lorito S., A. Piatanesi, V. Cannelli, **F. Romano**, and D. Melini (2009), Kinematics and Source Zone Properties of the 2004 Sumatra-Andaman Earthquake and Tsunami: Nonlinear Joint Inversion of Tide-Gage, Satellite Altimetry and GPS data, *J. Geophys. Res.* (now accepted with revision).

Mader C. L. (2001). *Numerical modeling of water waves*, Los Alamos series in Basic and Applied Sciences, 206 p.

Marks K.M., and W.H.F. Smith (2006), An evaluation of publicly available bathymetry grids, *Mar. Geophys. Res., 27*, 19-34.

McCloskey J., S. S. Nalbant, and S. Steacy (2005), Indonesian earthquake Earthquake risk from co-seismic stress, *Nature*, *434*, 291 – 291.

McCloskey J., A. Antonioli, A. Piatanesi, K. Sieh, S. Steacy, S.S. Nalbant, M. Cocco, C. Giunchi, J.D. Huang, and P. Dunlop (2007a), Near-field propagation of tsunamis from megathrust earthquakes, *Geophys. Res. Lett.*, *34*, L14316, doi:10.1029/2007GL030494.

McCloskey J., A. Antonioli, A. Piatanesi, K. Sieh, S. Steacy, S.S. Nalbant, M. Cocco, C. Giunchi, J.D. Huang, and P. Dunlop (2007b), Tsunami Threat in the Indian Ocean from a Future Megathrust Earthquake West of Sumatra, *Earth Planet. Sci. Lett.*, in press.

Megna A., S. Barba, S. Santini, and M. Dragoni (2008), Effects of geological complexities on coseismic displacement: hints from 2D numerical modelling, *Terra Nova*, *20*(3), 173-179, doi:10.1111/j.1365-3121.2008.00800.x.

Menke W. (1989), *Geophysical Data Analysis: Discrete Inverse Theory*, rev. ed., Academic, San Diego, Calif.

Menke W., H. Abend, D. Bach, K. Newman, and V. Levin (2006), Review of the source characteristics of the Great Sumatra–Andaman Islands earthquake of 2004, *Surv Geophys, 27*, 603–613, doi: 10.1007/s10712-006-9013-4.

Merrifield M.A. et al. (2005), Tide gauge observations of the Indian Ocean tsunami, December 26, 2004, *Geophys. Res. Lett.*, *32*, L09603, doi:10.1029/2005GL022610.

Metropolis N., M. N. Rosenbluth, A. W. Rosenbluth, A. H. Teller, and E. Teller (1953), Equation of state calculations by fast compute machines, *J. Chem. Phys*., 21, 1087-1092.

Mikada H., K. Mitsuzawa, H. Sugioka, T. Baba, K. Hirata, H. Matsumoto, S. Morita, R. Otsuka, T. Watanabe, E. Araki, and K. Suyehiro (2006), New discoveries in dynamics of an M8 earthquake-Phenomena and their implications at the 2003 Tokachi Earthquake using a long term monitoring cabled observatory, *Tectonophysics*, 426, 95 – 105, doi:10.1016/j.tecto.2006.02.021

Nagarajan B., I. Suresh, D. Sundar, R. Sharma, A.K. Lal, S. Neetu, S.S.C. Shenoi, S.R Shetye, and D. Shankar (2006), The great tsunami of 26 December 2004: a description based on tide-gauge data from the Indian subcontinent and surrounding areas, *Earth Planet Space, 58*, 211–215.

Nalbant S. S., S. Steacy, K. Sieh, D. Natawidjaja, and J. McCloskey (2005), Seismology: Earthquake risk on the Sunda trench, *Nature*, *435*, 756-757, doi:10.1038/nature435756a.

Natawidjaja D. H., K. Sieh, M. Chlieh, J. Galetzka, B. W. Suwargadi, H. Cheng, R. L. Edwards, J.-P. Avouac, and S. N. Ward (2006), Source parameters of the great Sumatran megathrust earthquakes of 1797 and 1833 inferred from coral microatolls, J. Geophys. Res., 111, B06403, doi:10.1029/2005JB004025.

NIO. National Institute of Oceanography, Goa, India.

Nishimura S., M. Ando, and K. Tadokoro (2005), An application of numerical simulation techniques to improve the resolution of offshore fault kinematics using seafloor geodetic methods, *Physics of the Earth and Planetary Interiors 151,* 181–193, doi:10.1016/j.pepi.2005.03.002

Obura D. (2006), Impacts of the 26 December 2004 tsunami in Eastern Africa, *Ocean Coast. Manage.*, *49*, 873–888, doi:10.1016/j.ocecoaman.2006.08.004.

Okada Y. (1992), Internal deformation due to shear and tensile faults in a half-space, *Bull. Seismol. Soc. Am.*, *82*, 1018-1040.

Okal E. A., A. Piatanesi, and P. Heinrich (1999), Tsunami detection by satellite altimetry, *J. Geophys. Res.*, 104, 599-615.

Pacheco J. F., and L. R. Sykes (1992), Seismic moment catalog of large shallow earthquakes, 1900 to 1989, *Bull. Seismol. Soc. Am.*, 82, 1306 –1349, 1992.

Piatanesi A., and S. Lorito (2007), Rupture Process of the 2004 Sumatra–Andaman Earthquake from Tsunami Waveform Inversion, *Bull. Seismol. Soc. Am.*, *97*(1A), S223-S231, doi: 10.1785/0120050627.

Piersanti A., G. Spada, R. Sabadini, and M. Bonafede (1995), Global post-seismic deformation, *Geophys. J.Int., 120,* 544–566, doi:10.1111/j.1365-246X.1995.tb01838.x.

Pietrzak J., A. Socquet, D. Ham, W. Simon, C. Vigny, R. J. Labeur, E. Schrama, G. Stelling, and D. Vatvani (2007), Defining the source region of the Indian Ocean Tsunami from GPS, altimeters, tide gauges and tsunami models, *Earth Planet. Sci. Lett., 261*, 49-64, doi:10.1016/j.epsl.2007.06.002.

PO.DAAC. Physical Oceanography Distributed Active Archive Center, Jet Propulsion Laboratory Caltech/NASA, USA.

Rabinovich A. B. (1997), Spectral analysis of tsunami waves: Separation of source and topography effects, *J. Geophys. Res.*, 102, 12663-12676.

Rabinovich A.B., R.E. Thomson, and F.E. Stephenson (2006), The Sumatra tsunami of 26 December 2004 as observed in the North Pacific and North Atlantic oceans, *Surv. Geophys., 27*, 647–677, doi:10.1007/s10712-006-9000-9.

Rabinovich A.B., and R.E. Thomson (2007), The 26 December 2004 Sumatra Tsunami: Analysis of Tide Gauge Data from the World Ocean Part 1. Indian Ocean and South Africa, *Pure Appl. Geophys., 164*, 261–308, doi:10.1007/s00024-006-0164-5.

Reid H.F. 1910, The Mechanics of the Earthquake, The California Earthquake of April 18, 1906, Report of the State Investigation Commission, Vol.2, Carnegie Institution of Washington, Washington, D.C.

Rhie J., D. Dreger, R. Bürgmann, and B. Romanowicz (2007), Slip of the 2004 Sumatra–Andaman Earthquake from Joint Inversion of Long-Period Global Seismic Waveforms and GPS Static Offsets, *Bull. Seismol. Soc. Am.*, *97*(1A), S115-S127, doi: 10.1785/0120050620.

Rothman D. (1985), Nonlinear inversion statistical mechanics, and residual statics corrections, *Geophysiscs*, 50, 2784-2796Satake K., and Y.

Rothman D. (1986), Automatic estimation of large residual statics corrections, *Geophysics*, *51*, 332-346.

Sambridge M., J. Braun and H. McQueen (1995), Geophysical parameterization and interpolation of irregular data using natural neighbours, *Geophys. J.Int.*, *122*, 837-857, doi:10.1111/j.1365-246X.1995.tb06841.x

Sambridge M., and Mosegaard K. (2002), Monte Carlo Methods in Geophysical Inverse Problems, *Reviews of Geophysics*, 20, 1009, doi:10.1029/2000RG000089.

Satake K. (1993), Depth Distribution of Coseismic Slip Along the Nankai Trough, Japan, From Joint Inversion of Geodetic and Tsunami Data, *J. Geophys. Res., 98*, B3, 4553-4565.

Satake K. , E.A. Okal, and J. C. Borrero (2007), Tsunami and its Hazard in the Indian and Pacific Oceans: Introduction, *Pure Appl. Geophys., 154*(2-3), 249-259, doi: 10.1007/s00024-006-0172-5.

Sen M., and P.L. Stoffa (1991), Nonlinear one-dimensional seismic waveform inversion using simulated annealing, *Geophysics*, *56*, 1624-1638.

Sen M., and P. L. Stoffa (1995), *Global Optimization Methods in Geophysical Inversion*, Adv. Explor. Geophys., vol. 4, Elsevier Sci., New York.

Seno T. and K. Hirata (2007), Did the 2004 Sumatra–Andaman Earthquake Involve a Component of Tsunami Earthquakes? *Bull. Seismol. Soc. Am.*, *97*(1A), S296 - S306, doi: 10.1785/0120050615.

Shapiro N.M., M.H. Ritzwoller, and E.R. Engdahl (2008) Structural context of the great Sumatra-Andaman Islands earthquake, *Geophys. Res. Lett.*, *35*, L05301, doi:10.1029/2008GL033381.

Sindhu B, I. Suresh, A.S. Unnikrishnan, N.V. Bhatkar, S. Neetu, and G.S. Michael (2007), Improved bathymetric datasets for the shallow water regions in the Indian Ocean, *J. Earth Syst. Sci.*, *116*(3), 261-274, doi: 10.1007/s12040-007-0025-3.

Sladen A., and H. Hébert (2008), On the use of satellite altimetry to infer the earthquake rupture, characteristics: application to the 2004 Sumatra event, *Geophys. J.Int.*, *172*, 707–714, doi: 10.1111/j.1365-246X.2007.03669.x

Smith W. H. F., and P. Wessel (1990), Gridding with continuous curvature splines in tension, *Geophysics*, *55*, 293−305.

Smith W.H.F., R. Scharroo, V. V. Titov, D. Arcas , and B. K. Arbic (2005), Satellite Altimeters Measure Tsunami, *Oceanography, 18*, 11-13.

Soldati G., A. Piersanti, A., and E. Boschi (1998), Global postseismic gravity changes of a viscoelastic Earth, *J. Geophys. Res., 103,* 29,867-29,885, doi:10.1029/98JB02793.

Spudich P., and D.P. Miller (1990), Seismic site effects and the spatial interpolation of earthquake seismograms: results using aftershocks of the 1986 North Palm Springs, California earthquake, *Bull. Seismol. Soc. Am., 80*, 1504-1532.

Stein S., and E. A. Okal (2005), Speed and size of the Sumatra earthquake, *Nature*, *434*, 581-582, doi:10.1038/434581a.

Stern R. J., Subduction zones, *Reviews of Geophysics,* 40, doi:10.1029/2001RG000108.

Subarya C., M. Chlieh, L. Prawirodirdjo, J-P. Avouac, Y. Boch, K. Sieh, A.J. Meltzmer, D.H. Natawidjaja and R. McCaffrey (2006), Plate-boundary deformation associated with the great Sumatra-Andaman earthquake, *Nature, 440,* 46-51, doi:10.1038/nature04522.

SuGAr, Sumatran GPS Array of Caltech's Tectonics Observatory, http://www.tectonics.caltech.edu/sumatra/data.html

Satake K., and Y. Tanioka (1999), Sources of Tsunami and Tsunamigenic Earthquakes in Subduction Zones, *Pure Appl. Geophys.*, 154, 467-483

Tanioka Y., K. Hirata, R. Hino, and T. Kanazawa (2004a), Slip distribution of the 2003 Tokachi-oki earthquake estimated from tsunami waveform inversion, *Earth Planets Space 56*, 373 – 376.

Tanioka Y. et al. (2004b), Tsunami run-up heights of the 2003 Tokachi-oki earthquake, *Earth Planets Space 56,* 359-365.

Tanioka Y., E.L. Geist, and N.T. Puspito (2006a), Preface to special issue ''The 2004 Great Sumatra Earthquake and Tsunami'', *Earth Planets Space 58(2),* 111.

Tanioka Y., Yudhicara, T. Kususose, S. Kathiroli, Y. Nishimura, S.I. Iwasaki, and K. Satake (2006b), Rupture process of the 2004 great Sumatra-Andaman earthquake estimated from tsunami waveforms, *Earth Planet Space, 58*, 203-209.

Tarantola A. (1987), *Inverse Problem Theory*, Elsevier Sci., New York.

Thomson R.E., A.B. Rabinovich, and M.V. Krassovski (2007), Double jeopardy: Concurrent arrival of the 2004 Sumatra tsunami and storm-generated waves on the Atlantic coast of the United States and Canada, *Geophys. Res. Lett.*, *34*, L15607, doi:10.1029/2007GL030685.

Tinti S., and R. Tonini (2005), Analytical evolution of tsunamis induced by near-shore earthquakes on a constant-slope ocean, *J. Fluid Mech., 535*, 33–64, doi:10.1017/S0022112005004532.

Titov V., A.B. Rabinovich, H.O. Mofjeld, R.E. Thomson, and F.I. González (2005), The Global Reach of the 26 December 2004 Sumatra Tsunami, *Science, 309*, 2045-2048, doi:10.1126/science/1114576.

Tsuji Y., Y. Namegaya, H. Matsumoto, S.-I. Iwasaki, W. Kambua, M. Sriwichai and V. Meesuk (2006), The 2004 Indian tsunami in Thailand: tsunami height and tide-gauge records, *Earth Planet Space*, *58*, 223-232.

UHSLC, University of Hawaii Sea Level Center, USA.

United Kingdom Hydrographic Office (2005). Catalogue of Admiralty Charts and Publications, 2005 Edition, Taunton, Somerset, United Kingdom.

Vigny C., W.J.F. Simons, S. Abu, R. Bamphenyu, C. Satirapod, N. Choosakul, C. Subaraya, A. Soquet, K. Omar, H.Z. Abidin, and B.A.C. Ambrosius (2005), GPS in SE Asia provides unforeseen insights on the 2004 megathrust earthquake Insight into the 2004 Sumatra-Andaman earthquake from GPS measurements in Southeast Asia, *Nature*, *436*, 201-206, doi:10.1038/nature03937.

Wald D. J., and T. H. Heaton (1994), Spatial and temporal distribution of slip for the 1992 Landers, California earthquake, *Bull. Seismol. Soc. Am.*, 84, 668-691.

Wald D. J., and R. W. Graves (2001), Resolution analysis of finite fault source inversion using one- and three-dimensional Green's functions 2. Combining seismic and geodetic data, *J. Geophys. Res., 106*, 8767–8788.

Wang R., F. L. Lorenzo, and F. Roth (2003). Computation of deformation induced by earthquakes in multi-layered elastic crust — FORTRAN programs EDGRN/EDCMP, *Comput. Geosci.*, *29*, 195–207.

Wang Z., and D. Zhao (2005), Seismic imaging of the entire arc of Tohoku and Hokkaido in Japan using P-wave, S-wave and sP depth-phase data*, Physics of the Earth and Planetary Interiors 152*, 144-162, doi:10.1016/j.pepi.2005.06.010.

Wang R., F.L. Martin, and F. Roth (2006), PSGRN/PSCMP - a new code for calculating co- and post-seismic deformation, geoid and gravity changes based on the viscoelastic-gravitational dislocation theory. *Computers and Geosciences, 32*, 527-541, doi:10.1016/j.cageo. 2005.08.006.

Ward S. N. (2001), "Tsunamis" in *The Encyclopedia of Physical Science and Technology,* ed. R. A. Meyers, Academic Press.

Watanabe T., H. Takahashi, M. Ichiyanagi, M. Okayama, M. Takada, R. Otsuka, K. Hirata, S. Morita, M. Kasahara, and H. Mikada (2006), Seismological monitoring on the 2003 Tokachi-oki earthquake, derived from off Kushiro permanent cabled OBSs and land-based observations, *Tectonophysics, 426*, 107-118, doi:10.1016/j.tecto.2006.02.016.

Wells D. L., and K. J. Coppersmith (1994), New empirical relationships among magnitude, rupture length, rupture width, rupture area, and surface displacement. *Bull. Seismol. Soc. Am.*, 84, 974-1002.

Wesnousky S. G. (1994), The Gutenberg-Richter or Characteristic Earthquake Distribution,

Which Is It?, *Bull. Seismol. Soc. Am.*, 84, 1940-1959.

Wessel P., and W. H. F. Smith (1998), New, improved version of the Generic Mapping Tools Released, EOS Trans. AGU, 79, 579.

Yagi Y. (2004), Source rupture process of the 2003 Tokachi-oki earthquake determined by joint inversion of teleseismic body wave and strong ground motion data*, Earth Planets Space, Vol 56*, 311-316.

Yamanaka Y., and M. Kikuchi (2003), Source process of the recurrent Tokachi-oki earthquake on September 26, 2003, inferred from teleseismic body waves*, Earth Planets Space, 55*, e21–e24.

Yamanaka H., K. Motoki, K. Etoh, M. Murayama, and N. Komaba (2004), Observation of aftershocks of the 2003 Tokachi-Oki earthquake for estimation of local site effects, *Earth Planets Space, 56*, 335-340.

Zhao S., R.D. Müller, Y. Takahashi, and Y. Kaneda (2004), 3-D finite-element modelling of deformation and stress associated with faulting: effect of inhomogeneous crustal structures, *Geophys. J. Int., 157,* 629-644, doi:10.1111/j.1365-246X.2004.02200.x.